

Quantitative immuno-mass spectrometry imaging by laser ablation-inductively coupled plasma-mass spectrometry

A thesis submitted for the degree of Doctor of Philosophy at

University of Technology Sydney

Faculty of Science

School of Mathematical and Physical Sciences

By Mika T Westerhausen

Supervised by:

Professor Philip Doble

Dr Nerida Cole

Dr David Bishop

Associate Professor Andrew McDonagh

2019

Abstract

Laser ablation inductively coupled plasma mass spectrometry (LA-ICP-MS) is an elemental bio-imaging technique that combines high sensitivity and spatial resolution of elements with quantification in two or three dimensions. LA-ICP-MS has recently been applied to detection and quantification of non-elemental analytes (eg. proteins) in tissue sections using immunohistochemical methods. This approach uses molecular probes such as antibodies, tagged with reporter elements such as the lanthanides which are not found naturally in biological samples. Analyses based on these methods is known as immuno-mass spectrometry imaging (iMSI) and has the potential for application to currently refractive research questions in cell and organ biology and new diagnostic platforms.

The drawbacks of commonly used matrix-matched tissue standards were addressed by development of novel facile methods for the preparation of moulded gelatin standards. Surface roughness and robustness were compared against cryo-sectioned gelatin and homogenised brain tissue standards. The moulded standards had significantly higher accuracy, precision and reproducibility and were easier to prepare. Additionally, background metals in gelatin were removed using chelating resins to increase the dynamic calibration range and to improve limits of analysis.

The resolution of LA-ICP-MS elemental bio-imaging is usually constrained by the diameter of the laser spot size and is often not adequate to explore in situ sub-cellular distributions of elements and proteins in biological tissue sections. Super-resolution reconstruction is a method used for many imaging modalities, combining multiple lower resolution images to create a higher resolution image. This thesis describes a super-resolution reconstruction method for LA-ICP-MS imaging by ablating consecutive layers of a biological specimen with offset orthogonal scans. Layer-by-layer image reconstruction was extended to the third dimension without the requirement of image registration across multiple sections. Quantitative super-resolution reconstruction provided superior image clarity and fidelity in two- and three-dimensions.

These methods were applied to the development of iMSI for both antibody and aptamer probes to quantify and localise dystrophin in muscle, and myelin basic protein in brain. Quantification of dystrophin is challenging by conventional methods and is central to development of Duchenne muscular dystrophy treatments. Samples were stained with a gadolinium labelled anti-dystrophin antibody and analysed by LA-ICP-MS. Normal mouse and normal human samples were found to have ~700 and ~300 parts per billion gadolinium respectively with under 20% relative standard deviation. The results improved on current methods and met FDA guidelines. The feasibility of using aptamers for iMSI was confirmed, which may enable analysis of challenging targets.

Certificate of Original Authorship

I certify that the work in this thesis has not previously been submitted for a degree nor has it been submitted as part of requirements for a degree except as fully acknowledged within the text.

I also certify that the thesis has been written by me. Any help that I have received in my research work and the preparation of the thesis itself has been acknowledged. In addition, I certify that all information sources and literature used are indicated in the thesis.

This research is supported by an Australian Government Research Training Program

Signature of Student:

Production Note:
Signature removed prior to publication.

Date: 31/07/19

Dedicated to difficulty

Acknowledgements

I would like to acknowledge my three supervisors in order of chronological encounter. Firstly, Associate Professor Andrew McDonagh for introducing me to research during my undergraduate research project on ruthenium phthalocyanine and putting a secretly analytical chemistry project among the physics honours projects so that a naïve young nanotechnology student could unwittingly give it a try.

Secondly Professor Philip Doble for initially putting Andrew up to the task of luring students over to analytical chemistry dark arts and eventually for putting up with my physics brained peculiarities over the course of my PhD studies. Finally, I would like to thank Dr Nerida Cole for teaching me everything that is required to be a researcher worth one's salt from experiments in the lab to brainstorming in the pub and supporting my endeavours from near and afar.

Next I would like to thank the three postdocs that helped me throughout my PhD but especially during the final months of thesis writing. Dr David Bishop, Dr Raquel Gonzalez de Vega, and Dr David Clases were all extremely helpful. I would particularly thank David Bishop for the ongoing collaboration and helping me translate my research to clear and logical presentation.

The champions of the lab Ronald Shimmon, Alex Angeloski and Dayanne Mozaner Bordin who have helped me for the whole of my PhD, despite breaking machines, finishing all the reagents and being an all-round nuisance in the lab.

The physics kids both finished and fallen soldiers who supported me from undergrad through to PhD: Kerem Bray, Matt Tai, Marc Gali Labarias, Alba Santín Garcia, Rodolfo Previdi and Vince Ha-Hau.

Much love and thanks to the PhD students of the group formerly known as Elemental Bio-Imaging Group now known as Atomic Medicine Initiative. Phuc Nguyen Prashina Singh, Karen Duong, Natasha Benson, Matthew Diplock, Thomas Lockwood, Joel Steele, Jake Violi, David Gertner, Sarah Meyer, and Vitor Cesar Taranto. Also, our newly

minted *Goodest Bois* Helen Zeng, Fiona Dang, Siobhan Peters and Jacob Marecic. Friday beers at Staves were an essential distress from weeks of machine mishaps.

Finally, I would like to thank my family for their continued support over my many years of study.

List of Publications

Refereed journal publications

[1] Mika T. Westerhausen*, David P. Bishop*, Annette Dowd, Jonathan Wanagat, Nerida Cole & Philip A. Doble, “Super-Resolution Reconstruction for Two-and Three-Dimensional LA-ICP-MS Bioimaging”, *Analytical Chemistry*, October 2019.

[2] Mika T. Westerhausen*, Thomas E. Lockwood *, David P. Bishop, , Raquel Gonzalez de Vega, Anna Röhnelt, Nerida Cole, Philip A. Doble & David Clases, “Low background mould-prepared gelatine standards for reproducible quantification in elemental bio-imaging”, *The Analyst*, October 2019.

[3] Mika Westerhausen*, David P. Bishop*, Nerida Cole, Elizabeth Gibbs, Rachelle Crosbie-Watson, Florian Barthelemy, Stan Nelson, Carrie Miceli, Philip A. Doble, and Jonathan Wanagat, “Quantitative immuno-mass spectrometry imaging of skeletal muscle dystrophin”, Article in preparation, Jan 2020.

*Equal First Author

Conference oral presentations

Mika T Westerhausen, David Bishop, Nerida Cole, Philip Doble, “Orthogonal Anisotropic Acquisition LA-ICP-MS for 2D and 3D Super Resolution Reconstruction Bio-Imaging”, Asia-Pacific Winter Conference on Plasma Spectrochemistry (APWC), 2017, Matsue, Japan

Mika T. Westerhausen, David P. Bishop, Nerida Cole, Jon Wanagat & Philip Doble, “Super-resolution reconstruction for bio-imaging by LA-ICP-MS”, European Winter Conference on Plasma Spectrochemistry (EWPCPS), 2019, Pau, France

Mika T. Westerhausen, David P. Bishop, Nerida Cole, Jon Wanagat & Philip Doble, “3D Super-resolution reconstruction for bio-imaging by LA-ICP-MS”, Conference on Laser Ablation, 2019, Maui-Hawaii, USA

Table of Contents

Abstract	ii
Certificate of Original Authorship.....	iv
Acknowledgements	vi
List of Publications	viii
Refereed journal publications	viii
Conference oral presentations.....	viii
Table of Contents.....	ix
List of Figures	xiv
List of Tables.....	xix
Acronyms & Abbreviations	xx
1. Literature Review	1
1.1 Metals in biology.....	1
1.1.1 Sources of metals	1
1.1.2 Analysis of elements	2
1.1.3 Mass Spectrometry in bioanalysis.....	3
1.1.3.1 Elemental Mass Spectrometry.....	4
1.1.3.2 Inductively coupled plasma mass spectrometry	4
1.1.4 Elemental bio-imaging techniques	6
1.1.4.1 LA-ICP-MS: fundamentals, principles and fields of application.....	10
1.1.4.1.1 Laser Ablation limits	11
1.1.4.1.2 Quantification strategies by means of LA-ICP-MS	13
1.1.4.1.3 Applications of LA-ICP-MS	15
1.1.4.2 Immuno-Mass Spectrometry Imaging and beyond	15
1.1.5 Tagging agents	18

1.1.6	Image processing	21
1.2	Thesis aims.....	24
2	Materials and Methods	26
2.1	Instrumentation.....	26
2.1.1	Solution nebulization inductively coupled plasma mass spectrometry	26
2.1.2	Laser ablation inductively coupled plasma mass spectrometry	28
2.1.3	Microscopy	30
2.1.4	Profilometry	30
2.1.5	Protein quantification via Spectrophotometry	31
2.2	Data acquisition and processing	31
2.2.1	Data acquisition	31
2.2.1.1	Conversion from raw data to 2D representation.....	32
2.2.2	Data visualization and manipulation	33
2.3	Experimental Methods.....	33
2.3.1	Chemicals and Reagents.....	33
2.3.2	Matrix Matched Mouse Brain Standards	34
2.3.2.1	Quantification of Metal Concentrations in Standards	34
2.4	Calculations.....	35
2.4.1	Linear regression analysis	35
2.4.2	Limits of analysis and outliers	36
2.5	Animals.....	36
2.5.1	Immunohistochemistry	37
3	Standard Preparation and Comparison	38
3.1	Abstract.....	38
3.2	Introduction.....	38
3.3	Method	41
3.3.1	Gelatin Standards.....	41

3.3.2	Tissue Standards	44
3.3.3	SN-ICP-MS.....	44
3.3.4	Elemental extraction to decrease background levels.....	45
3.3.5	LA-ICP-MS.....	45
3.3.6	Data Analysis	46
3.3.7	Profilometry	46
3.4	Results and Discussion	47
3.4.1	Qualitative comparison of mould methods	47
3.4.2	Topography and height characterisation.....	49
3.4.3	Post-analysis characterisation	52
3.4.4	Analytical figures of merit and background equivalent concentrations	53
3.5	Conclusion.....	56
3.6	Acknowledgments	57
4	Super resolution reconstruction for LA-ICP-MS imaging.....	58
4.1	Abstract.....	58
4.2	Introduction.....	58
4.3	Method	60
4.3.1	Instrumentation.....	60
4.3.2	Reagents	61
4.3.3	Standard Preparation.....	61
4.3.4	Sample Preparation	62
4.3.5	Optimisation of image acquisition parameters.....	63
4.3.6	Super Resolution Reconstruction.....	65
4.3.7	Processing Algorithms	66
4.3.8	Image processing software.....	67
4.3.9	Statistical Analysis.....	67

4.4	Results and Discussion	67
4.4.1	Optimisation of image acquisition parameters	67
4.4.2	Calibration	71
4.4.3	Quantification.....	76
4.4.4	Three-Dimensional Reconstruction	78
4.5	Conclusions.....	80
5	Muscular Dystrophy	82
5.1	Abstract.....	82
5.2	Introduction.....	82
5.3	Methods.....	86
5.3.1	Materials.....	86
5.3.2	Mouse models	86
5.3.3	Human tissue	87
5.3.4	Histological preparation	87
5.3.5	3-dimensional sample preparation.....	87
5.3.6	Preparation of iMSI standards	88
5.3.7	iMSI	89
5.3.8	Image processing	89
5.3.9	Statistical analysis.....	89
5.4	Results and Discussion	90
5.4.1	iMSI in wild-type and mdx mouse skeletal muscle.....	90
5.4.2	iMSI in normal human and DMD skeletal muscle.....	95
5.4.3	3D iMSI of thick sections.....	99
5.5	Conclusion.....	103
6	Towards aptamer imaging.....	105
6.1	Abstract.....	105
6.2	Introduction.....	105

6.3	Method	108
6.3.1	Animal Handling	108
6.3.2	Lanthanide Labelling of antibodies.....	108
6.3.3	MBP Antibody labelling.....	108
6.3.4	MBP Aptamer labelling	109
6.3.5	Myelin Basic Protein Antibody and Aptamer specificity analysis.....	112
6.3.6	Microscopy	112
6.3.7	LA-ICP-MS.....	113
6.3.8	Preparation of iMSI standards	113
6.4	Results and Discussion	114
6.4.1	Antibody vs Aptamer	114
6.4.2	Aptamer binding confirmation via dot blot	114
6.4.3	Fluorescence microscopy comparison.....	116
6.4.4	LA-ICP-MS comparison.....	119
6.5	Conclusion.....	121
7	Overall conclusions and future work.....	123
8	References.....	126
9	Appendix.....	157

List of Figures

Figure 1.1: Bioimaging of four transition metals (Cu, Fe, Zn and Mn) in mouse brain by LA-ICP-QMS imaging, scale bar 2mm. [24].....	8
Figure 1.2: Laser ablation inductively coupled plasma mass spectrometry schematic using a helium and argon gas system [33].	10
Figure 1.3: Comparison of ablation spot between a) nanosecond and b) femtosecond pulse width LA-ICP-MS systems [44].	12
Figure 1.4: Comparison of antibody and aptamer structures [85].	17
Figure 1.5: Schematic of indirect immunolabelling using fluorescent tagging [88].	18
Figure 1.6: Double immunolabeling of two cytokeratins, Ck14 (IgG3) and Ck8/18/19 (IgG1), in a duct wall of the human mammary gland (Twenty micrometers scale bar and colours are for Ck8/18/19 (a, FITC, green), Ck14 (b, Alexa-647, pink) and for nuclei (DAPI, blue) [86].....	19
Figure 1.7: Scheme of selected bi-functional ligands used as labelling reagents and their binding to amino acids of an antibody. The SCN-DOTA covalently binds to 3-amino groups of lysine residues. The other opportunity shown here is the labelling via a maleimide group which binds to the sulfhydryl residues after partial reduction of the antibody's cysteine-based disulfide bridges. MeCAT and SCN-DOTA contain a DOTA macro-cycle (pink circle) to complex lanthanide ions whereas the MAXPAR polymer chain contains many DTPA residues as chelating compounds (yellow circle).	21
Figure 1.8: Illustration of the basic principle of Super Resolution Reconstruction.	23
Figure 1.9: Scheme illustrating the super-resolution reconstruction from the acquisition of two orthogonal thick slices [122].....	24
Figure 2.1: Agilent 7500cx (left) and 7700x (right) Series Inductively Coupled Plasma Mass Spectrometer fitted with Agilent Integrated Autosampler [124].	26
Figure 2.2 NWR-193 Laser Ablation System [123] (left) and Agilent 7700 Series Inductively Coupled Plasma Mass Spectrometer [124] (right).....	28
Figure 2.3: Leica FS CB microscope.	30
Figure 2.4: DektakXT Profilometer.	30

Figure 2.5: Thermo Scientific™ NanoDrop 2000 Spectrophotometer.	31
Figure 2.6: Representation of laser ablation raster and the resulting spectra.	32
Figure 2.7: Graphic user interface for ImaJar software.	33
Figure 3.1: Moulding devices for gelatin standards: Cavity slide (A), Culturewell™ (B) and Hybriwell™(C).	42
Figure 3.2: 6-well Hybriwell™ gasket schematic [152].	43
Figure 3.3: Cavity slide gelatin standards. Plan view and single concavity aspect.	47
Figure 3.4: Culturewell™ silicon gasket gelatin standards. Plan view and aspect of 4 wells.	47
Figure 3.5: Hybriwell™ slide gelatin standards left in the freezer too long. Plan view and aspect of 2 wells.	48
Figure 3.6: Hybriwell™ slide gelatin standards. Plan view and aspect of 2 wells.	48
Figure 3.7 Teflon tape manufactured schematic and as fabricated gelatine standards.	49
Figure 3.8: Normalised heights as determined by profilometry showing deviations in height and heterogeneity in surface topography. The measured height of the tissues/standards was normalised to the expected height.	50
Figure 3.9: Visual comparison of an ablated homogenised animal tissue standard (A) and a gelatin standard (B). (C): Profilometry data standards ablated eleven times with increasing laser power. (D): Signal intensities for Mn, Cu, and Zn derived from repeated ablation of standard material.	53
Figure 4.1: Orthogonal acquisition, (A) first line scans, (B) second line scans offset by half the magnitude of the laser spot size, (C) combined pattern for SRR processing. Arrows denote direction of scan.	65
Figure 4.2: SRR processing of two ablated layers. (A) The two layers acquired with an AR of 2 in the horizontal and vertical directions. (B) and (C) Representation of the two layers brought to congruence using the Kronecker Product. (D) Up- sampling with null values into a checkerboard pattern. (E) Layers offset and stacked into a 3D array and null values and trilinearly interpolated. (F) Populated layers summed together to produce final 2D image.	66
Figure 4.3: Representative photomicrograph of dystrophin in murine quadriceps. The expression of the protein is clearly seen as a honeycomb structure in the	

membranes of the muscle fibres. The protein was stained with Gd-labelled MANDYS8 primary antibody and detected using a goat anti-mouse secondary antibody (Sigma) conjugated to alkaline phosphatase with NBT/BCIP substrate (Sigma).68

Figure 4.4: Image panel of acquisition parameter optimisation. Seven acquisitions were considered representing ARs ranging from 1 to 10. The SRR images are in column 1, except for (A), which was constructed in the conventional manner. Column 2 are the images after application of the Gaussian filter, whilst column 3 represents images after RLTV.70

Figure 4.5: Post ablation raster pattern after two passes in the horizontal and vertical directions.72

Figure 4.6 Representative calibration curves and image panels. (A) Anisotropic single layer calibration curve in horizontal direction. (B) Image of calibration standards in horizontal direction. (C) Anisotropic single layer calibration curve in vertical direction. (D) Image of calibration standards in vertical direction (E) Calibration curve after SRR with AR = 2. (F) Image of calibration standards after SRR. (G) Calibration curve after application of the Gaussian filter. (H) Image of calibration standards after Gaussian filter. (I) Calibration curve after RLTV. (J) Image of calibration standards after RLTV.73

Figure 4.7: Effect of image processing on two-layer test. (A) Anisotropic acquisition of single layer in horizontal direction. (B) Same layer as (A), transposed to vertical direction. (C) SRR of (A) and (B). (D) Application of Gaussian filter. (E) RTLTV image.78

Figure 4.8: Three-dimensional reconstructions of continuously ablated 50 μm section. (A) Planar view of single focus acquisition. (B) and (C) Oblique and isometric views of refocused laser acquisition at 5 μm for each pass. (D), (E), and (F) Planar, oblique and isometric views of single focus laser acquisition. The structural integrity of the dystrophin is clearly seen throughout the 10 layers.79

Figure 5.1: Dystrophin iMSI in wild type and mdx mouse quadriceps muscle. A, low-resolution iMSI (15 μm) of whole mouse quadriceps cross section showing expected sarcolemmal distribution of dystrophin. High-resolution (1.75 μm)

images of dystrophin by iMSI in wild-type (B) and mdx mouse quadriceps (C). Quantification scale in A denotes ppb of gadolinium for all panels.	90
Figure 5.2: Histograms with the 3 tested thresholding methods (A). Intensity map of WT quadricep (B) with the correlating threshold methods: Raw (C), Median (D) and Otsu's (E) using the histogram colours to represent the areas of the image used for quantification.	92
Figure 5.3: Representative areas of ablation of murine quadriceps, A, B and C. Black scale bar represents 1000 μm	93
Figure 5.4: IHC with hematoxylin counterstain (A) and iMSI (B) for dystrophin in serial sections of human quadriceps muscle (80 year old). Scale bar in A denotes 100 microns and applies to both images. The same gadolinium-labeled anti-dystrophin antibody was used in both. Quantification scale in C denotes ppb of gadolinium.	95
Figure 5.5: Exemplar iMSI image of section from 18-year-old male vastus lateralis biopsy. Scale bar is in ppb Gd.	96
Figure 5.6: IHC (A) and iMSI (B) of dystrophin in serial muscle sections from a patient with Duchenne muscular dystrophy. Quantification scale in C denotes ppb of gadolinium in panel B. Black bar in A denotes 100 microns.	97
Figure 5.7: Consecutive sections of human quadricep tissue (1-4) on the same intensity scale.	100
Figure 5.8: Two-dimensional image in the X-Z plane of 12-layer 3D stack of 30 μm thick sections incubated for 30 (A) ,60 (B) and 120 (C) minutes on the same intensity scale. Red line signifies the final layer with signal above the LOQ.	101
Figure 5.9: Two-dimensional image in the X-Z plane of 16-layer 3D stack of 30min incubated tissue of thickness 10 μm (A), 30 μm (B) 50 μm (C) on the same intensity scale Red line signifies the final layer with signal above the LOQ. ...	102
Figure 5.10: 3D image of 120min incubation time 30um section, scale in ppb of Gd. .	103
Figure 6.1: Dot blots of MBP only control (A), MBP Aptamer only control(B), human serum albumin control (C), unfolded MBP aptamer 5' biotin (D), and folded MBP aptamer 5' biotin (E) all visualized with streptavidin HRP and TMB substrate.	115

Figure 6.2: Elemental images of dot blots for folded Scrambled MBP aptamer 5' thiol tagged with ¹⁵³Eu control (A), folded MBP aptamer 5' thiol tagged with ¹⁵³Eu (B), unfolded MBP 5' biotin tagged with streptavidin Eu (C), folder MBP 5' biotin tagged with streptavidin Eu (D), MBP only control with streptavidin Eu (E), MBP aptamer 5' thiol tagged with 153Eu only control(F), and MBP aptamer 5' Biotin only control (G).116

Figure 6.3: Mouse hippocampal formation stained with Rabbit antiMBP AntiRabbit-FITC (Green) and Hoechst 33342 (Blue) (A) and MBP aptamer 5' Biotin and Streptavidin FITC (Green) and Hoechst 33342 (Blue) (B). The white arrow points to an oligodendrocyte.117

Figure 6.4: Mouse hippocampus stained with MBP aptamer 5' Biotin and Streptavidin Qdot (Red) and Hoechst 33342 (Blue). The white arrow points to a possible oligodendrocyte.118

Figure 6.5: Mouse hippocampus (A) and hippocampal formation (B) stained with MBP aptamer 5' Biotin and Streptavidin FITC (Green) and Hoechst 33342 (Blue) courtesy of the Human Protein Atlas[240] The white arrows point to possible oligodendrocytes.....119

Figure 6.6: Low resolution images of MBP aptamer biotin 5'-Streptavidin Eu (A), MBP aptamer thiol 5' -¹⁵³Eu (B) and antiMBP-¹⁵³Eu (C). Calibration bar denotes ppb Eu.120

Figure 6.7: High resolution image of MBP aptamer 5'biotin-streptavidin Eu (A) and correlating antiMBP-FITC micrograph courtesy of the Human Protein Atlas [240] Calibration bar denotes ppb Eu.121

List of Tables

Table 2.1: Typical ICP-MS parameters for SN-ICP-MS.....	27
Table 2.2: Typical LA-ICP-MS parameters.	29
Table 2.3: Table of formulas used in the excel function LINEST.	35
Table 2.4: General equations used for statistical analysis.	36
Table 3.1: Metal salts used in Gel Standards.....	42
Table 3.2: Concentrations of external calibration standards.	45
Table 3.3: Comparison of accuracy derived from different preparation methods and materials.....	51
Table 3.4: Characterisation of standard materials. The concentrations and error of each calibration level were cross-quantified by solution-based ICP-MS. LOD, Sensitivity and Linearity were determined from the calibration curve constructed by LA-ICP-MS.	54
Table 3.5: Background concentration [pg/g] of gelatin materials prior and after an additional extraction step with different resins, respectively.....	55
Table 4.1: Concentrations of gelatin standards.	61
Table 4.2: Concentration of liquid standards.	62
Table 4.3: Super resolution reconstruction acquisition parameters.....	64
Table 4.4: Analytical Figures of Merit after application of the processing algorithms. .	74
Table 4.5: Average Response and %RSD for calibration standard near or above the LOQ.	76
Table 4.6: Average concentrations and %RSD for simulated two-layer sample.....	77
Table 5.1: Incubation and section parameters for 3D atlas incubation.....	88
Table 5.2: Concentrations of gelatin standards (ng/g± ng/g).	89
Table 5.3: Average values of gadolinium (ppb) and % RSDs from the regions of interest and thresholding methods for wildtype murine quadriceps	94
Table 5.4: Technical replicates of dystrophin iMSI from consecutive serial muscle sections.....	98
Table 6.1: Sequences and Functionalisation of Oligonucleotides.....	110
Table 6.2: Concentrations of gelatin standards (ng/g).	113

Acronyms & Abbreviations

2D Two Dimensional

3D Three Dimensional

AP Alkaline Phosphatase

AR Anisotropic Ratio

CRM Certified Reference Material

DAPI 4',6-diamidino-2-phenylindole

DMD Duchenne's Muscular Dystrophy

EBI Elemental Bio-Imaging

EDTA Ethylenediaminetetraacetic acid

FDA Food and Drug Administration

FFPE Formalin-Fixed Paraffin-Embedded

FITC Fluorescein isothiocyanate

FM Fluorescence Microscopy

HRP Horseradish Peroxidase

ICP-MS Inductively coupled plasma mass spectrometry

IHC Immunohistochemistry

LA-ICP-MS Laser Ablation Inductively Coupled Plasma Mass Spectrometry

LIBS Laser-induced breakdown spectroscopy

LOD Limit of Detection

LOQ Limit of Quantification

IPIXE Ion Particle induced X-ray emission

MALDI Matrix Assisted Laser Desorption/Ionization

MeCAT Metal-coded affinity tags

MBP Myelin Basic Protein

MC Multicollector

Mdx Mutation Dystrophin X-Chromosome

MRI Magnetic Resonance Imaging

PBS Phosphate Buffered Saline

PMMA Poly(methyl methacrylate)

ppb Parts per billion

ppm Parts per million

PTFE Polytetrafluoroethylene

RLTV Richardson-Lucy Total Variance

RNA Ribonucleic acid

SCN-DOTA 2-(4-isothiocyanatobenzyl)-1,4,7,10-

tetraazacyclododecane-1,4,7,10-
tetraacetic acid

SIMS Secondary Ion Mass Spectrometry

SN-ICP-MS Solution Nebulisation
Inductively Coupled Plasma Mass
Spectrometry

SRR Super Resolution Reconstruction

ssDNA single stand Deoxyribonucleic
acid

TBS Tris Buffered Saline

TCEP Tris(2-carboxyethyl)phosphine

TOF Time of flight

WT Wildtype

XFM X-Ray Fluorescence Microscopy

XPS X-ray photoelectron spectroscopy

1. Literature Review

1.1 Metals in biology

Metals are a fundamental building block for life and are required to sustain the growth, development, and sustenance of all living organisms and ecosystems. Metals are distributed in a heterogeneous way across biological systems in both a spatial and temporal manner and are the root cause of various diseases and conditions. Both the form and the location of a metal dictates the effects it has in a biological entity [1]. The chemical composition of biological tissues is of great interest in biomedical research. Essential elements such as Cu, Zn and Fe play an important structural and functional role in proteins and enzymes. Knowledge on their chemical species, location, and concentration is the key for understanding their biological functions such as signalling, metabolism, and homeostasis in cells. Elucidating the important roles of metals in biological systems requires a multi-disciplinary approach at the interface of chemistry, biology and physics.

1.1.1 Sources of metals

Metals are usually heterogeneously distributed in tissues or cells and may be present free or bound to proteins, depending on their affinity and stability. Metals play important roles in the human body, maintaining cell structure and regulating gene expression, neurotransmission, and antioxidant response. There are major elements in high abundance which are responsible for vital bodily functions. Calcium and magnesium are used structurally in the synthesis of bone [2,3] and teeth [4], sodium and potassium contribute to isotonicity in various anatomical fluids [5], and cobalt is central to the essential cofactor, cobalamin (vitamin B12) [6].

Metals also contribute to the function of the body through their interaction either with or within various proteins. An estimated 50% of proteins contain metals [7], thus monitoring their abundance within biological systems can act as a predictor of the state of various tissues or metabolic pathways. Metals known to be contained in these metalloproteins are as follows: vanadium, chromium, manganese, iron, cobalt, nickel,

copper, zinc, molybdenum, tungsten, silicon, selenium, and tin [8] which are involved in crucial functions and forms. Variability of these metalloproteins and by extension the reactive metals they contain may be indicative of disease states or abnormalities. This has been demonstrated in a mouse model where iron concentrations in specific areas of the brain serve as a risk predictor for Parkinsonian neurodegeneration [9].

This imbalance of metals within the body may be caused by endogenous system malfunction or exogenous introduction of toxic species. An excessive metal accumulation in the nervous system may be toxic, inducing oxidative stress, disrupting mitochondrial function, and impairing the activity of numerous enzymes. Damage caused by metal accumulation may result in permanent injuries, including severe neurological disorders [10]. Metals are also purposefully introduced into the body to help with diagnostic scanning techniques where they are used as contrast agents, under the assumption they are safely evacuated by the body afterwards. Gadolinium-based contrast agents were found to be the cause of a rare syndrome called nephrogenic systemic fibrosis due to trace level accumulation of gadolinium in organs over the course of multiple treatments resulting in new guidelines for use [11]. Sometimes the introduction of exogenous metal is accidental from any manufactured good with contamination being an ever-increasing fear. Due to the various agents and chemicals used in manufacturing and everyday life the environment itself can be a source of metals which are inherently toxic when inhaled, ingested or when skin contact is made such as arsenic, lead and mercury [12]. The effect that metals levels have on human biology is vast and in need of deep analysis.

1.1.2 Analysis of elements

Metal ions are fundamental components of the chemistry of life. In fact, it is estimated that one third of proteins require a metal cofactor to perform their functions. The determination of chemical forms of elements is still an analytical challenge.

The study of the metal species calls for a new generation of analytical tools (bioanalysis) that substitute the traditional atomic detectors based in the use of photons (atomic absorption spectrometry (AAS), inductively coupled plasma-atomic emission spectroscopy (ICP-AES), atomic fluorescence spectroscopy(AFS)) by mass detectors

(mass spectrometry (MS) and inductively coupled plasma-mass spectrometry (ICP-MS)) that characterize ions [13].

1.1.3 Mass Spectrometry in bioanalysis

Mass spectrometry (MS) is an analysis technique based on separating the ionised form of elements using the mass to charge ratio of given ions.. It is an extremely sensitive technique, highly versatile and whose are of application are experiencing enormous growth in recent years. The MS can provide very valuable information about the chemical compounds: the molecular mass, the global formula and, from the pattern of fragmentations, the molecular structure, as well as the elemental and isotopic composition in natural or labelled substances. Recent advances in technology have revolutionized the way in which biological systems are visualized and studied. Advances in Mass Spectrometry have allowed the analysis of cellular proteins and metabolites (proteomics and metabolomics respectively) on an unimaginable scale [14].

The term Metabolomics refers to the study, identification and systematic quantification of low molecular weight compounds in certain cells, tissues or biological fluids that are the product of metabolic reactions in living beings. One of its main objectives is to identify subtle changes in the metabolic profiles between biological systems in different physiological or pathological states. Proteomics focuses on the study of the set of proteins produced in a cell, tissue or organism, its location, structure, stability and interaction. In addition, we know that in order to properly characterize a biological system it is also necessary to approach the study of its metallic species. That is, the chemistry of the cell must be characterized not only by the genome and proteome, but also by the distribution of metals and metalloids between the different biomolecules.

In recent years, there has been an increasing interest in the quantitative study of the elemental and molecular composition of biomolecules and their distribution in biological and environmental samples. Regarding the elemental composition, inorganic mass spectrometry and in particular ICP-MS is today the reference technique for establishing the elemental composition and distribution of species (speciation), especially to study the processes of metallic species (or with a heteroatom) in an organism or to evaluate the extent and impact derived from possible environmental contamination produced in

biological systems. With respect to the molecular composition of biological samples, organic or molecular mass spectrometry (MALDI and ESI-MS), using the soft ionization of biomolecules for the analysis of biopolymers, is currently one of the most powerful analysis tools (although the sensitivity of molecular mass spectrometry techniques is still insufficient in relation to the need to define biological processes at the cellular level).

1.1.3.1 Elemental Mass Spectrometry

The analysis of the total elemental content of a biological sample (e, g, fluids such as blood, serum, urine, a section of tissue, organ, etc.) can be performed in some cases directly or, generally, after mineralization to dissolve the metals and eliminate the organic matrix using sensitive and selective atomic techniques for the elemental determination at the trace level (Atomic Spectrometry techniques).

Undoubtedly, Inductively Coupled Plasma Mass Spectrometry (ICP-MS) is today the most powerful and appropriate technique for this purpose. ICP-MS was introduced as an analytical technique by Houk *et al.* [15] in the early 1980s. Although the basic design has not changed, the important improvements in terms of detection limits, linear detection dynamic range and robustness have established the ICP-MS as one of the main techniques for the analysis of trace elements and ultra-trace in organic, inorganic and biological samples [16]. Thanks to its characteristics such as low detection limits, practically independent of the chemical form in which the elements are found and of the sample matrix; its capacity for multielement and multi-isotopic determination; and its high dynamic range, make it the elemental detection technique of choice for a multitude of studies [17].

1.1.3.2 Inductively coupled plasma mass spectrometry

When classifying and quantifying elements, it is extremely important to minimise signal interferences and be able to compare acquired signals to a real quantity such as concentration. With ICP-MS, there are numerous constraints which will be covered in this thesis.

The elemental sensing range of ICP-MS is between 7 to 250 amu (lithium to uranium) but only for elements with stable positive ions within that range [18]. Also, due to the

use of argon as a carrier gas in most systems there are numerous spectral interferences with the mass analyser which can confound the signal [19]. There are various types of ICP-MS with differing methods of ion separation to maximise mass resolution, increase sensitivity and minimise interferences. The main varieties are single quadrupole, triple quadrupole, time of flight (TOF) and multicollector (MC). Single and triple quadrupole ICP-MS operate in a similar linear fashion where ions are cyclically manipulated using magnetic multipoles, filtering in an octopole first then focusing using a quadrupole, all after being ionised in the plasma. Triple quadrupole ICP-MS differs by having an additional quadrupole placed after the filtering octopole which allows for the reaction of gases with the ion stream to assist with the filtering of interferences. MC and TOF analysers use trajectory arcs through a large magnetic field to separate and detect ions of different mass to charge ratios. Where TOF analysers collect the full range of ions to detectors MC analysers position faraday cups at specific positions correlated to specific ions masses for detection[20]. An ICP-MS quantifies elements by counting the number of signals of a given mass per time period. Particles are lost either via bonding with contaminants or condensation when they travel the distance between the laser ablation and the ICP-MS. An amount of time is required to register particles that flow through the system. This sampling time is a limitation for the quantification and accuracy. The sampling periods of different elemental masses are measured consecutively meaning that portions of sample are not all measured equally both relative to each other and the sample. To overcome these constraints a calibration standard is used [21].

A calibration standard in the context of an ICP-MS is a material or element of known parameters that may be introduced either external or internal to the experimental sample. The calibration standard undergoes the same analytical regime as the experimental sample either combined with the sample (internal) or in parallel to the sample (external) and any limitations in the system affect both standard and sample. The final signal is then compared to an independent measurement of the concentration of the element of interest in the calibration standard and signal is corrected. The major advantage that makes this method suitable for research use in areas such as biomarker discovery and pharmaceuticals is that the quantification is absolute. This means that the

final concentrations are gauged to a benchmark outside the sample allowing for comparison of replicates and different samples without artefacts.

A calibration standard requires several attributes for optimum performance. It must be homogeneously dispersed, either externally or internally to the sample. The element or elements which comprise the calibration standard cannot interact or overlap with those under investigation; ideally being unique to the specimen. Finally the standard should not affect the condition of the material under investigation and, if possible, be simple to apply [22]. Due to this condition of minimum tampering of the sample to minimise previously published [23] loss of elements from processing steps external standards are preferable. External standards are calibration standards that are separate from or external to the experimental sample. There are numerous external standards, each developed for specific experimental conditions.

It has been demonstrated that the ICP-MS is the most powerful detection technique for the analysis of trace and ultra-trace element comprising several advantages such as: high sensitivity, low mass interferences, great dynamic range and the capacity of the multi-elemental and isotopic analysis. Precisely the easy coupling of ICP-MS to efficient separation techniques (such as high-resolution liquid chromatography (HPLC), gas chromatography (GC) and capillary electrophoresis (CE)) with ICP-MS has opened up possibilities the path for the use of "hyphenated" techniques capable of offering qualitative and quantitative elemental speciation with high sensitivity and selectivity.

In addition to the analysis of aqueous solution elements (for example, after digestion of biological and environmental samples), ICP-MS analysis of biological and environmental samples "in-situ" is also possible using laser ablation (LA) combined with ICP-MS. This coupling allows the direct sampling of solids and provides analysis with high spatial resolution in the μm range, as we will see in following sections of this Thesis.

1.1.4 Elemental bio-imaging techniques

Nowadays, there is a wide variety of bioimaging techniques available for research in biology, pharmacology and clinical sciences, as well as for routine analysis. Frequently, "in vivo" and "ex vivo" studies using imaging methods are carried out in order to clarify

the mode of action and side effects of the drugs, to evaluate the toxicity of certain materials and / or to understand the development of diseases.

Elemental bio-imaging (EBI) is a class of analytical techniques which gather both spatial and elemental data in biological specimens. They have high spatial resolution (10-100 μm) and elemental sensitivity ($\mu\text{g}\cdot\text{g}^{-1}$) [24] allowing localization of trace elements to structures within a tissue (Figure 1.1).

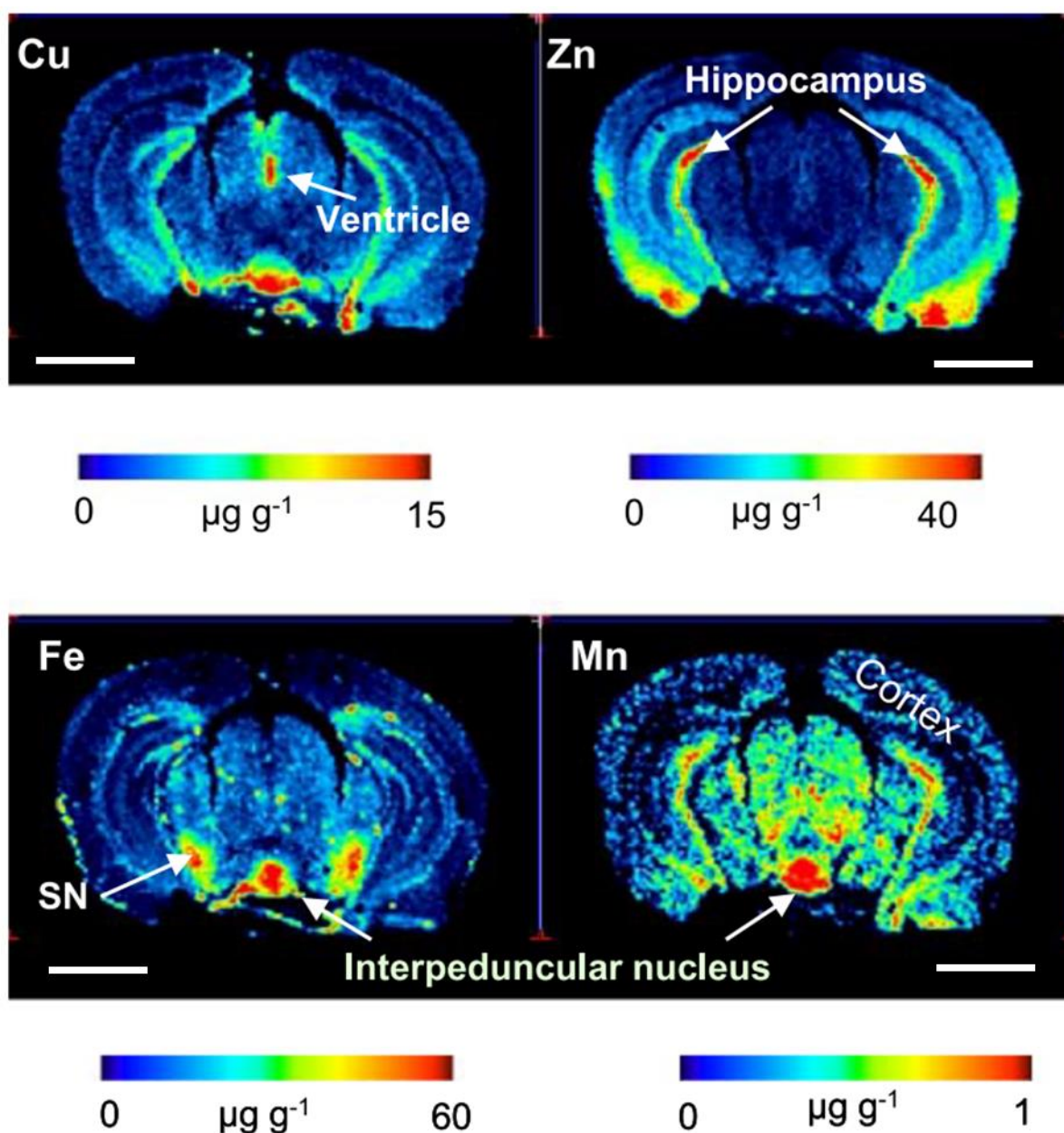


Figure 1.1: Bioimaging of four transition metals (Cu, Fe, Zn and Mn) in mouse brain by LA-ICP-QMS imaging, scale bar 2mm. [24].

In recent years the direct quantitative analysis (with a minimum sample preparation) of the elemental spatial distribution in a solid sample, such as a thin section of biological tissue, using elemental microanalytical imaging techniques has been addressed. This possibility is interesting, given that it provides detailed and highly reliable information on the precise and quantitative location of metals in biological tissues and opens the door to the selection of regions and samples of interest for subsequent metallomic studies

focused on the identification of metal-biomolecule complexes. Based on its physical foundation (with different spatial resolution and sensitivity), the most commonly used elemental bioimaging techniques are X-ray fluorescence (XRF), secondary ion mass spectrometry (SIMS), laser-induced breakdown spectroscopy (LIBS) and laser ablation (LA) coupled to an ICP-MS (LA-ICP-MS).

The resolution, elemental sensitivity and experimental requirements for the different techniques restrict their use to suitable types of samples. X-ray fluorescence (XRF) has high spatial resolution (~100nm) but it is limited by strong matrix effects which interfere with sample quantification [25,26]. Sample preparation is also cumbersome requiring cryogenesis before the sample is mounted on a substrate [27]. These combinations of issues restrict the elemental sensitivity of XRF to 100-1000 $\mu\text{g/g}$. SIMS has greater spatial resolution (~50nm) and is elementally sensitive to 0.1 $\mu\text{g/g}$ in most biological samples. However due to the shallow penetration depth (0.2-10nm) of this technique analyses are generally restricted to the surface or single position depth profiling [28]. LIBS has high resolution of up to 6 μm [29] and elemental sensitivity of 1-10 $\mu\text{g/g}$ while remaining a method capable of full sample analysis. Its limitation is in the high energy laser powers (an order of magnitude higher than LA-ICP-MS) used which causes thermalisation of the sample potentially changing spatial distribution of elements [30]. LA-ICP-MS like LIBS is a technique of analysing the whole of a sample with resolution of 5.0 μm and elemental sensitivity of 0.01 $\mu\text{g/g}$ with LIBS having superior sensitivity to lighter elements (C,N,O). Counter to the high power laser of LIBS, LA-ICP-MS only requires enough laser power to aerosolise the sample which is far lower thereby minimising the thermal issues mentioned previously [31].

It is precisely the combination of laser ablation with inductively coupled plasma mass spectrometry (LA-ICP-MS), first introduced by Gray in 1985 [32], perhaps the most promising and sensitive technique, for elemental bioimaging, allowing multielement analysis and the measurement of the isotopes ratio (at trace elements and ultra-trace levels) with high spatial resolution and good quantitative analysis capacity.

1.1.4.1 LA-ICP-MS: fundamentals, principles and fields of application

A conventional LA-ICP-MS setup (as seen in Figure 1.2) uses a high powered laser (of a nanosecond or shorter pulse) to ablate a sample in a given pattern (usually a rastered line) while constantly flowing an inert gas (either argon, helium or a mixture) over the sample to sweep the ablated plume into an inductively coupled plasma mass spectrometer (ICP-MS). The inductively coupled plasma is created from carrier gas being driven through an electromagnetic field generated by a high voltage radio frequency generator. Particles are stripped of their electrons and accelerated towards the mass spectrometer. A reaction cell is used to discard isobaric interference from the mass analyser so that the recorded signal is uncorrupted. Finally, the stream of positive ions is separated using magnet field oscillation by a quadrupole and detected by the mass analyser [33]. The data is then spatially resolved allowing analysis of the detected species in two and three dimensions.

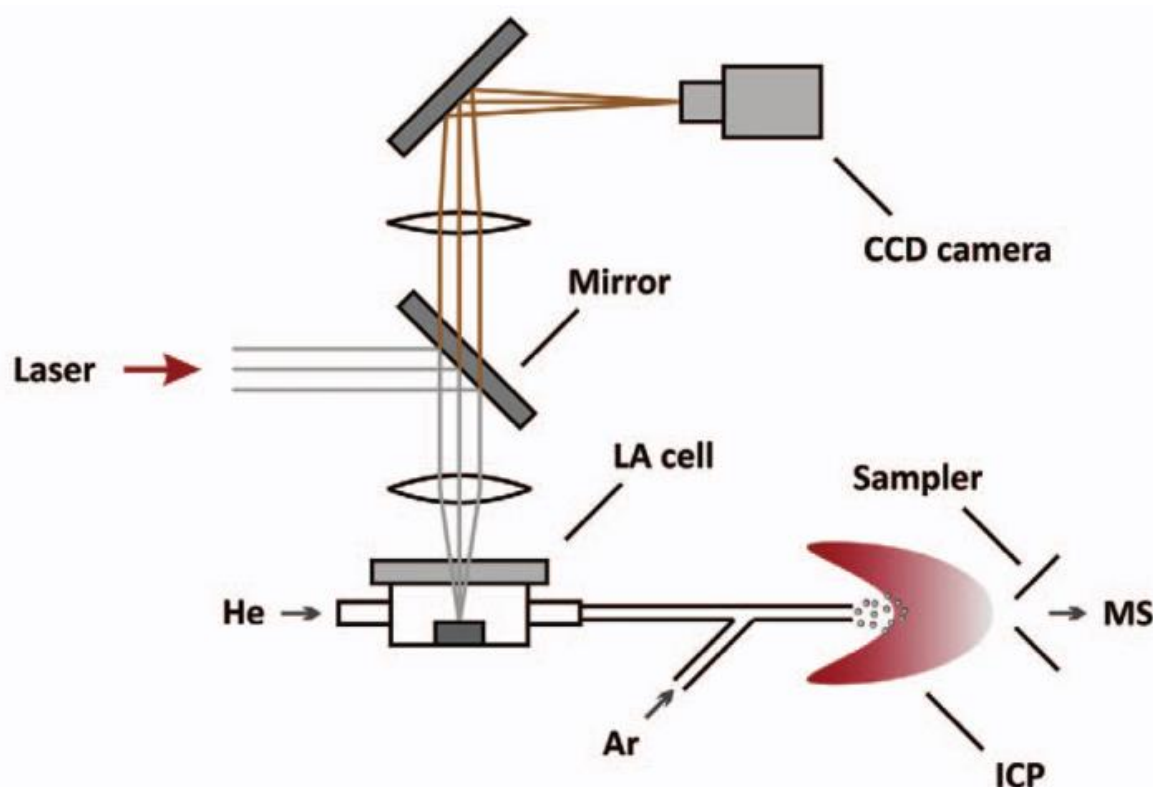


Figure 1.2: Laser ablation inductively coupled plasma mass spectrometry schematic using a helium and argon gas system [33].

LASER is an acronym for Light Amplified by Stimulated Emission of Radiation. Lasers work by the exciting (conventionally with high voltage electricity) either a solid (solid

state) or a gas such that ground state energy electrons are promoted to a higher “excited” energy level; these electrons prefer to be in the ground state so in order to remove this surplus energy light is emitted as the electron transitions back to the ground state [34]. The difference in energy between the excited and ground state influences the wavelength of light emitted as per de Broglie’s famous derivation $\Delta E = h\nu$ [35]. Different wavelengths have been used for lasers, ranging from infrared (IR) to ultraviolet (UV). Due to high absorbance in all medium, UV lasers such as: Nd: YAG (yttrium garnet and aluminium doped with neodymium) at wavelengths of 266nm and 213nm, and the excimer laser (gas laser, ArF) at 193nm, are the most widely used.

One of the crucial advantages of the LA-ICP-MS technique is the acquisition of quantitative elemental data but this is limited by the requirement of calibration standards [36]. There are also equipment based restrictions to the accuracy of LA-ICP-MS which will be discussed in the following sections [37].

1.1.4.1.1 Laser Ablation limits

The interaction of the laser and the substrate has a major impact on the quality and accuracy of the signal collected. The quantity of ablated material is dependent on thickness, density and flux of the laser [38]. There is a delicate balance between having sufficient laser fluence to ablate material, and enough to avoid the roll-off point [39]. The roll-off point occurs when the laser energy transferred to the sample is so high that a plasma cloud is formed in the laser path. This plasma cloud shields the sample from the incoming laser thereby reducing ablation efficiency which can be severely detrimental to data collection [40].

The minimum possible laser spot size that will ablate the sample should be used for increased spatial resolution and elemental detection, [41]. The resolution of a laser system is dependent on the diffraction limited relation displayed in Equation 1.1. For LA-ICP-MS, wavelength is the most important variable for improving resolution and therefore ultraviolet lasers are used [42]. Given this equation and a standard UV laser wavelength of 193nm this resolution limit is sub-micron ($\sim 0.32\mu\text{m}$) which is lower than the minimum spot size for a commercial laser ablation system ($\sim 1\mu\text{m}$).

$$r = \frac{4f\lambda}{\pi D}$$

Equation 1.1 Diffraction limited relation [43], where r = resolving length, f =focal length, λ =wavelength and D =beam diameter

Another aspect of importance is the pulse width of the laser. Due to the high energy transfer from laser to sample there is a significant heat conduction factor through the sample. Minimisation of heat transference away from the ablation site is key, because of excess energy (causing signal roll-off) and the role of heat in driving diffusion. A solution to minimise heat transfer is the pulse width which can be reduced from nanosecond to femtosecond. The femtosecond laser dwell time is generally shorter than the heat transfer mechanism of most materials. As can be seen in Figure 1.3, ablation site secondary effects are reduced when femtosecond lasers are used [44].

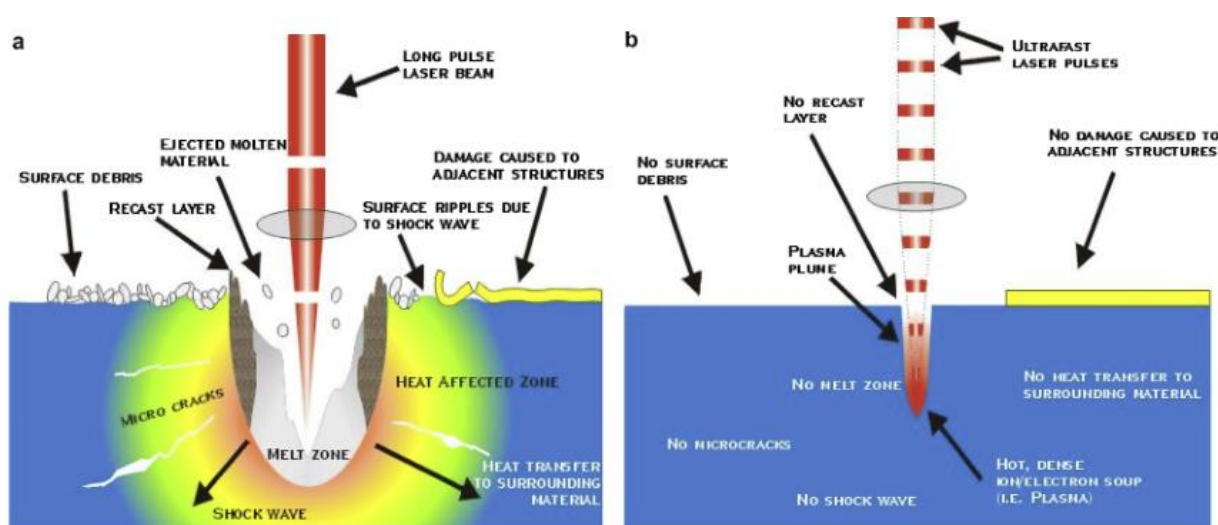


Figure 1.3: Comparison of ablation spot between a) nanosecond and b) femtosecond pulse width LA-ICP-MS systems [44].

The final restriction for laser ablation considers the speed at which the ablated material is transported to the ICP-MS. This metric is called washout time and is improved through ablation cell design. There are three major designs which are all small volume cells with high pressure gas flow in different formats. The philosophy of these “fast” washout cells is that with faster transport of sample to the ICP-MS there are less sampling artefacts and the laser can be run at faster scanning speeds for shorter experimental time [45].

1.1.4.1.2 Quantification strategies by means of LA-ICP-MS

Elemental bioimaging by means of laser ablation coupled to inductively coupled plasma mass spectrometry (LA-ICP-MS) is a technique for the investigation of elemental distributions in the tissue sections and provides high spatial resolution, excellent sensitivity and the possibility of quantitative imaging.

The quantification and calibration of elemental imaging by LA-ICP-MS has been extensively reviewed by Hare *et al.* [46] and the different strategies for the quantification of elements in biological tissues include: internal standardization (IS) where a naturally occurring element is used to calibrate [37], external calibration where elements are doped into an external medium and cross calibrated to the sample [47], online standard addition where known concentration of an element is added in liquid form to the flow of material from laser to ICP-MS [48,49], isotopic dilution where a known concentration of an isotopically enriched element is doped into the sample [50,51], matrix-matched standards where the external standard medium is manufactured from the matrix of the sample [52], and other methods such as film coating where metals are sputtered onto the sample to serve as an IS [53], or printing where either an IS or enriched isotope is applied using an inkjet printer [54]. Due to the biological nature of the samples in this thesis, only external calibration methods are discussed as they effect sample structure or elemental distribution less than internal standard methods.

A certified reference material (CRM) is a commercially produced external standard derived from various materials. Its parameters are thoroughly specified and can vary from pig liver [55] to glass [56]. The limitation of these types of external standards are in the non-uniform manner of application and the relative concentration of the reference material compared to that of the investigated material [57]. For this reason, there is a limited selection of CRM which are of use for LA-ICP-MS quantitative imaging.

Spin coated poly(methyl methacrylate) (PMMA) films doped with ruthenium, yttrium, copper and zinc allowing a soft tissue to be deposited on top of the sample as a thin film is one approach [58]. The homogenous application of PMMA via spin coating largely addressed the application issues of CRMs. For this method, the standards are applied under the tissue; therefor higher ablation powers are required and may intersect with at

the roll-off point. Additionally, PMMA cracks when stored in a fridge and possible incomplete homogenisation. Beryllium, manganese, cobalt, rhodium, tantalum, tungsten and rhenium spiked agarose gels have been used in a similar manner to PMMA. This method also requires total ablation of specimen which exacerbates the thermal issue mentioned early in this chapter [59].

Another method taken from thin film manufacturing is the evaporative deposition of gold. Unlike the CRM and thin film methods, this technique applies gold to the surface of a sample with great uniformity. However, evaporative deposition requires high vacuum conditions which are not compatible with many biological samples. Unlike doping or spiking of materials, the concentration of gold from deposition is very high compared to trace elements in the sample, due to the 9nm thickness of the gold coating [60]. This mismatch between the concentration of the calibration standards and the analyte of interest can result in inaccuracies [57].

Most quantitative studies have relied upon the preparation of matrix-matched laboratory standards. This matrix matched external standard approach was developed specifically to address the effects of non-analyte components or chemical matrix effects. These are external standards constructed with homogenised tissue of the same organ and animal as the sample spiked with elemental salts. An example matrix matched calibration was fabricated using homogenized brain tissue doped with cobalt, copper, iron, magnesium, manganese, strontium, selenium and zinc [52]. The homogenate is analysed within the same experimental cycle as the specimen to account for signal variation from laser fluence fluctuation during a LA-ICP-MS run. The only weakness of these standards is when samples contain lower concentrations of element than is endogenous to the matrix matched standards source tissue. To improve upon matrix matched standards a replacement would need little to no endogenous elements of interest for LA-ICP-MS while also maintain equivalent ablation behaviour as tissue.

Elemental bioimaging has recently matured into the best array of tools to investigate the fundamental interactions of biological systems. Of the various techniques LA-ICP-MS is the most suited due to the transition metals involved and the concentrations at which they are present. LA-ICP-MS also allows for accurate and sensitive quantification of both

endogenous and exogenous metals. It is compatible with current immunohistochemistry processes and allows other staining protocols to be developed.

1.1.4.1.3 Applications of LA-ICP-MS

Elemental bioimaging through LA-ICP-MS has evolved rapidly to become the method of choice for a wide variety of biological and medical samples. Elemental bioimaging of endogenous and exogenous metals have been used to construct a metal profile of single cells [61] or testing a Zebrafish embryo model for ecotoxicology [62]. Metals such as copper also have major roles in Menkes disease [63] and Wilson's disease [64] which have been studied using animals models and human samples to improve diagnostics and test treatments. Metals used in treatment were generally assumed to naturally pass through the body without accumulation apart from in specialised cases. However EBI revealed that some metal containing treatments such as anticancer agents [65], magnetic resonance imaging contrast agents [66] and antibacterial silver nanoparticles [67] bioaccumulated in some cases over the course of a lifetime.

More recently has been the usage of rare earth metals tagging agents in immune-based research as an alternative to fluorescent and radioactive tags. Two recent examples are tagging metallothionein in ocular tissue [68] and single cells tagged with metals in 3D [69] showing the breadth of which these newer immune-tags can be used in biological systems.

1.1.4.2 Immuno-Mass Spectrometry Imaging and beyond

LA-ICP-MS has been successfully used for the measurement of heteroatoms which are directly associated with proteins in tissues in a wide variety of applications. To apply this technique for the analysis of biomolecules, which do not have detectable elements, naturally present in their structure, labelling strategies with a metal or heteroatom tags can be employed as a promising tool.

The potential of immunoassays with an element-tagged antibody in combination with LA-ICP-MS detection for multiplexing assay has been demonstrated in several applications. The introduction of antibodies tagged with rare earth elements to spatially and quantitatively map specific epitopes was first demonstrated on β -amyloid peptide

by Hutchinson *et al* in 2005 [70]. Since then in the field of neurology, this process has allowed the measurement of changes in the distribution of trace metals in the brain. Studies co-localising iron and the neurotransmitter dopamine in rodent models of neurodegeneration have provided solutions to problems about the aetiology of Parkinson's disease, which had remained unresolved for a century because of analytical limitations [71].

Using LA-ICP-MS to analyse antibody probes tagged with metals to incubate tissue samples thereby localising the metal probe to the epitope of interest is increasingly referred to as immuno-mass spectrometry imaging (iMSI). Compared to conventional IHC fully quantitative maps may be easily constructed from LA-ICP-MS analysis but currently at lower resolution than optical techniques [72].

Probes have progressed in the last 50 years as new biological agents have been discovered. Antibodies were the first probe produced predominantly widely used for identification of species in biological samples. These are produced in either whole animals or hybridoma cells lines [73] and can be produced to a large number of molecules provided they are immunogenic or can be made immunogenic by conjugation techniques [74]. Since then a number of selective binding agents have been discovered (e.g. Messenger RNA) [75–77], or synthetically manufactured such as spirooligomers [78–80], which are synthetic oligomers made by coupling pairs of bis-amino acids into a fused ring system. However, recently a class of molecules with the ability to be functionalised and which have the potential to bind with high specificity to small and large biological and chemical targets have been developed. These are usually short synthetic sequences of RNA or DNA called aptamers [81].

Structurally antibodies and aptamers differ vastly, most obviously in physical size with an antibody being around 150 kDa where as an aptamer is generally around 30 kDa as illustrated by Figure 1.4 [82]. This has the advantage of allowing more rapid tissue penetration [83]. The production method for aptamers also means they have a larger range of targets as they are produced by amplification of sequences with high affinity for the target from extensive random libraries of nucleic acid sequences. This has the further advantage that target compounds which have low immunogenicity can be used to produce aptamers with exquisite selectivity able to differentiate even between chiral compounds [84].

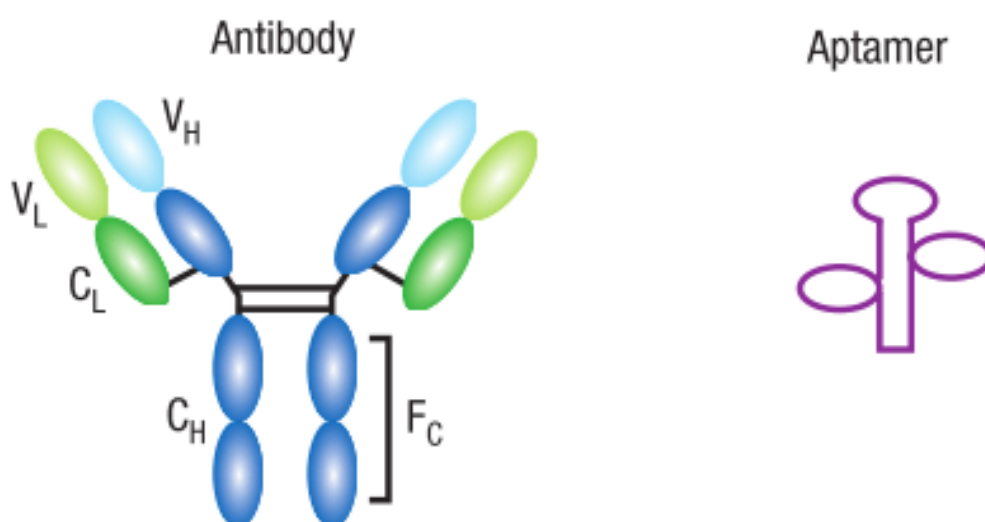


Figure 1.4: Comparison of antibody and aptamer structures [85].

Polyclonal antibodies are produced *in vivo* by repeatedly challenging a host with the target antigen and then purifying the desired antibody from the serum, or for production of monoclonal antibodies, using complex cell culture techniques to produce hybridomas [73]. The architecture of an antibody allows signal amplification where antibodies against the species specific Fc (fragment crystallizable) portion of a primary antibody may be exploited in a secondary labelling approaches as illustrated in Figure 1.5 [86]. Aptamers are generally more chemically and thermally robust than antibodies but those

derived from RNA are very susceptible to enzymatic degradation compared to antibodies [87].

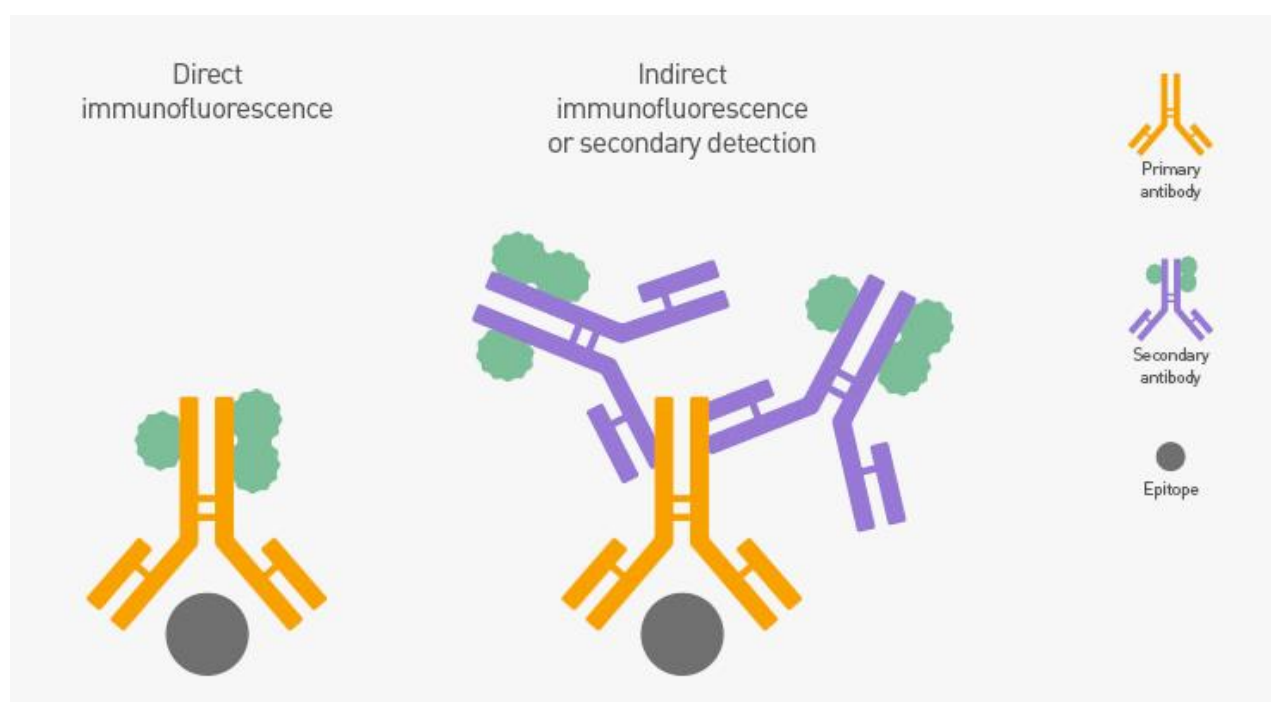


Figure 1.5: Schematic of indirect immunolabelling using fluorescent tagging [88].

Overall both antibodies and aptamers have their relative advantages and disadvantages. The advantages of each can be exploited by using the two types of probe both singly and in tandem when creating protocols for investigating tissue samples allowing greater flexibility and a larger range of epitopes to be examined.

1.1.5 Tagging agents

Biological research often requires the use of molecular labels that are covalently attached to a protein of interest to facilitate detection or purification of the labelled protein and/or its binding partners. Conventional tags include fluorescent labels or enzymatic/colorimetric labels. Fluorescent tags generally comprise of a fluorescent protein or molecule which emit light when excited by photons [89]. The most widely used tagging systems are enzymatic/colorimetric such as horse radish peroxidase, which takes advantage of colour development usually by an enzymatic reaction where the absorbance of light is used to measure signal intensity [90]. This immunohistochemical

analysis by using insoluble chromogenic products cannot be quantified so comparison between samples is accomplished only by observation of positive versus negative areas of staining [91].

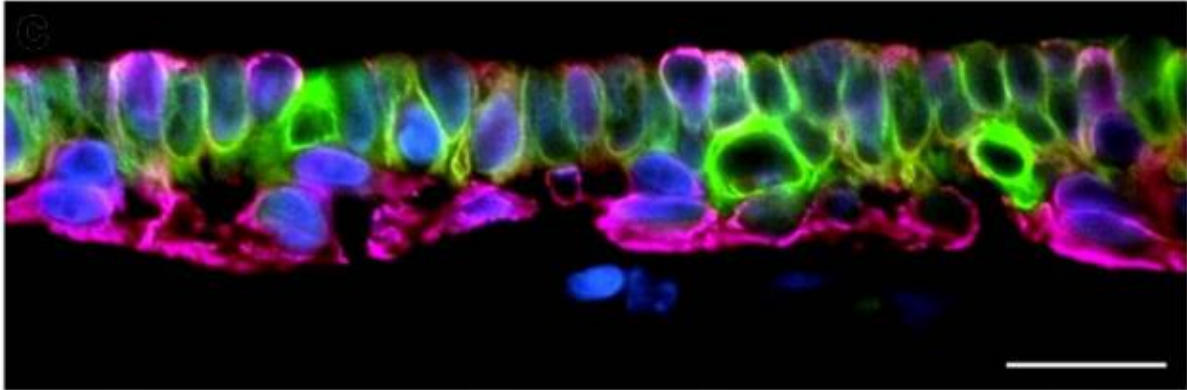


Figure 1.6: Double immunolabeling of two cytokeratins, Ck14 (IgG3) and Ck8/18/19 (IgG1), in a duct wall of the human mammary gland (Twenty micrometers scale bar and colours are for Ck8/18/19 (a, FITC, green), Ck14 (b, Alexa-647, pink) and for nuclei (DAPI, blue) [86].

A major class of tags for antibodies and nucleic acid probes are fluorescent molecules such as fluorescein isothiocyanate (FITC), green fluorescent protein or DsRed [92]. Fluorescent tagging works by exciting the fluorescent molecule/protein with photons of a specific wavelength thereby inducing emission of photons of another wavelength. For immunohistochemistry, these fluorescent molecules have the advantage of being used for analysis of multiple analytes (“multiplexing”) in a single tissue specimen. The majority of literature describe double labelling and then usage of a direct tissue stain usually 4',6-diamidino-2-phenylindole (DAPI) for contrast (as seen in Figure 1.6). The process of fluorescence varies between tags due to the number of excitation-emission pathways making quantification difficult [93]. For absolute quantification via fluorescent tags excitation must be standardised for each fluorescent tag, as well as accounting for secondary optical effects such as scattering [94]. Further, spectral overlap limits the number of targets that can be simultaneously determined.

Nanoparticles are a new class of tags comprised of nanosized collections of elements coated in easily functionalised compounds. Nanoparticles can be detected using multiple methods due to their fluorescent, colorimetric or combined nature, and is dependent on

size and elemental composition [95–98]. They overcome the issues present with other fluorescent tags with customisable quantum properties allowing for a system which does not have multiple excitation-emission pathway and spectral overlap issues [99]. However, all this customisability does not come without restrictions. They have blinking issues or are too large to enter cells of interest [100–102]. While this area has excellent potential to monitor practically any system using various binding chemistries, it has not been tested extensively.

The experiments performed in this work will be focus on the use of lanthanides as tagging labels. Specific elemental tags with little to no natural occurrence in biological systems are attached to probes and detected using mass spectrometry [103]. MaxPar™ reagent is a proprietary polymer based elemental tag which uses lanthanide group elements commercially available by Fludigm [104]. There are also many other options such as 2-(4-isothiocyanatobenzyl)-1,4,7,10-tetraazacyclododecane-1,4,7,10-tetraacetic acid (SCN- DOTA) or metal-coded affinity tags (MeCAT) [105], which takes advantage of traditional analytical chemistry standardisation techniques [46]. They are also easily attached to probes such as antibodies (as seen in Figure 1.7) with flexibility to be used concurrently.

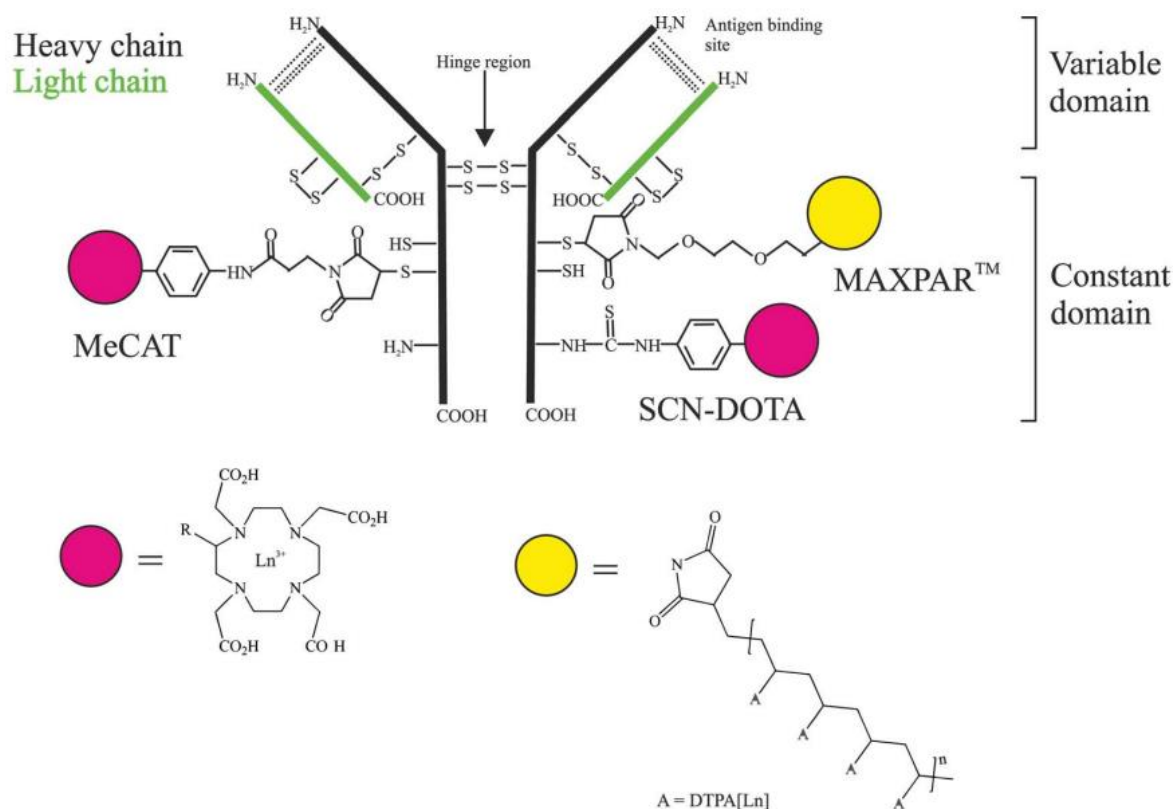


Figure 1.7: Scheme of selected bi-functional ligands used as labelling reagents and their binding to amino acids of an antibody. The SCN-DOTA covalently binds to 3-amino groups of lysine residues. The other opportunity shown here is the labelling via a maleimide group which binds to the sulfhydryl residues after partial reduction of the antibody's cysteine-based disulfide bridges. MeCAT and SCN-DOTA contain a DOTA macro-cycle (pink circle) to complex lanthanide ions whereas the MAXPAR polymer chain contains many DTPA residues as chelating compounds (yellow circle).

Antibodies and aptamers are the most flexible probes and may be applied to small molecules as well as protein species and may be used in conjunction with elemental tags. Elemental tagging allows the use of ICP-MS to give the required ability to identify, quantify and spatially resolve multiple interrelated targets in tissue sections which would not be accessible using conventional optical microscopy.

1.1.6 Image processing

LA-ICP-MS imaging resolution is currently restricted by beam diameter as was historically the case for optical imaging techniques. This limitation in optical microscopy spawned the field of imaging science which focuses on surpassing the resolution limit while also minimising the artefacts created by new methods of processing. Most tools

from this field have not been tested with LA-ICP-MS imaging due to the mismatch between the medium of analysis: photons and other electromagnetic waves for imaging science [106–108]; aerosolised elements and compounds for LA-ICP-MS [109]. The other shortcoming is that LA-ICP-MS is a destructive technique which discounts conventional multi-image reconstruction algorithms for resolution improvement which use tens to thousands of images to recreate a single image [110,111]. Despite this limitation reconstruction is a viable strategy for LA-ICP-MS as it does not depend on inherent properties of electromagnetic waves.

Super resolution reconstruction (SRR) is an established technique in geographical and biological imaging fields [112–114] based on using multiple lower resolution images to build a higher resolution reconstruction, illustrated by Figure 1.8. The higher resolution reconstruction requires an interpolation algorithm to populate pixels not filled by the lower resolution images. There are several interpolation strategies used in current SRR algorithms such as linear, cubic and nearest neighbour interpolation [115]. Within the EBI field, SRR has only been used in Air Flow-Assisted Ionization Mass Spectrometry Imaging by Tang *et al* [116] on rat brain and kidney sections. Their study concluded that the application of the super-resolution reconstruction technique, based on sparse representation for Mass Spectrometry Imaging (MSI), was feasible and effective.

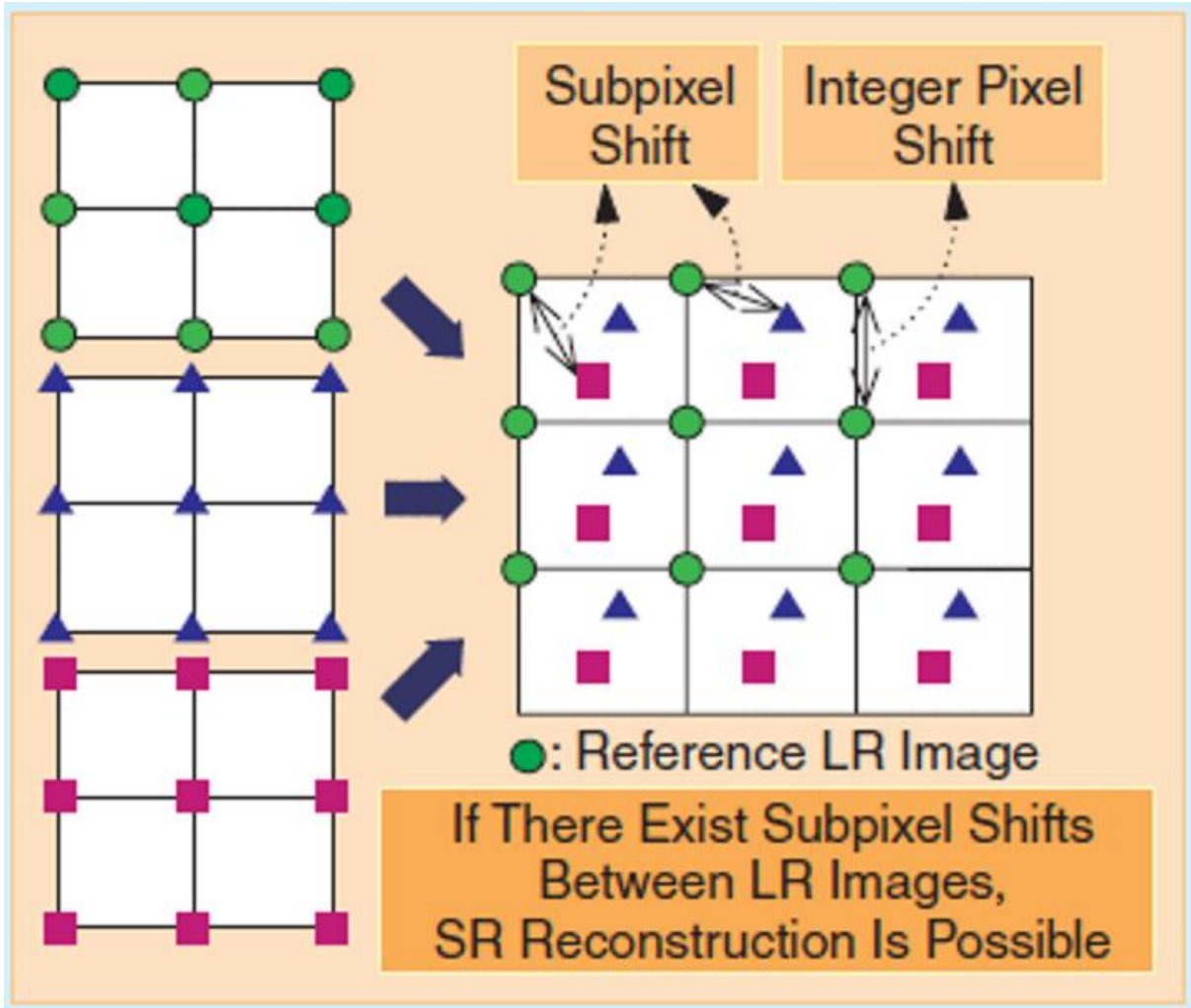


Figure 1.8: Illustration of the basic principle of Super Resolution Reconstruction.

Currently most LA-ICP-MS applications are acquired under conditions where $v_l = \frac{x_s}{t_{sc}}$ Equation 1.2 , where v_l is the scan velocity, x_s is the laser spot size and t_{sc} is the integration time, developed by Lear *et al*[38] to maintain the original dimensions of bio-images. Herrmann *et al.* [117], Drescher *et al.* [118], Mueller *et al.* [119], Theiner *et al.* [120] and Niehoff *et al.* [121] have published various papers that use anisotropic pixel dimensions which violate this equation in order to improve the resolution in the scan direction. This anisotropic pixel regime share similarities with an anisotropic orthogonal super resolution reconstruction method for magnetic resonance imaging [122]. Combining these two methods, we propose a super resolution reconstruction method for LA-ICP-MS using 2 consecutive raster scans taken in orthogonal directions as illustrated in Figure 1.9.

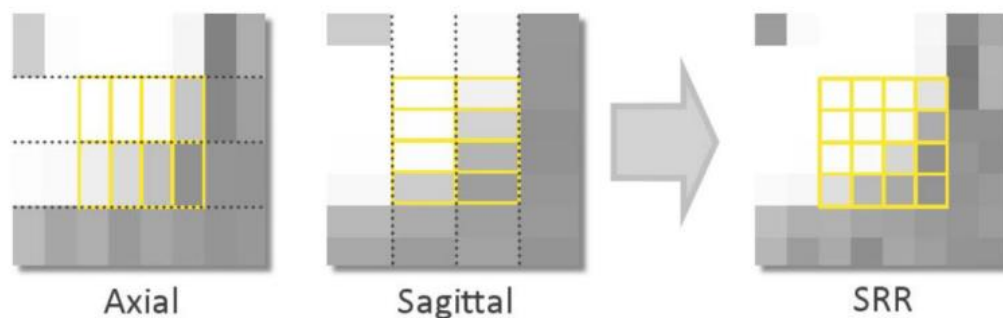


Figure 1.9: Scheme illustrating the super-resolution reconstruction from the acquisition of two orthogonal thick slices [122].

Higher resolution images allow comparison between LA-ICP-MS data and other similarly resolved images. This analysis between optical, elemental and structural data is complex and requires tools to correlate, interrogate and apply statistical calculations in parallel. LA-ICP-MS data is not considered a default type for import into the tools currently used by the biological sciences. There remains a gap where a program or workflow which can bridge LA-ICP-MS to fields such as optical microscopy or tomography.

1.2 Thesis aims

This thesis encompasses the development of tools and processes to improve elemental bioimaging and iMSI by LA-ICP-MS.

The aims of this thesis are to:

1. Develop external calibration standards equivalent to matrix matched standards with lower background for all elements with the following objectives:
 - a. Development of a method for fast and simple manufacture of external calibration standards from gelatin
 - b. Comparison of the analytical figures of merit of gelatin standards against conventional matrix matched standards
 - c. Use profilometry to compare physical characteristics of each standard type

2. Evaluate image processing algorithms on LA-ICP-MS specifically super resolution reconstruction for resolution improvements with the following objectives:
 - a. Adapt super resolution reconstruction algorithms for LA-ICP-MS
 - b. Improve resolution of images
 - c. Optimise experimental parameters for resolution improvement
 - d. Compare quantitative characteristics of super resolution reconstruction to conventional LA-ICP-MS

3. Quantify dystrophin in murine quadricep tissues using super resolution reconstruction with the following objectives:
 - a. Evaluate conventional and SRR LA-ICP-MS on metal tagged dystrophin antibody for quantification of dystrophin in murine quadriceps
 - b. Interrogate a mouse model of Duchenne's muscular dystrophy using novel immuno- mass spectrometry imaging protocol for diagnostics
 - c. Compare immuno-mass spectrometry imaging protocol on human quadricep samples
 - d. Acquire 3-dimensional SRR images of murine quadriceps to explore the possible heterogeneity of dystrophin expression in the z-axis

4. Compare antibodies and aptamers as probes for the quantification of target epitopes with the following objectives:
 - a. Confirm binding of aptamers and antibodies for myelin basic protein
 - b. Evaluate direct and indirect labelling protocols
 - c. Stain murine brain samples with tagged aptamers for comparison of elemental and fluorescent tagging agents using optical microscopy and LA-ICP-MS

2 Materials and Methods

All experiments were carried out within the Faculty of Science at the University of Technology Sydney and the David Geffen School of Medicine at the University of California, Los Angeles.

2.1 Instrumentation

2.1.1 Solution nebulization inductively coupled plasma mass spectrometry

All solution nebulization inductively coupled plasma mass spectrometry (SN-ICP-MS) were performed using 7500cx and 7700x series ICP-MS (Agilent Technologies, Waldbronn, Germany)(Figure 2.1) equipped with a micromist™ concentric nebuliser (Glass Expansion, West Melbourne, Australia) and a Scott type double pass spray chamber cooled to 2°C used for sample introduction. Platinum sampling and skimmer cones were used. The 7500cx ICP-MS was controlled by Agilent Technologies ICP-MS Chemstation software (B.03.07) and on a Hewlett-Packard (Hewlett-Packard Palo Alto, CA) desktop computer via a category 5e ethernet cable. The 7700x ICP-MS was controlled by Agilent Technologies ICP-MS MassHunter 4.3 software (C.01.03) and on a Hewlett-Packard (Hewlett-Packard Palo Alto, CA) desktop computer via a category 5e ethernet cable. All experiments used 99.9995% ultra-high purity liquid argon (Argon 5.0, Coregas Pty Ltd, Yennora, NSW, Australia).

SN-ICP-MS was used to analyse digested standards. An Agilent integrated autosampler (AIS) was loaded with solutions for analysis. Solutions were transferred



Figure 2.1: Agilent 7500cx (left) and 7700x (right) Series Inductively Coupled Plasma Mass Spectrometer fitted with Agilent Integrated Autosampler [124].

to the ICP-MS using a 1.02 mm internal diameter Tygon tubing and a three channels peristaltic pump. The solution was pumped at a continuous flow of 1.0 mL.min⁻¹. A 100 ppb Rhodium solution in 1% HNO₃ was used as an internal standard and introduced into the analyte flow via a T connector post-pump. The solution was delivered to the plasma of the ICP via a Micromist nebulizer and Scott type double pass spray chamber. The typical ICP-MS conditions can be found in Table 2.1.

Table 2.1: Typical ICP-MS parameters for SN-ICP-MS.

	Agilent 7500cx SN-ICP-MS	Agilent 7700cx SN-ICP-MS
Sample introduction		
RF power (W)	1500	1500
Carrier gas flow rate (L min ⁻¹)	0.85	0.7
Makeup gas flow rate (L min ⁻¹)	0.15	0.5
Sample depth, mm	8	8
Ion lenses		
Extracts 1, 2 (V)	4.5, -170	3.8,-185
Omega bias, lens (V)	-26, 2.4	-120,18
Cell entrance, exit (V)	-50,-68	-30,-40
Octopole parameters		
Octopole RF (V)	185	190
Octopole bias (V)	-6	-8
Collision gas, flow rate (mL min ⁻¹)	0	0

2.1.2 Laser ablation inductively coupled plasma mass spectrometry

Laser ablation inductively coupled plasma mass spectrometry (LA-ICP-MS) was performed using a New Wave Research NWR193 (Kennelec Scientific, Mitcham VIC, Australia) ArF excimer laser with an Agilent 7700x ICP-MS (Agilent Technologies, Waldbronn, Germany) (Figure 2.2). The ICP-MS instrument was fitted with an 's' lens for enhanced sensitivity. The 7700cx ICP-MS was controlled by Agilent Technologies ICP-MS MassHunter 4.3 software (C.01.03) and on a Hewlett-Packard (Hewlett-Packard Palo Alto, CA) desktop computer via a category 5e ethernet cable. ActiveView™ software (New Wave Research, Ltd via Electro Scientific Industries, Inc., Portland, OR) loaded onto a build in desktop computer was used to construct laser ablation experiments and control the triggering of the ICP-MS via a HP 6890 cable connected between the laser ablation system and the ICP-MS. All experiments used 99.9995% ultra-high purity liquid argon (Argon 5.0, Coregas Pty Ltd, Yennora, NSW, Australia). Typical LA-ICP-MS parameters are shown in Table 2.2. To maximize sensitivity and ensure a low oxide formation ($\text{ThO}/\text{Th} < 0.3\%$) with LA-conditions, a NIST 612 Trace Element in Glass CRM was ablated. H_2 was used for collision gas to minimise carbon based polyatomic interferences due to the biological nature of the samples.



Figure 2.2 NWR-193 Laser Ablation System [123] (left) and Agilent 7700 Series Inductively Coupled Plasma Mass Spectrometer [124] (right).

Table 2.2: Typical LA-ICP-MS parameters.

New Wave Excimer 193		Agilent 7700x	
Laser Fluence	0.01, 0.02mJ.cm ⁻²	Sample introduction	
Laser Power	5%	RF power (W)	1350
Spot Size	10,15,20,35 μm	Carrier gas flow rate (L min⁻¹)	1.15
Scan Speed	10-140 μm.s ⁻¹	Makeup gas flow rate (L min⁻¹)	0
Frequency	20 & 40Hz	Sample depth, mm	4
		Ion lenses	
		Extracts 1, 2 (V)	4.5, -125
		Omega bias, lens (V)	-80, 13.2
		Cell entrance, exit (V)	-60, -90
		Octopole parameters	
		Octopole RF (V)	180
		Octopole bias (V)	-18
		Collision gas, flow rate (mL min⁻¹)	H ₂ , 3.1

2.1.3 Microscopy

Leica FS CB microscope with Leica EL6000 fluorescent light source was used for brightfield microscopy and low-resolution fluorescent mapping Figure 2.3. A Nikon A1 laser scanning confocal microscope was used for high resolution and 3-dimensional mapping.



Figure 2.3: Leica FS CB microscope.

Microscopy was performed using a Leica FS CB optical microscope. Objectives of 5x ,10x, 20x and 50x with a 10x eyepiece were used to snake-wise raster capture the regions of interest. Cursory fluorescent images of FITC and stains were taken using a Leica EL6000 fluorescent light source. H3 and A filters were used to isolate FITC and 33342 Hoechst respectively. Images were saved in a Tagged Image File Format (tiff).

2.1.4 Profilometry

Profilometry was used to compare the ablation characteristics of tissue samples, matrix matched standards and gelatin standards. Surface roughness and ablation depth were measured using a DektakXT Profilometer (Bruker, Billerica, MA). A 2 μ m stylus with 1mg of force with an overall scan resolution of 0.33 μ m was used in hill and valley mode. All measurements were performed in triplicate across the full width, height and diagonal of pre- and post- ablation area. Visualisation and statistics were generated using Vision64 (Bruker) software.

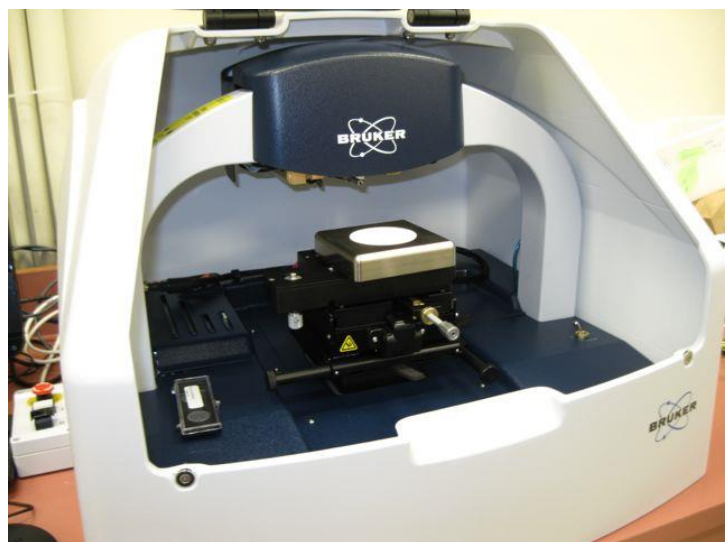


Figure 2.4: DektakXT Profilometer.

Surface topography was measured using a DektakXT Profilometer (Figure 2.4), (Bruker, Billerica, MA). A Dell (Round Rock, TX) desktop computer loaded with Vision64 software (Bruker, Billerica, MA) was used to control profilometry experiments.

2.1.5 Protein quantification via Spectrophotometry

Thermo Scientific™ NanoDrop 2000 Spectrophotometer (Figure 2.5) was used to estimate the concentration of antibodies and aptamers after MaxPar tagging. For antibodies the *A280* mode was used using *IgG* as the reference value due to the type of antibodies used in this work. This means sample concentrations were calculated using the assumed mass extinction coefficient of 13.7 at 280 nm for a 1% IgG solution. Alternatively, for aptamers the *Nucleic Acid* mode was used using *ssDNA-33* as the reference value as all aptamers used were single strand Deoxyribonucleic acid (DNA) [125]. 4μL volumes of sample were aliquoted for all measurements.



Figure 2.5: Thermo Scientific™ NanoDrop 2000 Spectrophotometer.

2.2 Data acquisition and processing

2.2.1 Data acquisition

All standard LA-ICP MS experiments were conducted in line with current best practice [38] using rastered (Figure 2.6) line sampling with scan speeds and ICP-MS dwell times set according to the parameters outlined by Lear *et al.*. Raster lines all began on the same side of the sample with 10 second laser warm up time and a 20 second wash out time between lines. This regime was modified when super-resolution reconstruction (SRR) laser ablation was performed, the details of which will be covered in Chapter 4. In brief, the parameter equation from Lear *et al.* [38] was altered such that the scan speed

multiplied by the integration time was used as the resolution rather than the spot size, with the resolution being an integer proportion of the spot size (i.e. for a 30 μm spot size and resolution of 15 μm the ratio is 2).

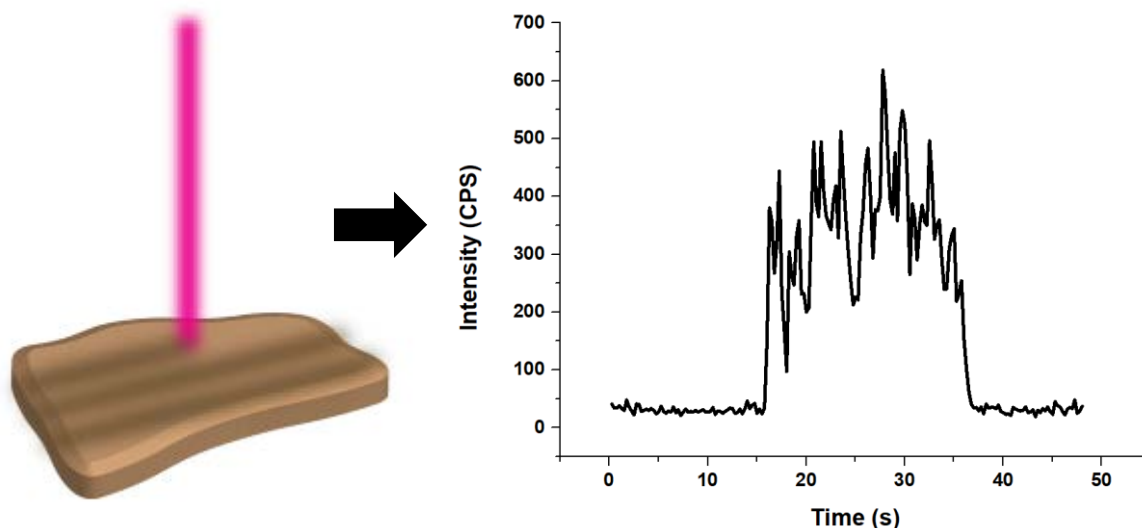


Figure 2.6: Representation of laser ablation raster and the resulting spectra.

The ICP-MS records the data of each raster line in a numbered folder containing a correspondingly numbered comma separate values file (CSV) containing the time resolved elemental data. These numbered folders representing each line of ablation were subfolders of the batch folder.

2.2.1.1 Conversion from raw data to 2D representation

The structure of the CSV in the batch file from a LA-ICP-MS run was in the form of first column time in seconds; then each consecutive column was the signal of one of the measured elements in counts per second (CPS) starting from the lowest mass and ending with the highest mass. This means in order to form images from this data each CSV file must be separated into individual elements and then each element must be merged into a single element image. This was achieved using ImaJar (MassImager Version 3.62b) an in-house developed imaging data processing software package by Robin Schmid, University of Münster. ImaJar converts each batch folder into an image for each isotope recorded and then illustrates them as seen in Figure 2.7.

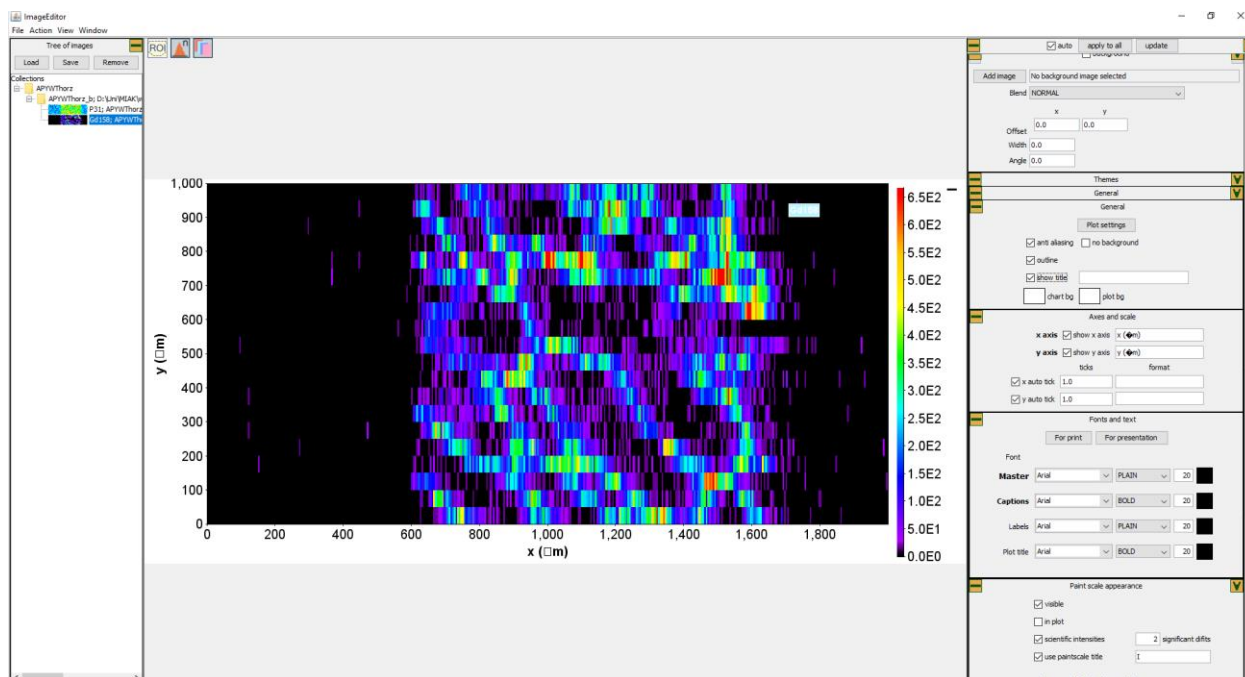


Figure 2.7: Graphic user interface for ImaJar software.

2.2.2 Data visualization and manipulation

After LA-ICP-MS image data was construction in ImaJar, it is exported as either CSV for FIJI or *Visualization Toolkit (VTK)* for Paraview. Once imported both software packages were used to perform several functions required for quantitative imaging. Primarily quantification of the image using the calibration curves constructed from the standards. Image manipulation such as thresholding and filtering were also performed in both software. Image statistics such as histograms and calculation of the mean, median and mode were also completed using both software.

2.3 Experimental Methods

2.3.1 Chemicals and Reagents

Argon and hydrogen used in all experiments were supplied as 99.99% pure liquid (Ace Cryogenics; Castle Hill NSW, Australia). All ‘water’ referred to in experiments was 18.2 $M\Omega\text{ cm}^{-1}$ deionised water. High purity metal salts were purchased from Sigma-Aldrich (Castle Hill NSW, Australia). Liquid elemental standards, ultrapure hydrogen peroxide and ultrapure nitric acid (Seastar Baseline 67– 70% HNO_3 ; Choice Analytical, Thornleigh

NSW, Australia) unless otherwise stated. All tissue samples and homogenates were stored at -18 °C. Disposable plastic ware was sterile, and all pipette tips were trace metal free polypropylene with a high-density polyethylene filter (Gilson, WI, USA, Australia) to prevent aerosols and cross-contamination.

2.3.2 Matrix Matched Mouse Brain Standards

Tissue standards were prepared using a modification of the method described by Hare *et al* [52]. Mouse brains were harvested from control animals euthanised under existing ethics protocols with tissue sharing approvals at UTS. Tissues were washed in three changes of phosphate buffered saline pH 7.4 (PBS; NaCl 8g/L; KCl 0.2g/L; Na₂HPO₄ 1.15g/L; KH₂PO₄ 0.2g/L). and connective tissue, blood vessels, and fat were carefully dissected away. The tissue was then homogenised using a variable speed tissue homogeniser (Omni Scientific, Vista CA, USA) fitted with disposable polypropylene tips which were cleaned of trace metal contamination by soaking in 5% nitric acid for 24 hours and rinsed in several changes of deionised water. Homogenisation was conducted in short bursts and the tissue cooled on ice to minimise heat generation during the process.

Metal standard solutions were prepared as follows. Stock solutions of given metals were made from analytical grade (99.9999% purity) nitrate salts and Milli-Q (MQ) water (18.2 MΩ·cm at 25°C, Arium Pro Vf, Sartorius, Goettingen, Germany) to 100ppm concentration. An aliquot (500µL) of each standard solution was individually spiked into 0.5g of homogenized mouse brain and mixed by additional homogenisation. An additional 4.5g of homogenized mouse brain was added further mixed; care was taken to prevent local heating of the tissue. The samples were centrifuged for five minutes at 1000 rpm in a bench top centrifuge to remove incorporated air bubbles. The resulting homogenates were transferred to disposable moulds and cryosectioned at 30µm using disposable Teflon coated microtome blades (CL Sturkey Inc., Lebanon PA, USA) and air dried.

2.3.2.1 Quantification of Metal Concentrations in Standards

The concentrations of metal standards in the gelatin standards and tissue homogenates were confirmed by microwave digestion and analysis of the digests by solution ICP-MS

(SN-ICP-MS). Aliquots of homogenised tissue standard (three replicates; approximately 50 mg each) were microwave digested in a MARS 6 - Microwave Digestion System (CEM Corporation, Matthews, NC) using the “Animal Tissue” method in 5mL of a 4:1 solution of HNO₃ (68% w/v) and H₂O₂ (30%w/v; Choice Analytical). Gelatin standards were digested by the addition of 1mL of HNO₃ (68% w/v) then topped up to 5mL with MilliQ water. After digestion, each solution was quantitatively transferred to a sterile disposable centrifuge tube (15 mL; Falcon™, Becton Dickinson, Franklin Lakes NJ, USA), diluted with water and the weight recorded (approximately 50g/tube). The diluted solutions were then analysed by solution-ICP-MS (Agilent Technologies 7500cx, Santa Clara, CA, USA).

2.4 Calculations

2.4.1 Linear regression analysis

Table 2.3: Table of formulas used in the excel function LINEST.

Function	Excel Syntax	Equation
Average	AVERAGE(number1, [number2], ...)	$\bar{a} = \frac{1}{n} \sum_{i=1}^n a_i$
Standard Deviation	STDEV(number1,[number2],...)	$s = \sqrt{\frac{\sum(x - \bar{x})^2}{(n - 1)}}$
Slope	SLOPE(known_y's, known_x's)	$m = \frac{\sum(x - \bar{x})(y - \bar{y})}{\sum(x - \bar{x})^2}$
Intercept	INTERCEPT(known_y's, known_x's)	$b = \bar{y} - m\bar{x}$
Linearity	RSQ(known_y's,known_x's)	$r^2 = \frac{\sum(x - \bar{x})(y - \bar{y})}{\sqrt{\sum(x - \bar{x})^2 \sum(y - \bar{y})^2}}$

Error in slope	LINEST(known_y's,known_x's,TRUE,TRUE)	$s_m = \sqrt{\frac{1}{n-2} \frac{\Sigma(y - \hat{y})^2}{\Sigma(x - \bar{x})^2}}$
Error in intercept	LINEST(known_y's,known_x's,TRUE,TRUE)	$s_b = \sqrt{\frac{\Sigma(y - \hat{y})^2 \Sigma x^2}{n(n-2) \Sigma(x - \bar{x})^2}}$

2.4.2 Limits of analysis and outliers

Table 2.4: General equations used for statistical analysis.

Function	Equation
Limit of detection	$LOD = \frac{(\bar{y}_0 + 3.3s_0) - b}{m}$
Limit of quantification	$LOQ = \frac{(\bar{y}_0 + 10s_0) - b}{m}$
Grubb's test for outliers[126]	$G = \frac{ x_i - \bar{x} }{s}$

2.5 Animals

Mouse brain sections were acquired from the Howard Florey Institute of Neuroscience and Mental Health, University of Melbourne. Under the following Howard Florey Animal Ethics Committee approval 15-104-FINMH. Briefly, male C57BL/6 mice were raised according to standard animal care protocols and fed normal chow and water ad libitum. Animals were euthanised with an overdose of sodium pentobarbitone (100 mg kg⁻¹) and perfused with 30 mL of warmed (37 °C) 0.1 M phosphate buffered saline (PBS), pH 7.4. Tissue was briefly fixed in 4% paraformaldehyde in PBS until the brains sank, after which they were immersed overnight in two changes of 30% sucrose in PBS. Tissue was then frozen at -80 °C and mounted in O.C.T.[™] via the medulla oblongata and upper spinal cord. After equilibrating at -20 °C, the brains were sectioned using PTFE-coated cryotome blades (DT315R50 Silver Microtome Blades. C. L. Sturkey, Inc., Lebanon PA)

on a Cryostar cryotome (CryoStar™, Thermo Fisher Scientific, North Ryde, NSW, Australia) to 30 µm thickness at 90 µm intervals and mounted on standard microscope slides

Wild-type (C57BL/6J), mdx (C57Bl/10ScSn-Dmd^{mdx}/J background), and heterozygote mouse (WT/mdx bred inhouse) quadriceps tissues were purchased from Jackson Laboratories (Bar Harbor, ME, USA,) and rectis femoris muscle was dissected under guidelines established by the Institutional Animal Care and Use Committee at the University of California, Los Angeles. Mice were maintained in the Terasaki Life Sciences Vivarium following guidelines established by the Institutional Animal Care and Use Committee at the University of California, Los Angeles (approval #2000-029-43) and approval for these studies was granted by the UCLA Animal Welfare Assurance (approval #A3196-01). All mice used in the study were male. Animals were euthanised by CO₂ with cervical dislocation and Quadriceps were dissected and harvested immediately. Tissue was then frozen at -80 °C and mounted in O.C.T.™ via the Quadricep. After equilibrating at -20 °C, the quadriceps were sectioned using PTFE-coated cryotome blades to 10-50µm thickness and mounted on standard microscope slides.

2.5.1 Immunohistochemistry

All IHC experiments were performed in labs sterilized with RNase AWAY™ (Thermo Fisher Scientific, North Ryde, NSW, Australia). All buffers were diluted with water sterilized via 0.22µm filtering and then autoclaving unless otherwise stated. LoBind microcentrifuge tubes (Eppendorf Macquarie Park NSW, Australia) were used to store antibodies, aptamers and staining solutions. All disposable accessories (e.g. pipette tips and centrifuge tubes) were either bought sterile or sterilized by autoclave.

3 Standard Preparation and Comparison

3.1 Abstract

The quantification of elemental distributions in biological tissue requires laboratory prepared matrix-matched standards. Inherent variabilities in standard matrices and sample composition require careful evaluation of accuracy, precision and robustness. Standard matrices need to be as closely matched to the sample in both physical and biochemical properties, and preparation of standards with various biological matrices may not be suitable for the intended analysis. Furthermore, complex and time-consuming preparation methods limit their applicability. This chapter presents novel facile methods for the preparation of gelatin standards using both commercial and laboratory-made moulds. Surface roughness, height and robustness of the mould-prepared standards were compared against cryo-sectioned gelatin and homogenised brain tissue standards. The mould-prepared standards had significantly higher accuracy and precision, were easier to prepare, and provided enhanced reproducibility. We also present a simple method to remove background metals in gelatin using chelating resins to increase the dynamic calibration range and to improve limits of analysis.

3.2 Introduction

Laser ablation-inductively coupled plasma-mass spectrometry (LA-ICP-MS) was first applied to biological tissues in 1994 by Wang *et al.* [127] and is now a routine technique to measure the spatial distribution of elements and co-factors of functional biomolecules. Recent advances in immunohistochemistry have also expanded the applicability of LA-ICP-MS to the investigation and quantification of biomolecule distributions [128,129]. Progress in sampling techniques [130] and internal standardisation approaches [131,132] to overcome instrumental drifts has also contributed to improved precision and accuracy and rapid analyses [133]. One major advantage of LA-ICP-MS over other bio-imaging methods is the capability of calibration for quantification of the target element or biomolecule. For typical analytical methods sequential analysis of reference standards and samples is the gold standard for validated quantification. Unfortunately, the diversity and individuality of biological tissues preclude the use of certified reference

materials or standards, and laboratories are usually required to prepare and characterise their own “in-house” prepared reference standards [52,134,135]. Most approaches aim to simulate the biological environment of metals and heteroatoms to guarantee consistent ablation characteristics, aerosol formation, transport, atomisation and ionisation[136]. However, the simulation of these matrix-matched tissue standards is limited as standard matrices cannot fully mimic the full spectrum of biological tissue in terms of heterogeneity, durability and biochemical environment. This has motivated many researchers to investigate a variety of approaches to harmonize the methods of standard preparation to meet regularity guidelines.

One common approach to prepare reference standards includes the homogenisation of easily obtainable tissues from lamb, pig, cow or mouse which aims to match the target tissue as closely as possible. The homogenate is then spiked with aliquots of metals, again homogenised, frozen and subsequently sectioned to their desired thickness. A cross-quantification step consisting of digestion of the standard and analysis by solution nebulisation ICP-MS is required to determine accurate elemental levels in standards [52]. A variety of approaches have been published reporting the preparation of materials to simulate tissue obtained from brain [66,137] eye[138,139] tumour tissue [129,140] liver [141,142] and teeth [134,143].

Unfortunately, high levels of endogenous elements in the chosen matrix of the standard limit the ability to determine lower elemental concentrations. Trace elements that are downregulated by a biological response are often outside the calibration range when calibrated against reference tissues exhibiting a natural abundance of elements. Further issues are related to the homogenisation and cutting process, which vary in reproducibility and potentially introduce a systematic error and uncertainty between different batches of standards. Standards originating from different tissues and/or different animals show different characteristics which can be traced back to differences in individual elemental and biomolecule levels influenced by genetics, environment and type of tissue. The tedious preparation and characterisation, and the susceptibility towards systematic error has encouraged the investigations of other standard materials which are easier to manufacture and show less variability. Specifically, the operation of

micro and cryotomes can induce deformation and dimensional changes in height as discussed by Dorph-Petersen *et al.* [144].

Hydrocolloid gel standards such as gelatin based standards are becoming increasingly frequent for the calibration of metals in biological tissues as they show similar densities and similarities in composition and mitigate the problems with homogenates from raw animal tissues [121,136,145,146]. Three major methods for the fabrication of gelatin standards are described in literature comprising pipetted films [147], spotted droplets [145] and cryo-sections [148]. However, surface tensions, “coffee-stain” effects, elemental discrimination and cutting artefacts may affect the homogeneity of elemental distribution and standard topography, which needs to be controlled carefully to sustain stable quantification [145].

Furthermore, as with raw animal tissue, gelatin has natural background levels for biologically important metals, which complicates the determination of trace metals. The properties of gelatin standards can be controlled quite precisely by several parameters. Sala *et al.* [145] discussed the effect of various drying/setting and gelatin content in the context of coffee-stain effects and elemental discrimination. They analysed depth and surface distributions at various lateral resolutions and found that careful control allows the fabrication of highly homogenous, microanalytical standards suited for the calibration of elements in soft biological tissue.

Complete ablation of the entire sample requires the standard to have the same height as the sample and is usually accomplished by cutting with a microtome or cryotome. However, even if these instruments are calibrated regularly, they are a potential source for lower accuracy and precision. Another approach is to avoid complete ablation of sample and standard in order leave some remaining tissue on the microscope slide. If matrix matching was successful, continuous amounts of material should be ablated from both sample and standards.

In this work, we present novel facile methods for the preparation of gelatin standards for improved traceable standards compared to cryo-cut gelatin, and homogenates from raw animal tissue. We demonstrate that commercial and laboratory-made moulds offer

improved, simplified and reliable control of standard dimensions and surface. The elemental and surface homogeneity and height were compared to different animal tissues and cryo-sectioned gelatin, as well as robustness and reproducibility of calibration. This chapter explores the effect of endogenous element concentrations on the analytical figures of merit and present an extraction method to avoid high elemental background intensities to improve current limits of analysis.

3.3 Method

3.3.1 Gelatin Standards

Direct comparison between gelatin and mouse brain homogenate standards were performed for manganese, copper and zinc due to their natural biological occurrence and diagnostic importance [149,150].

Unless otherwise listed chemicals were attained from Sigma Aldrich, Castle Hill NSW, Australia at the highest possible purity. A single stock solution containing the metal salts at the concentrations listed in Table 3.1 was prepared in a buffer containing 100mM Tris-HCl to buffer the acidic metal salts (pH7.4 Sigma Aldrich, Castle Hill NSW, Australia), ethylenediaminetetraacetic acid to complex the metals so precipitation does not occur at high concentration (EDTA; 10 mM Sigma Aldrich, Castle Hill NSW, Australia), 1% w/w polyethylene glycol to strengthen the gelatin as previously reported [151] (M_n 400 Sigma Aldrich, Castle Hill NSW, Australia) prepared in Milli-Q (MQ) water (18.2 $M\Omega\cdot\text{cm}$ at 25°C, Arium Pro Vf, Sartorius, Goettingen, Germany). For each of the resulting metal salt solutions, a 900 μL aliquot was added to 100 mg gelatin from bovine skin (Type B, Sigma Aldrich, Castle Hill NSW, Australia) and dissolved by heating to 53°C for 15 minutes on a dry block with periodic vortexing.

Table 3.1: Metal salts used in Gel Standards.

Element	Salt	Concentration in stock solution ($\mu\text{g}\cdot\text{mL}^{-1}$)
Cu	Copper (II) nitrate hydrate	100
Mn	Manganese (II) nitrate hydrate	100
Zn	Zinc nitrate hydrate	100

Three different moulds were tested for the manufacturing of gelatin standards on a microscope slide: BRAND® cavity slides (76 mm × 26 mm, thickness 1.2-1.5 mm 3 concavity, Sigma Aldrich, Castle Hill NSW, Australia), CultureWell™ Reusable Gasket (8 wells 6mm Diameter X 1mm Depth volume 15-30 μL ; Grace Bio-Labs, Bend,OR) and 6-well Hybriwell™ gasket (depth 0.25 mm, volume 50 μL ; Grace Bio-Labs, Bend,OR) as seen in Figure 3.1.

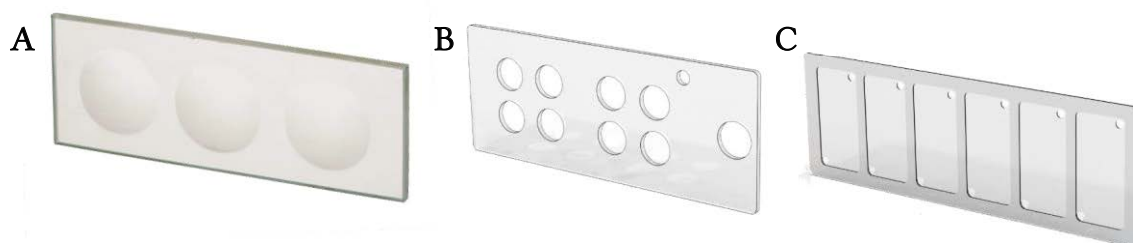


Figure 3.1: Moulding devices for gelatin standards: Cavity slide (A), Culturewell™ (B) and Hybriwell™ (C).

Gelatin standards were deposited onto each of the wells of the cavity slide (Figure 3.1 A) using a piston pipette (20-100 μL PIPETMAN Classic, Gilson, Middleton, WI). 100 μL of still liquid gelatin standard was carefully applied to minimise the creation of bubbles. After pipetting slides were left at room temperature to solidify.

A Culturewell™ gasket (Figure 3.1 B) was fixed onto a single plain slide. Gelatin standards were pipetted into the wells at a volume of 50 μL then left to solidify at room temperature.

A 6 Hybriwell™ gasket (Figure 3.1 C) clear polycarbonate cover with two ports (depth 0.25 mm, volume 50 µL; Grace Bio-Labs, Bend,OR) was applied to a fresh single plain glass microscope slide. The chamber slides were heated to 53°C for one minute on a dry heat block before filling a total volume of 50 µL metal-gelatin standard via the port using a piston pipette.

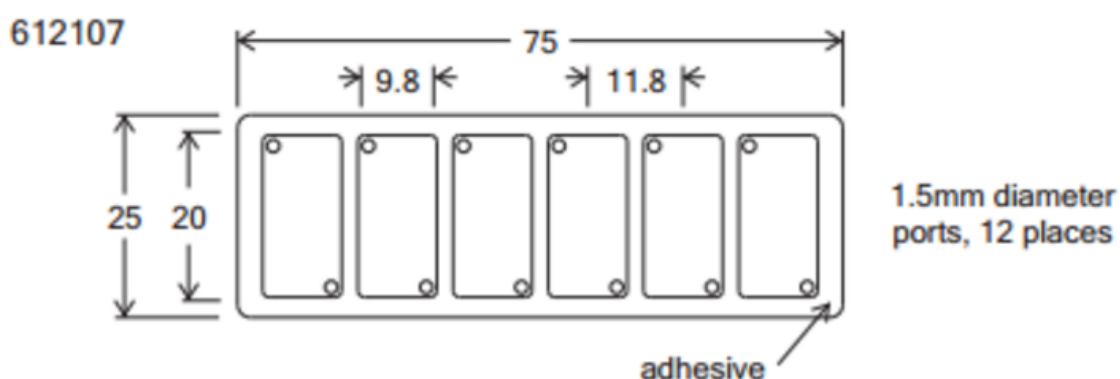


Figure 3.2: 6-well Hybriwell™ gasket schematic [152].

Prior to removal of the adhesive gasket and seal, the gelatin standards were cooled to room temperature (30 minutes) and subsequently to -20°C (20 minutes) until the gelatin film was frozen and opaque in appearance. Liquid nitrogen freezing was not used due to the risk of petrification [153]. The standards were then stored at room temperature until required for use.

For further characterisation, 50 mg aliquots of gelatin were digested with 50 µL of nitric acid (67-70% Seastar Baseline, Sidney, BC, Canada) overnight then diluted to 4mL with MQ water.

Various gelatin standards thicknesses were produced with laboratory prepared moulds by using Teflon tape (Bush branded) (100 µm) as a spacer between a PTFE block and a glass microscope slide. The resulting gaps were filled with heated liquid gelatin and subsequently frozen and dried as per the commercial moulds. Multiple layers of the 100 µm Teflon tape were used to manufacture gelatin standards with thicknesses of any multiple of 10 µm.

3.3.2 Tissue Standards

Tissue standards containing copper, manganese and zinc were prepared as previously described by Hare *et al.* [52] using mouse brains harvested from control animals euthanised under existing ethics protocols with tissue sharing approvals at UTS. Briefly, mouse brains were homogenised, and weighed aliquots were spiked with metal solutions to give final metal concentrations as shown in Table 3.2. The spiked homogenate was then injected into moulds and frozen at -20°C. The frozen homogenate was cryo-sectioned using PTFE-coated cryotome blades (DT315R50 Silver Microtome Blades. C. L. Sturkey, Inc., Lebanon PA) on a Cryostar cryotome (CryoStar™, Thermo Fisher Scientific, North Ryde, NSW, Australia) and mounted on microscope glass slides (Superfrost™, Thermo Fisher Scientific, North Ryde, NSW, Australia).

3.3.3 SN-ICP-MS

SN-ICP-MS was performed as outlined in section 2.1.1. Standards for the counter quantification of copper, manganese and zinc standards were made from 10 ppm single element standards (Choice Analytical NSW, Australia) diluted in 1% HNO₃ at 5, 1, 0.5, 0.25, 0.1 and 0.05 ppm. Gelatin and brain standards were diluted 1:10 for analysis using 500µL of 67-70% nitric acid (SEASTAR™ BASELINE®, Choice Analytical Thornleigh NSW, Australia) and made to volume with MQ.

Table 3.2: Concentrations of external calibration standards.

	Name	Cu (mg/kg)	Mn (mg/kg)	Zn (mg/kg)
Gel	Blank	0.00	0.28	0.03
	1	3.15	2.32	1.92
	2	5.00	4.30	3.97
	3	9.04	7.50	6.69
	4	18.62	15.27	13.85
	5	48.85	39.39	29.33
Brain	Blank	5.42	0.03	2.29
	1	5.49	0.53	4.17
	2	15.93	10.00	18.09
	3	38.03	29.07	33.79
	4	51.87	44.48	64.54

3.3.4 Elemental extraction to decrease background levels

Trace or minor elements were removed from the gelatin via solid-liquid extraction of with non-buffered water to avoid buffer components interfering with extraction. 200 mg of gelatin was weighed and dissolved in 800 μ L of water, heated to 53 $^{\circ}$ C, and spiked with chelating resins. Various resins were investigated: Amberlyst 15 (H), Amberlite CG50 (H) and Amberlite IR120 (Na⁺) were purchased from Sigma Aldrich while Bio-Rex 70 and Chelex 100 were purchased from Bio-Rad (Gladesville, Australia). Resins were added to liquid gelatin standards and gently shaken for 1 hour before being separated by centrifugation in a Centrifuge 5702 (Eppendorf; Macquaire Park, Australia) operated at 2000 rpm for 2 minutes. The supernatant was diluted with a 2x concentrated buffer solution to produce a 10% buffered gelatin standard, which was then applied to the mould.

3.3.5 LA-ICP-MS

LA-ICP-MS parameters were set to those outlined by Lear *et al* [38] to obtain squared pixels. Four adjacent lines 4 mm in length were ablated from each standard using spot

sizes of 20, 35, 50, 100 μm using a NWR193 Laser Ablation System (Kenelec Scientific, Frenchs Forest, Australia) coupled to a 7700 ICP-MS (Agilent Technologies, Mulgrave, Australia) at 40 Hz with a laser fluence of 0.5 J/cm². The four adjacent lines were re-ablated an additional 3 times to form 4 layers of ablation to test depth homogeneity in gelatin standards. LA-ICP-MS conditions were optimised using NIST 612 trace elements in glass certified reference material (National Institute of Standards and Technology, Gaithersburg, USA). To maximize sensitivity and ensure a low oxide formation (ThO/Th<0.3%) with LA-conditions, a NIST 612 Trace Element in Glass CRM was ablated

3.3.6 Data Analysis

All Data analysis was performed with Microsoft Excel (Microsoft Corporation, Redmond, WA). Limits of analysis were determined from measurement of signal response and standard deviation from the gelatin /tissue blank[154]. Limits of detection (LOD) and quantification (LOQ) were calculated using the equations found in Table 2.4. A confidence value (k) of 3.3 for LOD and 10 for LOQ was used. σ_b standard deviation of the blank, respectively, and m is the slope of the curve. Standard deviation calculations of all samples and standards was also performed using the inbuilt STDEV.P function.

3.3.7 Profilometry

Surface roughness of the gelatin standards was measured using a DektakXT Profilometer (Bruker, Billerica, MA). A 2 μm stylus with 1mg of force with an overall scan resolution of 0.33 μm was used to scan the full length and width of gelatin standards, mouse brain standards, mouse lung section and mouse quadricep section for a total of 3 times each.

Surface roughness was calculated using the Root Mean Squared Roughness (R_{RMS}) equation shown below.

$$R_{RMS} = \sqrt{\frac{\sum x^2}{L}}$$

$\sum x^2$ is the sum of the squared displacement and L is the length of measurement. Surface roughness is then normalised by the subtraction of the mean height of the standard.

3.4 Results and Discussion

3.4.1 Qualitative comparison of mould methods

The three different gelatin moulding methods were compared visually to assess viability for further analysis of the standards. This initial test compared surface topology, stability and LA-ICP-MS compatibility. Cryotomed tissue sections were used as a benchmark for comparison as physical similarity is a minimum gauge of fitness for usage.

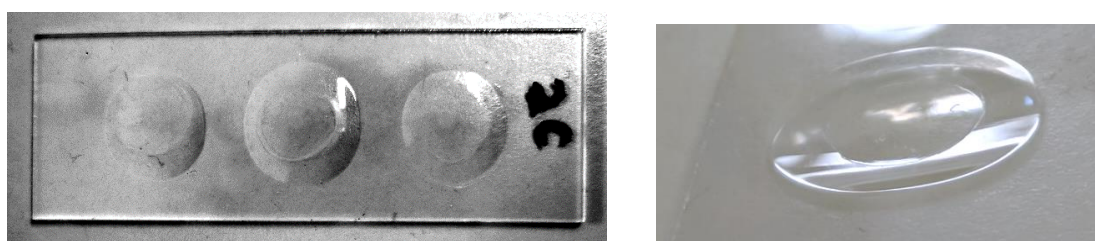


Figure 3.3: Cavity slide gelatin standards. Plan view and single concavity aspect.

The cavity slide, while easy to apply gelatin standards, produced a curved surface to each as seen in Figure 3.3. This topology may cause artefacts during laser ablation and would require constant refocussing. The limitation of having only three wells per slide at minimum would require two slides of standards reducing the available area for samples within a sample cell.



Figure 3.4: Culturewell™ silicon gasket gelatin standards. Plan view and aspect of 4 wells.

The Culturewell™ gaskets (Figure 3.4) were flatter in profile than the cavity slides but had other issues. Due to the formation of a meniscus during pipetting the edges of the circles of gelatin were highly curved reducing the usable surface. Given the smaller

dimensions of each well this would reduce the reusability of this standard. Each gelatin circle was also prone to coming unstuck from the microscope slide from general handling which could lead to damage or loss of standards.

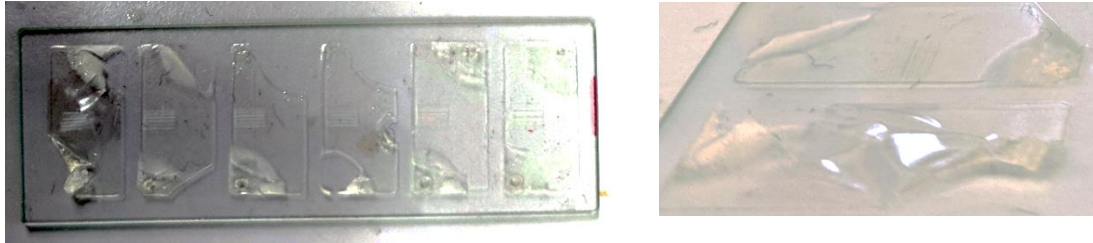


Figure 3.5: Hybriwell™ slide gelatin standards left in the freezer too long. Plan view and aspect of 2 wells.

The preparation of gelatin standards utilising Hybriwells appeared to be most promising as curved surfaces and artefacts were easier avoided (Figure 3.6). The rectangular shape also makes it more compatible for efficient line by line ablation compared to the circular shape of the previous moulds. The large 196mm² area of each standard is also appealing with only the areas beneath each injection port being unusable.



Figure 3.6: Hybriwell™ slide gelatin standards. Plan view and aspect of 2 wells.

However, the freezing process must be carefully controlled. This step can affect the quality of a standard as seen in Figure 3.5, where the areas near the injection ports lifted due to leaving the slide in the freezer for too long. Nevertheless, the surface was visually flat and free of damaged areas across most of each standard.

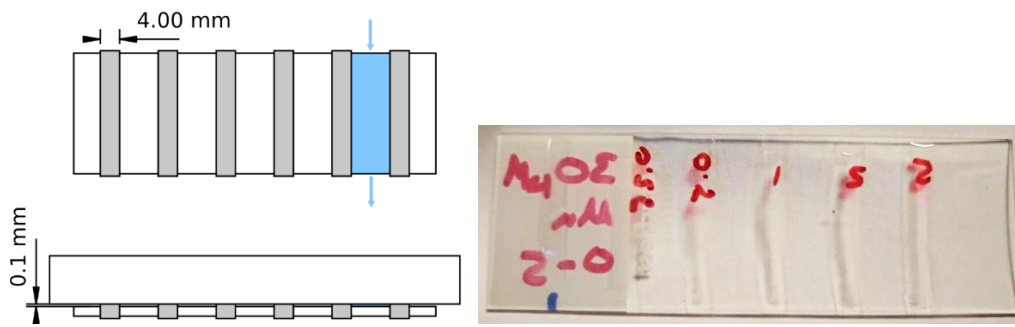


Figure 3.7 Teflon tape manufactured schematic and as fabricated gelatine standards

The standards manufactured by Teflon tape (Figure 3.7) were equivalent to the ones made by Hybriwell™ gaskets as they both use capillary action to fill the moulds thereby minimising drying related artefacts. Teflon tape standards also had regions without gelatin as with the injection ports of the Hybriwell™ gaskets. In the case of the Teflon mould-standards this happened on the ends of the slide where Teflon tape was not present (i.e. the entry and exit of the well). Removal of Teflon tape had to be undertaken with care as any wrapping imperfections created areas where the gelatin would embed itself in the tape making removal a tearing risk for the gelatin standard.

3.4.2 Topography and height characterisation

The three cryo-sectioned tissue matrices brain, quadriceps, and lung; and cryo-sectioned and mould filled gelatin were fabricated, and the topography measured by profilometry as shown in Figure 3.8 and Table 3.3.

Cryo-sectioning caused significant systematic error in height, despite regular calibration of the cryostat. The error was most prominent for tissue samples with deviations from the expected values ranging from 49.0% to 126.4% for lung and quadriceps tissue, respectively. High shear forces during sectioning, induced thickness artefacts and increased surface roughness at the margins of the sections. The cryo-sectioning of a homogenised brain standard and a gelatin standard resulted in a thickness of 67.3% and 73.9% of the expected value with a standard deviation of $\pm 3.52 \mu\text{m}$ and $\pm 0.99 \mu\text{m}$, respectively. The preparation of biological material (e.g., fixing, drying, shear forces during cutting) induced various types of deformations (homogeneous or differential, isotropic or anisotropic, uniform or non-uniform) as discussed by Dorph-Peterson *et al.* [144].

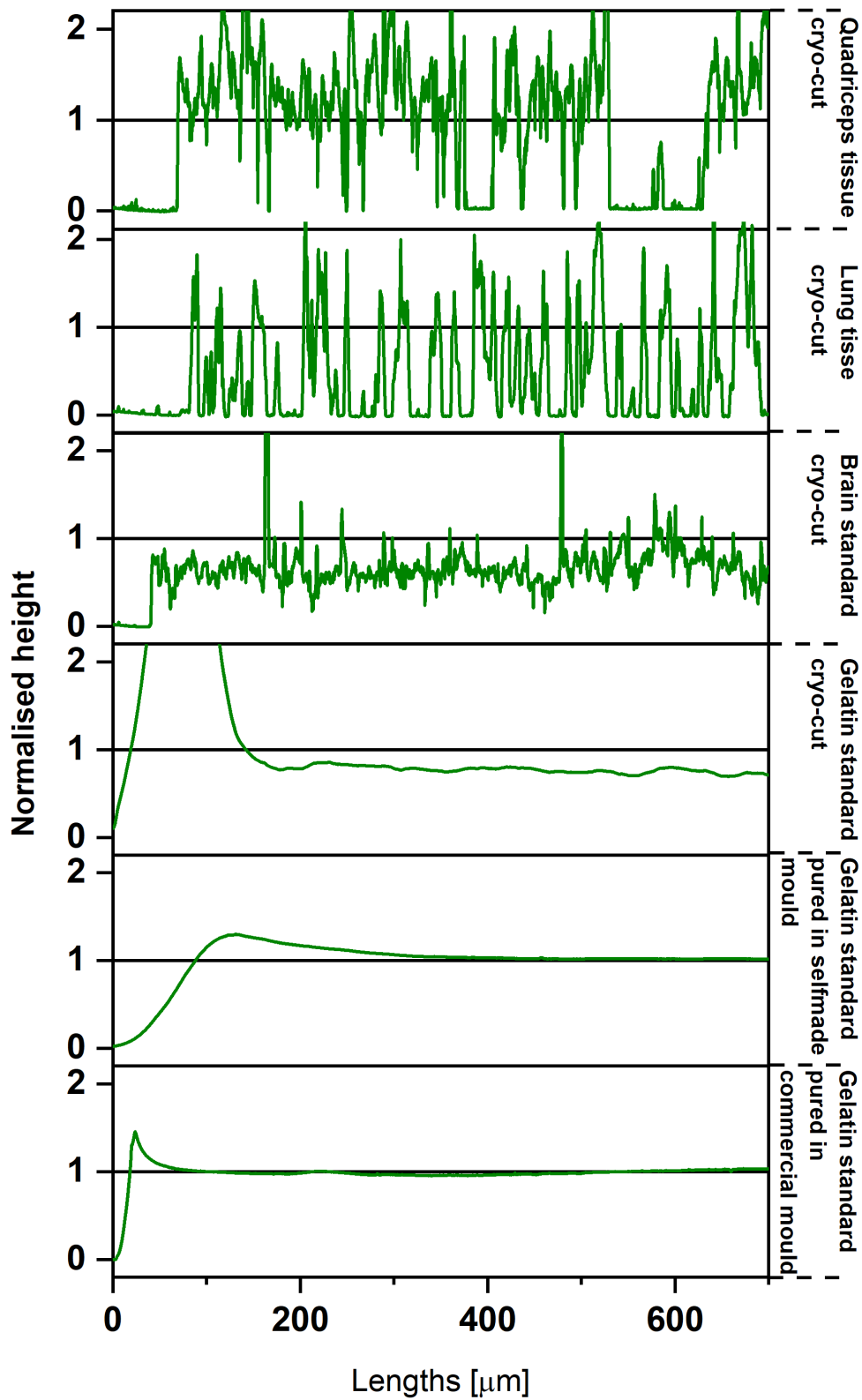


Figure 3.8: Normalised heights as determined by profilometry showing deviations in height and heterogeneity in surface topography. The measured height of the tissues/standards was normalised to the expected height.

Table 3.3: Comparison of accuracy derived from different preparation methods and materials.

Standard type	Theoretical thickness [μm]	Observed thickness [μm]	Accuracy [%]	Standard deviation [μm]
Quadriceps	10.00	12.64	126.4	6.68
Lung sample	5.00	2.59	49.0	2.82
Brain standard	10.00	6.73	67.3	3.52
10 μm Gelatin	10.00	7.39	73.9	0.99
10 μm Gelatin	10.00	10.26	102.6	0.80
25 μm Gelatin	25.00	24.90	99.0	0.59
30 μm Gelatin	30.00	28.34	94.5	1.64

Gelatin standards manufactured in moulds exhibited an increased height accuracy ranging from 94.5% to 102.6% with typical standard deviation between 0.59 and 1.64 μm . Only the margins of mould prepared standards appeared to contain thickness artefacts, typically seen as an increase height, and likely due to drying processes, similar the coffee-stain effect [145], but far less prominent. The profilometry comparison of sectioned gelatin and mould-prepared gelatin demonstrated an increased control of height and surface roughness for standards prepared in both commercial and laboratory-made moulds. When performing complete ablation of a sample, inaccuracy in height translated directly into a systematic error in quantification. Therefore, gelatin standards prepared in moulds are more suited for stable quantification. The differences in height and roughness of various tissues and standards after cryo-sectioning require a detailed topographical characterisation prior and/or after analysis via LA-ICP-MS.

3.4.3 Post-analysis characterisation

Figure 3.9 shows a photomicrograph image of (A) ablated lines on a homogenised brain standard and (B) on a mould-prepared gelatin standard. Tissue homogenisation produced micro-structures with physical properties that caused entire ablation of the standard in some areas, while tissue remained in other areas (Figure 3.9 (A)).

These micro-structure heterogeneities increased the overall error, in particular during high spatial resolution analysis. Micro-structures were not observed in the gelatin standards and ablation produced reproducible patterns (Figure 3.9 (B)) with a consistent depth.

Figure 3.9 (C) shows the topography of both homogenised brain standard and mould-prepared gelatin standards with thicknesses of 10 μm following with 11 adjacent laser scan lines and increasing laser power ranging from 0.02 J cm^{-2} to 3.52 J cm^{-2} . The ablation of adjacent lines on the homogenised brain standard resulted in crater formation impacting adjacent scan lines. This uncontrolled removal of surrounding tissue became more prominent with increasing laser power and resulted in uncontrolled mass flows of ablated elements and decreased spatial resolution. These effects were not observed on gelatin standards which improved aerosol formation and increased quantification stability. The improvement of increased control of material introduced into the plasma and overall robustness was demonstrated by four adjacent scan lines on all standards with Figure 3.9 (D) demonstrating the highest standard. The signals of Mn, Cu and Zn as typical biological relevant elements were monitored and normalised to the average response. The sequential ablation of gelatin layers resulted in only minor sensitivity drifts. The sequential ablation of layers on homogenised brain standards, however, resulted in significant drift; a direct consequence of poorly controlled aerosol formation and heterogeneity in surface topography.

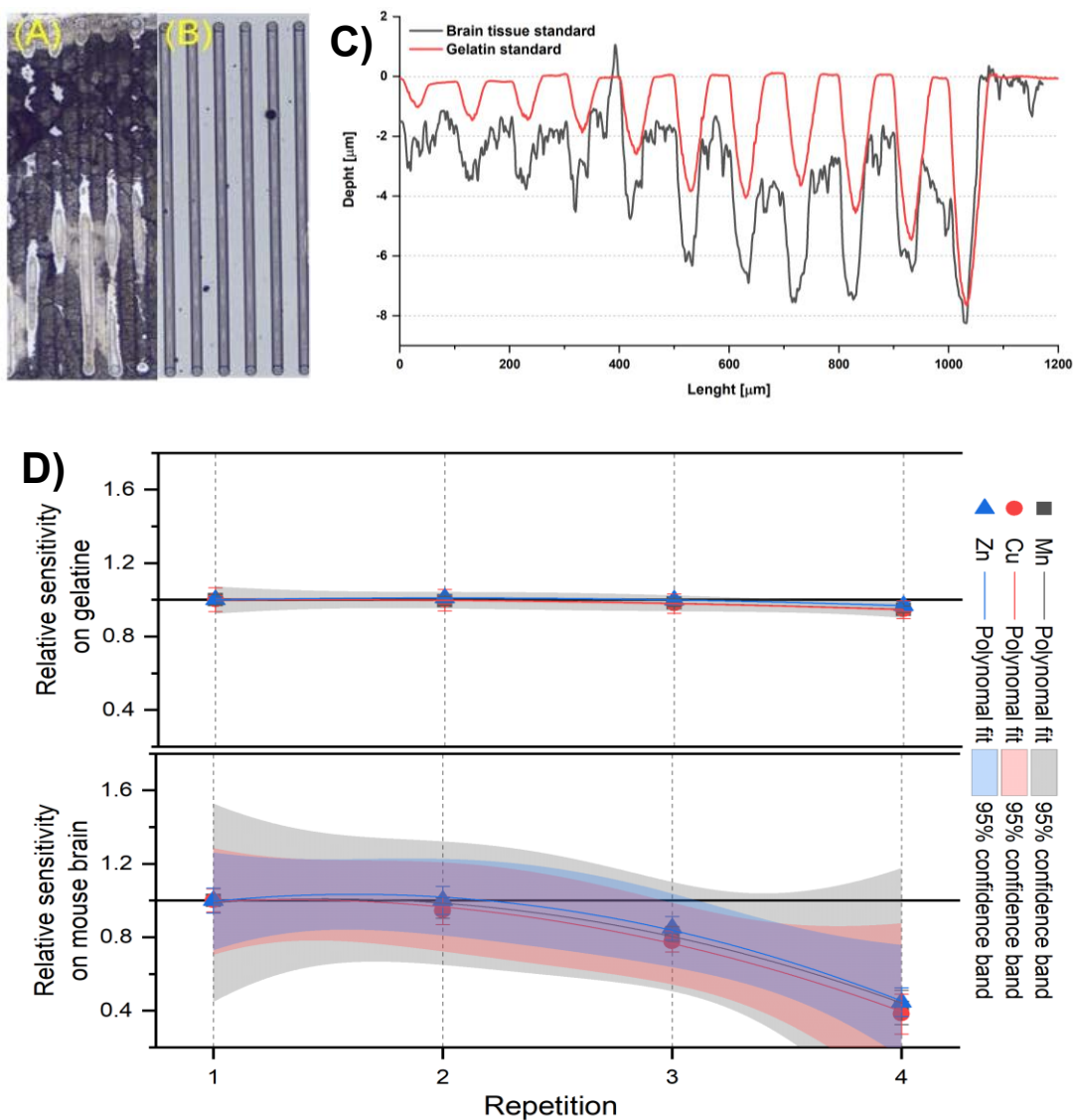


Figure 3.9: Visual comparison of an ablated homogenised animal tissue standard (A) and a gelatin standard (B). (C): Profilometry data standards ablated eleven times with increasing laser power. (D): Signal intensities for Mn, Cu, and Zn derived from repeated ablation of standard material.

3.4.4 Analytical figures of merit and background equivalent concentrations

The analytical figures of merit were compared between calibrations of gelatin standards and homogenised brain standards. The concentration of the biologically relevant elements Mn, Cu and Zn were determined by solution nebulisation ICP-MS and are shown in Table 3.4, as well as the LOD, linearity and sensitivity from the calibration curves following LA-ICP-MS analysis. The LODs for the gelatin standards were 10-times lower for Zn, 3.8-times lower for Mn and only slightly reduced for Cu.

Table 3.4: Characterisation of standard materials. The concentrations and error of each calibration level were cross-quantified by solution-based ICP-MS. LOD, Sensitivity and Linearity were determined from the calibration curve constructed by LA-ICP-MS.

	Mn	Cu	Zn	
Gelatin standards	Blank [$\mu\text{g/g}$]	2.20 \pm 0.70	0.52 \pm 0.21	0.03 \pm 1.06
	Level 1 [$\mu\text{g/g}$]	2.32 \pm 0.88	3.15 \pm 0.50	1.92 \pm 1.01
	Level 2 [$\mu\text{g/g}$]	4.30 \pm 1.11	5.00 \pm 0.87	3.97 \pm 1.14
	Level 3 [$\mu\text{g/g}$]	7.50 \pm 1.51	9.04 \pm 1.58	6.69 \pm 1.39
	Level 4 [$\mu\text{g/g}$]	15.27 \pm 2.33	18.62 \pm 2.72	13.85 \pm 1.96
	Level 5 [$\mu\text{g/g}$]	39.39 \pm 2.69	48.85 \pm 2.84	29.33 \pm 2.21
	LOD [$\mu\text{g/g}$]	1.10	4.28	0.64
	Linearity (R^2)	0.9983	0.9916	0.9995
	Sensitivity [cps \cdot g/ μg]	1390 \pm 50	143 \pm 5	175 \pm 4
Mouse brain standards	Blank	0.03 \pm 0.80	5.42 \pm 1.81	2.29 \pm 7.49
	Level 1 [$\mu\text{g/g}$]	0.53 \pm 1.00	5.49 \pm 1.46	4.17 \pm 7.03
	Level 2 [$\mu\text{g/g}$]	10.00 \pm 4.68	15.93 \pm 6.33	18.09 \pm 19.96
	Level 3 [$\mu\text{g/g}$]	29.07 \pm 16.37	38.03 \pm 24.82	33.79 \pm 45.31
	Level 4 [$\mu\text{g/g}$]	44.48 \pm 16.19	51.87 \pm 22.83	64.54 \pm 53.15
	LOD [$\mu\text{g/g}$]	4.18	5.39	6.41
	Linearity (R^2)	0.9872	0.9941	0.99313
	Sensitivity [cps \cdot g/ μg]	846 \pm 89	113 \pm 15	194 \pm 14

The sensitivities were similar for Cu and Zn in both gelatin (Cu: 143 cps g/ μg ; Zn 175 cps g/ μg) and brain tissue (Cu: 113 cps g/ μg ; Zn 194 cps g/ μg) and increased for Mn in gelatin (1390 vs. 846 cps.g/ μg). The improved surface roughness for the gelatin standard resulted in decreased standard deviation of sensitivity (i.e. the standard deviation of the slope) for all elements.

The gelatin contained lower background levels of biologically relevant elements (except Mn) than homogenised brain. The background concentration the elements in the standard matrix dictate achievable LODs via external calibration and need to be minimised to measure elements that may be downregulated due to metal dyshomeostasis or are at low concentrations. Accordingly, three different gelatin types were investigated for background concentrations of various metals and shown in Table 3.5.

Table 3.5: Background concentration [pg/g] of gelatin materials prior and after an additional extraction step with different resins, respectively.

	²⁴ Mg	²⁷ Al	⁵⁵ Mn	⁵⁶ Fe	⁵⁸ Ni	⁶³ Cu	⁶⁶ Zn
Gelatin							
Bovine	40600±400	21300±100	2100±10	54500±340	338±9.3	530±9.4	1200±120
Fish	260±30	310±40	8.2±3.5	910±52	7.2±11	120±10	110±110
Porcine	4500±200	510±10	33±5.9	1300±98	17±11	70±35	300±170
Resin added to porcine gelatin							
Amberlite IR120+ (Na)	1.7±2.9	330±99	5.7±0.3	1260±200	20±1.1	46±8.9	69±55
Amberlite CG-50 (H)	160±19	260±170	7.1±8.0	1000±340	14±2.1	260±4.9	88±82
Bio-Rad Bio-Rex-70 (Na)	12±21	240±75	0.4±0.7	780±55	43±5.8	76±3.9	35±43
Amberlyst 15 (H)	140±52	250±63	0.6±0.7	670±24	4.5±1.2	28±1.5	33±57
Bio-Rad Chelex 100 (Na)	86±50	320±10	0.6±1	660±76	26±5.7	18±5.1	75±83

Fish and porcine gelatin contained the lowest levels, which would make these materials favourable for lower LODs. However, from these two, only porcine gelatin formed a solid gel at room temperature when using 10% solutions. The background levels were further reduced with an extraction step during standard preparation. Porcine standards were heated until liquefied and spiked with ion exchange resins, which were subsequently separated from the gelatin via centrifugation. Five different resins were evaluated to reduce metal levels in the porcine gelatin standards. The addition of resins required effective buffering of the gelatin solutions due to pH changes affecting gelatin integrity. The use of extraction resins reduced the natural background level crucially. The background level reduction for Mg, Al, Mn, Fe, Ni, Cu and Zn, elements usually naturally abundant in gelatin, is also shown in Table 3.

3.5 Conclusion

This chapter presented a novel method for the preparation of matrix-matched gelatin standards by using moulds rather than cryo-sectioning. Commercial and laboratory-made moulds were compared against cryo-sectioned gelatin and homogenised brain tissue standards. The method enhanced control of standard thickness and surface roughness compared against standards obtained after cryo-sectioning. Thickness and topography of standards were important parameters for stable sample calibration and were directly related to signal deviations and accuracy. This was shown by conducting LA-ICP-MS signal acquisition profilometry of standards made from homogenised tissue and gelatin, respectively. The homogenised tissue showed a reduced degree of control for material deposition, while gelatin standards allowed stable ablation, even after repeated ablation events. The analytical figures of merit were improved for the gelatin standards and limits of analysis were further reduced by an additional extraction step for metals during standard preparation employing different resins. The significant reduction of metal background levels increased the dynamic range for quantification of trace levels of metals in tissues.

Although tissue homogenates may model the biological environment more precisely, they were also prone to systematic error and artefacts impacting accuracy and precision and reproducible quantification. Tissue homogenates had inferior analytical figures of

merit within one experiment, and therefore would have lower traceability between different batches of standards from different laboratories. The preparation of gelatin standards in moulds was highly reproducible, improved limits of analysis, and more suited for routine methods of imaging by LA-ICP-MS.

3.6 Acknowledgments

The experiments performed with Thomas E. Lockwood on the Teflon tape moulds and the removal of background elements in gelatin solutions are gratefully acknowledged.

4 Super resolution reconstruction for LA-ICP-MS imaging

4.1 Abstract

The resolution of laser ablation-inductively coupled plasma-mass spectrometry (LA-ICP-MS) elemental bio-imaging is usually constrained by the diameter of the laser spot size and is often not adequate to explore *in situ* sub-cellular distributions of elements and / or proteins in biological tissue sections. Super-resolution reconstruction is a method typically used for many imaging modalities and combines multiple lower resolution images to create a higher resolution image. Here, we present a super-resolution reconstruction method for LA-ICP-MS imaging by ablating consecutive layers of a biological specimen with offset orthogonal scans, resulting in a 10x improvement in resolution for quantitative measurement of dystrophin in murine muscle fibres. Layer-by-layer image reconstruction was also extended to the third dimension without the requirement of image registration across multiple thin section specimens. Quantitative super-resolution reconstruction, combined with Gaussian filtering and application of the Richardson-Lucy total variation algorithm, provided superior image clarity and fidelity in two- and three-dimensions.

4.2 Introduction

The resolution of an image for most practical applications of laser ablation-inductively coupled plasma-mass spectrometry (LA-ICP-MS) using single quadrupole instruments is governed by the laser spot size, the ICP-MS total integration time, and the laser scan speed. In this context, the resolution may be defined by each sampling event of the specimen represented by each pixel of the image.

The size of a pixel in the direction of the line scan is given by $v_l t_{sc}$ where v_l is the scan speed of the laser and t_{sc} is total integration time [38]. Manipulation of t_{sc} or v_l varies the resolution of the image in the direction of the line scan. For example, halving the total integration time will halve the lateral pixel size. This scenario has been frequently

used to construct images with anisotropic (rectangular) pixels of improved resolution in the scan direction only, whilst the spacing between consecutive scans is defined by the diameter of the laser spot at the sample [117–120]. The anisotropic ratio (AR) of a pixel is given by $AR = \frac{d_l}{v_l t_{sc}}$ (Equation 1) where d_l is the diameter of the laser spot.

Conventional LA-ICP-MS imaging has made major contributions to our understanding of the role of transition metals and other elements in health and disease at lateral resolutions of 25 μm^2 to 2500 μm^2 using laser spot sizes of 5 to 50 μm [155–157]. However, there remains a pressing need to improve the resolution to adequately image subcellular localisation of bio-metals, and more recently bio-molecules via immunohistochemically assisted imaging mass spectrometry [129]. Here, proteins and other bio-molecule targets may be interrogated in tissues by tagging antibodies with lanthanide doped polymers [158] or metal nanoparticles [9]. A major difficulty for both these imaging approaches is the square relationship between signal intensity and spot size, which limits the smallest practical spot size for quadrupole-based instruments to approximately 5 to 10 μm . Below this, there is not enough material in each sampling event for detection.

Efforts to go beyond this resolution limit have involved laser oversampling and application of various deconvolution algorithms. For example, Stijn *et al.* [159] imaged the 3D distribution of ^{55}Mn in corrosion growth rings of glass at sub-micrometre resolution via overlapping spot sampling, and deconvolution with an iterative Richardson-Lucy total variation (RLTV) algorithm. An alternative approach is super resolution reconstruction (SRR) to produce high resolution images from noisy or low-resolution images. SRR is a mature technique used in many image-based fields including astronomy [110,111], magnetic resonance imaging [113,160], and light microscopy [161]. SSR reconstructs a higher resolution image by combining multiple images, which are acquired at sub-pixel distance offsets. SRR requires a nonuniform interpolation algorithm to populate pixels not filled by the lower resolution images [162,163], which typically involve linear, cubic and nearest neighbour interpolation strategies [115]. The SRR algorithm may also be applied in three dimensions in a similar manner to MRI [164–166].

3D image reconstructions by laser ablation inductively coupled mass spectrometry (LA-ICP-MS) are conventionally performed by sampling of consecutive slices of a specimen and image registration of each of these slices for integration into a final 3D image of voxels that is a representation of the original sample [67,158,167–171].

This chapter demonstrates a novel method of super resolution reconstruction (SRR) to improve the fidelity and resolution of immunohistochemically assisted quantitative LA-ICP-MS imaging with consecutive offset orthogonal raster scans in two and three dimensions. In the case of three-dimensional imaging, continuous orthogonal sampling of the specimen was undertaken until the specimen was completely ablated, eliminating image registration required by conventional approaches.

4.3 Method

4.3.1 Instrumentation

All LA-ICP-MS analyses were conducted on an Agilent 7700c series ICP-MS (Agilent Technologies, Waldbronn, Germany) coupled to a New Wave Research NWR193 (Kennelec Scientific) ArF excimer laser emitting at a wavelength of 193 nm. Laser ablation and ICP-MS parameters were optimised with a gelatin standard containing Gd with a laser spot size of 15 μm , scan speed of 30 $\mu\text{m}/\text{s}$ and laser frequency of 20Hz with the Ar carrier gas at 1.15 L/min. Calibration curves and construction of images were performed in MassImager[172], an in-house developed imaging data processing software package, and FIJI used for image visualisation [173]. The resulting calibration equations were used to convert the signal intensities of every voxel in each image to concentrations (ng/g).

For solution analyses, an Agilent Technologies 7700x ICP-MS (Agilent Technologies, Mulgrave, Australia) was used with sample introduction via a micromist concentric nebuliser (Glass Expansion, West Melbourne, Australia) and a Scott type double pass spray chamber cooled to 2°C. ICP-MS extraction lens parameters were selected to maximise the sensitivity of a 1% HNO₃:HCl solution containing 1 ng/mL of Li, Co, Y, Ce and Tl. Hydrogen was added into the octopole reaction cell to reduce interferences

from carbon due to the biological samples. Calibration curves were constructed and processed using Agilent Technologies Masshunter software.

4.3.2 Reagents

Gadolinium (III) nitrate hexahydrate, Tris-HCl (pH7.4), ethylenediaminetetraacetic acid (EDTA; 10 mM), Polyethylene glycol (M_n 400) and Gelatin from bovine skin (100 mg; Type B) were purchased from Sigma Aldrich (Castle Hill NSW, Australia).

Grace Bio-Labs (Bend, OR) supplied 6 Hybriwell™ gasket (20x9.8 mm) and clear polycarbonate cover with two ports (item number 612107, depth 0.25 mm, volume 50μL). Ultrapure HNO₃ and, Gd standard were supplied by Choice Analytical (Thornleigh, New South Wales, Australia). Anti-dystrophin monoclonal antibody (MANDYS8, sc-58754) was supplied by Santa Cruz Biosciences (Dallas, Texas). MaxPar™ Labelling kit was purchased from Fluidigm (South San Francisco, CA). Mouse on Mouse (M.O.M.™) Blocking Reagent (MKB-2213) was purchased from Vector Laboratories (Burlingame, CA). Superblock (TBS; 37535) and TBS containing 0.1% Tween-20 (28360, TBS-T) were supplied by Thermofisher, Waltham, Ma.

4.3.3 Standard Preparation

Matrix matched gelatin standards were prepared from modification of a previously described method [148], and detailed in Chapter 3. Briefly, a stock solution of 25 ppm Gd was prepared by dissolving 323.89mg of gadolinium (III) nitrate hexahydrate in 100mL of pH 7.4 aqueous buffer comprising 100mM Tris-HCl, 10 mM EDTA, and 1% w/w polyethylene glycol. A series of gelatin standards were prepared by dilutions of this stock solution in the buffer to levels shown in Table 4.1; and addition of 100 mg of gelatin to 900μl of the dilutions at 53°C with periodic vortexing.

Table 4.1: Concentrations of gelatin standards.

	Standard 1 (ppb)	Standard 2 (ppb)	Standard 3 (ppb)	Standard 4 (ppb)	Standard 5 (ppb)	Standard 6 (ppb)
Gd	1.3±0.1	16.2±0.2	61.2±0.4	241±2	893±5	3523±14

Flat homogeneous standard sections suitable for laser ablation were prepared by adhesion of 6 Hybriwell™ gaskets and clear polycarbonate covers with two ports to a glass slide. The slide was heated to 53°C for one minute on a dry heat block before pipetting 50 µL of the metal-gelatin standard mixture via the port.

The standard slide was cooled to room temperature for 30 minutes and then to -20°C in a freezer for 30 minutes or until the gel was frozen. The adhesive gasket and polycarbonate covers were then removed, and the standards stored at room temperature until required for use.

To determine the concentration of the standards, 100 µg of each standard was dissolved in 1 mL of HNO₃ and diluted to 5 mL and analysed by solution ICP-MS as described above. A 7-point calibration curve for quantification of the digest gelatin was constructed by diluting 10ppm standards of Gd as per Table 4.2. ¹⁰³Rh was used as an inline internal standard.

Table 4.2: Concentration of liquid standards.

	Blank (ppb)	Level 1 (ppb)	Level 2 (ppb)	Level 3 (ppb)	Level 4 (ppb)	Level 5 (ppb)	Level 6 (ppb)
Gd	0.00	0.2900	1.170	4.690	18.75	75.00	300.0

4.3.4 Sample Preparation

Wildtype black 6 C57BL/6 mice purchased from Jackson Laboratories (Bar Harbor, ME, USA) and rectis femoris muscle was dissected under guidelines by the Institutional Animal Care and Use Committee at the University of California, Los Angeles. Mice were maintained in the Terasaki Life Sciences Vivarium following guidelines by the Institutional Animal Care and Use Committee at the University of California, Los Angeles (approval #2000-029-43). Approval for these studies was granted by the UCLA Animal Welfare Assurance (approval #A3196-01). All mice used in the study were male.

The MANDYS8 anti-dystrophin antibody (Santa Cruz Biotechnology) was labelled with ¹⁵⁸Gd using a MaxPar™ polymer label by the manufacturer (Fluidigm) [104].

10 μ m thick (for 2D) and 50 μ m thick (3D) cryosections of mouse rectis femoris muscle were prepared for immunohistochemistry as follows. Air dried samples were washed in duplicate for 2 minutes with TBS at pH 7.4. Sections were then blocked with mouse on mouse blocking reagent for 60 min as per manufacturer's instructions [174]. Sections were washed with TBS containing 0.1% Tween-20, 2 x 2 mins (TBS-T). A 1:100 dilution of the tagged anti-dystrophin antibody to a final concentration of 2 μ g/mL with Superblock[®] diluent. The sections were incubated with this solution for 30 minutes at room temperature. The sections were washed in triplicate for 3 minutes with TBS-T followed by an ultra-high purity water wash. Sections were air-dried and stored in a dry dust free environment until required for analysis by LA-ICP-MS.

4.3.5 Optimisation of image acquisition parameters

The laser repetition frequency was maintained at 20 Hz (time between laser pulses = 50 ms) and the integrated analysis time of each plume in the ICP-MS was equal to or an integer multiple of 50 ms to minimize aliasing. Lateral resolution improvements below the spot size of the laser was based on anisotropic oversampling by the ICP-MS in the direction of the line scan. The lateral sampling interval (Δx) is a function of the total integration time i.e., $\Delta x = v_l t_{sc}$ (Equation 1). Seven ablation conditions were considered (Table 4.3) spanning various scan speeds and total integration times representing ARs from 1 to 10. The laser spot size was kept constant at 15 μ m for all experiments.

Table 4.3: Super resolution reconstruction acquisition parameters.

Acquisition	Spot Size [μm]	Scan Speed [$\mu\text{m s}^{-1}$]	Total Integration Time [s]	Sampling Interval [μm]	Anisotropic Ratio (AR)
1	15	15	1	15	1
2	15	60	0.125	7.5	2
3	15	30	0.25	7.5	2
4	15	15	0.5	7.5	2
5	15	15	0.25	3.8	4
6	15	15	0.125	1.9	8
7	15	15	0.1	1.5	10

Two raster pattern scans were performed for each condition in Table 4.3. The first data matrix was acquired from consecutive line scans from left to right for a given distance across the specimen, each line scan offset by the magnitude of the spot size of the laser (Figure 4.1(A)). This was followed by the collection of the second data matrix from a pattern scan in an orthogonal direction to the first, with the origin of ablation offset by half the magnitude of the spot size in the scanning directions of both layers (Figure 4.1 (B)). The area of ablation for each pattern was a square of $300 \mu\text{m}$ by $300 \mu\text{m}$. Standards were ablated in the same manner before and after each acquisition scheme using the same spot size, scan speed and integration time.

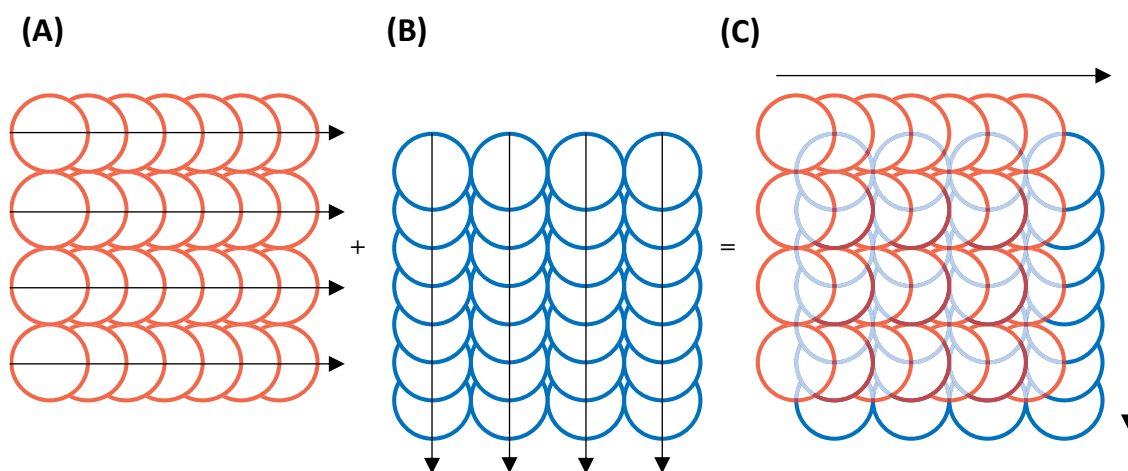


Figure 4.1: Orthogonal acquisition, (A) first line scans, (B) second line scans offset by half the magnitude of the laser spot size, (C) combined pattern for SRR processing. Arrows denote direction of scan.

For 3D images, the sample acquisition parameters consisted of a $15\mu\text{m}$ spot size moving at $30\mu\text{m}\cdot\text{s}^{-1}$ scan speed with a total integration time of 0.125s , equivalent to an AR of 4. All samples were $50\mu\text{m}$ thick and were ablated in 10-layer acquisitions. Standards were ablated at the beginning, middle and end of each 10-layer batch in the same manner as the 2D samples. The optical focus was used to test the depth of field for ablation. Refocusing of layers by $5\mu\text{m}$ of depth per layer pair was compared to unfocused ablation.

4.3.6 Super Resolution Reconstruction

The two matrices described above were made conformable for addition using the Kronecker Product [175] of the raw data (Figure 4.2 A), and the row, or column matrix as applicable (Figure 4.2 B), resulting in matrices with equal dimensions (Figure 4.2 C). These matrices were then up-sampled with null values into a checkerboard pattern (Figure 4.2 D) and shifted by the appropriate initial offset, stacked into a 3D array and trilinearly interpolated [176] (Figure 4.2 E). Finally, the two populated matrices were summed to create a 2D image (Figure 4.2 F).

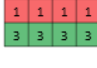


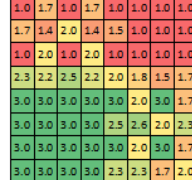
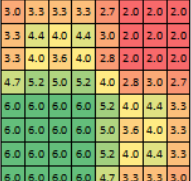
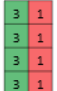
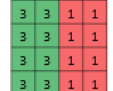
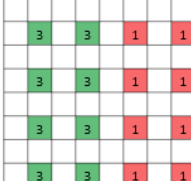
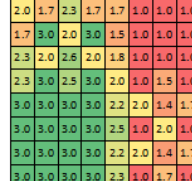
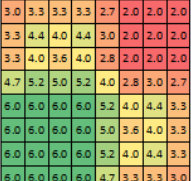
Layer	A	B	C	D	E	F
Horizontal		$\begin{bmatrix} 1 \\ 1 \end{bmatrix}$				
Vertical		$\begin{bmatrix} 1 & 1 \end{bmatrix}$				

Figure 4.2: SRR processing of two ablated layers. (A) The two layers acquired with an AR of 2 in the horizontal and vertical directions. (B) and (C) Representation of the two layers brought to congruence using the Kronecker Product. (D) Up-sampling with null values into a checkerboard pattern. (E) Layers offset and stacked into a 3D array and null values and trilinearly interpolated. (F) Populated layers summed together to produce final 2D image.

Due to the depth difference between layers, step E was performed with the layers stacked on top of each other in order of ablation. For 2D images the layers were summed together in the z-axis to create a standard image. Conversely 3D images were maintained as stacks of 2D images for further processing with trilinear interpolation between the layers.

4.3.7 Processing Algorithms

Two steps of post-processing were used to mitigate data convolution. The first step consisted of smoothing with a Gaussian kernel with dimensions equivalent to the spot size of the laser to correct the square pixel from circular laser beam artefacts as described previously [177].

The second step consisted of minimising beam related spreading of the signal using Richardson–Lucy Total Variance Regularization (RLTV) [159] applied via the DeconvolutionLab 2 in Fiji [178]. A synthetic point spread function (PSF) comprising two Gaussians diagonally offset by the radius of the laser beam was applied, as per the

original scanning pattern offset. For 3D maps, the two Gaussian PSFs were applied individually to each layer.

Quantification was performed by applying the same processing workflow to the gelatin standards in order to account for any changes to the raw data.

4.3.8 Image processing software

Image processing was performed using MATLAB for SRR then FIJI for image filtering. The MATLAB code for SRR was written inhouse and is available from (Appendix 9-1 & <https://github.com/Elemental-Bio-Imaging-Facility>). The default FIJI Gaussian filter and the DeconvolutionLab2 [178] plugin for Richardson-Lucy total variance deconvolution (RLTV) were used in this experiment. Processing was performed on both samples and calibration standards. 3D images were constructed using vtk files and imported into Paraview [179] for visualisation.

4.3.9 Statistical Analysis

Statistical analyses on the raw and processed data was performed with the Real Statistics plugin for Excel [180]. The LODs and LOQs were estimated from the calibration curves according to the following equations:

$LOD = \frac{3\sigma}{S}$ and $LOQ = \frac{10\sigma}{S}$; where σ was estimated by the standard error in the y-intercept and S was the slope of the calibration curve.

4.4 Results and Discussion

4.4.1 Optimisation of image acquisition parameters

We chose to use the expression of dystrophin in murine tissue as an exemplar target. Dystrophin is a protein found in muscle fibres and is part of the dystrophin-glycoprotein complex (DGC), a multimeric transmembrane protein complex that links the intracellular cytoskeleton and the extracellular matrix [181] that confers structural stability to the sarcolemma during muscle contraction [182]. It is a low abundant protein with a clearly defined location in the muscle membrane (Figure 4.3), making it a suitable

target for examining the improvements of SRR imaging, and the subsequent processing algorithms.

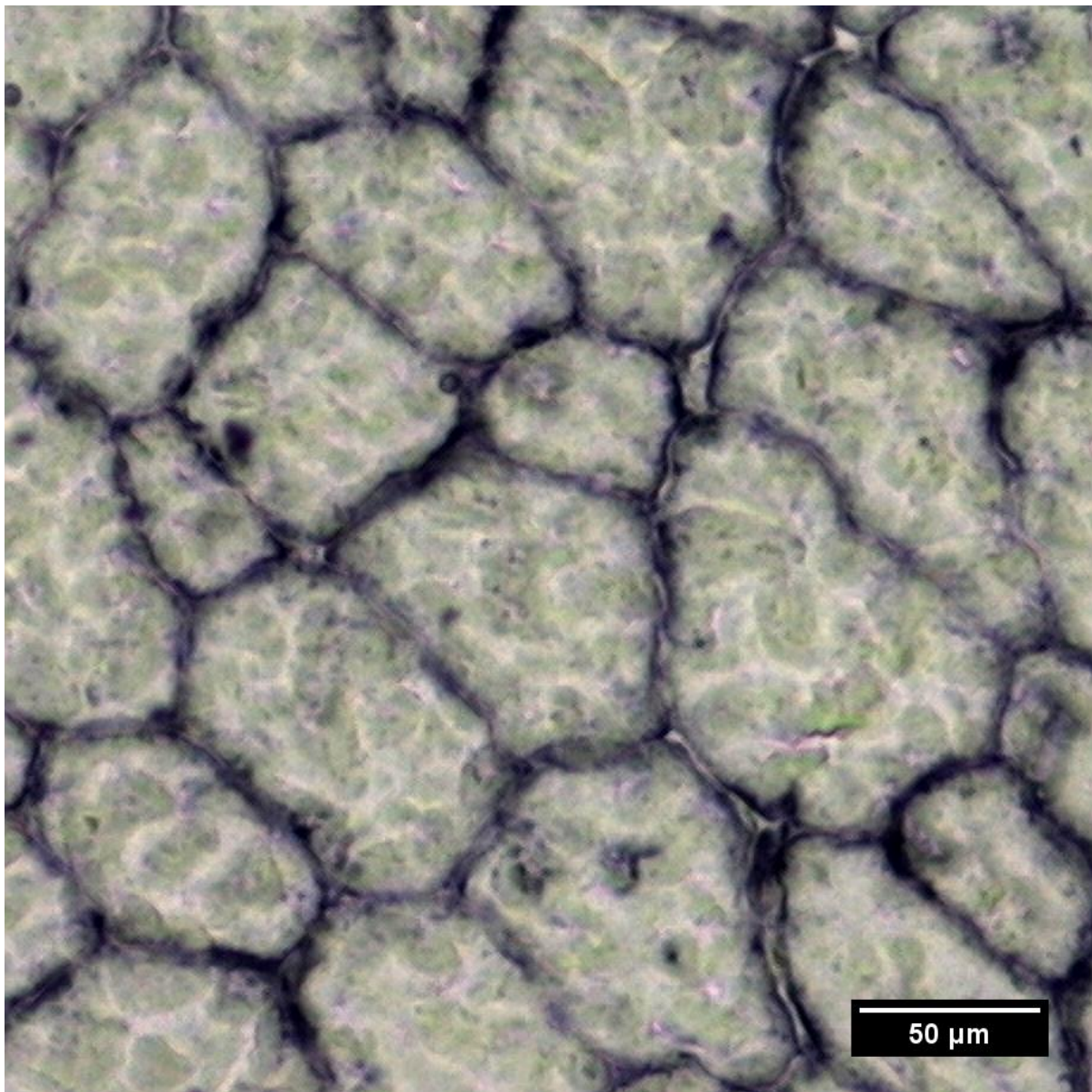


Figure 4.3: Representative photomicrograph of dystrophin in murine quadriceps. The expression of the protein is clearly seen as a honeycomb structure in the membranes of the muscle fibres. The protein was stained with Gd-labelled MANDYS8 primary antibody and detected using a goat anti-mouse secondary antibody (Sigma) conjugated to alkaline phosphatase with NBT/BCIP substrate (Sigma).

Seven scenarios were considered for investigation and optimisation of image acquisition parameters (Table 4.3) of various laser scan speeds ranging from 15 to 60 $\mu\text{m}\cdot\text{s}^{-1}$, and total integration times between 0.100 and 1.00s, representing ARs from 1 to 10, which may be thought of as a magnification factor to improve image fidelity and clarity. The

spot size was maintained at 15 μm for all experiments as preliminary scans (data not shown) indicated excellent signals of Gd for the sample under investigation, whilst spot sizes below 15 μm did not provide sufficient intensities for subsequent SRR. Spot sizes above 15 μm performed equally well in terms of AR magnification, however the criteria of optimisation were resolution improvement and acquisition speed.

Figure 4.4 depicts the resulting images from each of the seven acquisitions. Each Figure was quantified against calibration curves consisting of 6 standards. The calibration and quantification procedures are described in detail in sections 4.4.2 and 4.4.3 below. Figure 4.4 (A), (B) and (C) was constructed using conventional acquisition parameters (without SRR) in which the scan speed was 1x the magnitude of the spot size, and the total integration time was 1s, equivalent to a resolution of 15 μm per voxel and consisted of two passes without offset in the horizontal direction to maintain equivalence of ablated mass for direct comparisons of later acquisitions. Figure 4.4 (A) depicts the distribution of dystrophin as measured by the proxy Gd and is difficult to discern with patchy coverage and of limited utility. Figure 4.4 (B) shows the result of application of the Gaussian filter, and Figure 4.4 (C) the result of RLTV processing, respectively. As expected, each of these post acquisition processes did not improve the clarity of the image when compared against the raw image.

Consider acquisitions 2, 3 and 4, where the AR was constant at 2 (equivalent to a lateral and axial resolution of 7.5 μm per voxel) and the scan speed was decreased from 60, 30 and 15 $\mu\text{m}\cdot\text{s}^{-1}$, representing increments of 4x, 2x and 1 x the magnitude of the spot size. In each experiment the total integration time of the mass spectrometer was increased by a factor of the same increment in order to maintain an AR of 2.

Visual inspection of Figure 4.4 (D) (Acquisition 2, speed 4x) shows improved Gd coverage and emergence of the characteristic “honeycomb” structure of dystrophin within the muscle fibre membranes. Figure 4.4 (E) shows smoothing of the image after application of the Gaussian filter, whilst Figure 4.4 (F) demonstrates that the RLTV was effective for improving image clarity.

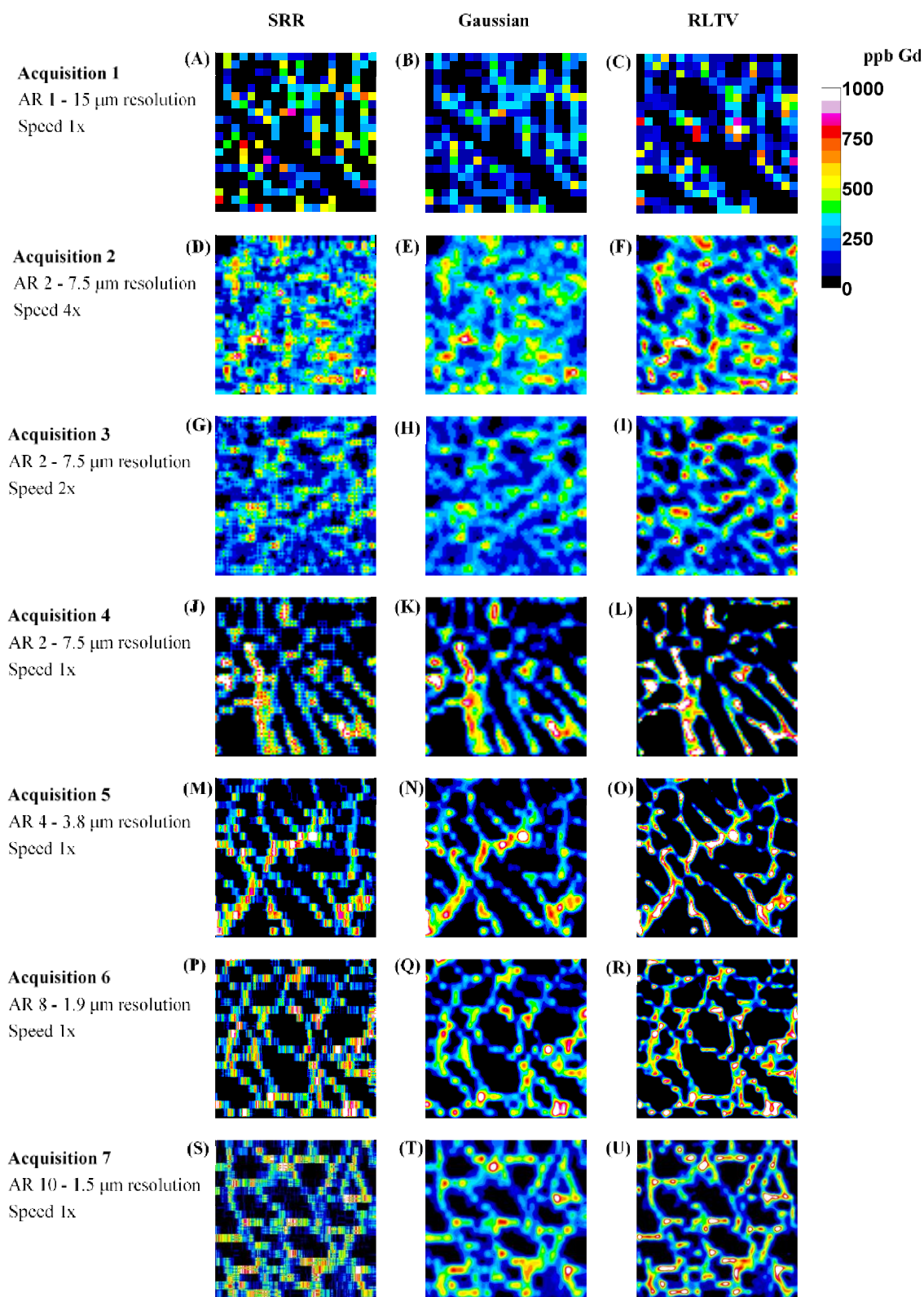


Figure 4.4: Image panel of acquisition parameter optimisation. Seven acquisitions were considered representing ARs ranging from 1 to 10. The SRR images are in column 1, except for (A), which was constructed in the conventional manner. Column 2 are the images after application of the Gaussian filter, whilst column 3 represents images after RLTV.

Similarly, Figure 4.4 (G), (H) and (I) depict the raw and post processed images (Acquisition 3, speed 2x) with half the scan speed of the former acquisition. Although the AR was maintained at 2 as before, the image clarity was superior in all three images. This improvement in clarity was a direct consequence of the washout time of the cell on this instrument (~20-50ms) becoming decreasingly significant as a proportion of acquisition time per laser pulse. The image clarity following application of the post processing algorithms was again superior to the raw SRR image. This effect is even more prominent in Acquisition 4 in which the total scan speed was at the same magnitude of the spot size (Figure 4.4 (J), (K) and (L)). Here, the distribution of dystrophin is clearly visible in the raw image and further improved by application of the Gaussian filter and the RLTV algorithm.

In general, these image blur effects were acceptable at scan speeds below two times the magnitude of the spot size, i.e. $30 \mu\text{m}\cdot\text{s}^{-1}$. Although faster scan speeds increased the Gd signal, the image blur was generally not suitable for SRR acquisition.

Acquisition 5 demonstrates that the AR can be further increased to 4, representing a lateral and axial resolution per voxel of $3.8 \mu\text{m}$ (Figure 4.4 (M), (N), and (O)). The dystrophin distribution is clearly visible in the raw image and is further clarified by application of the post processing algorithms. Acquisitions 6 (Figure 4.4 (P), (Q) and (R)), and 7 (Figure 4.4 (S), (T) and (U)) show that the AR can be further increased to 8 and 10, representing lateral and axial resolutions of 1.9 and $1.5 \mu\text{m}$ per voxel, respectively, resulting in post processed images of excellent clarity and fidelity.

In consideration of these factors, the best compromise between resolution, acquisition time, and cell washout effects was when the scan speed was less than two times the magnitude of the spot size. This compromise is only applicable to the instrument in our laboratory as new cell designs available from various vendors have significantly reduced washout times to approximately 1 to 5 ms [45].

4.4.2 Calibration

The effects of the workflow and the various processing algorithms on calibration curves are shown in Figure 4.6. Figure 4.6 (A) shows a representative calibration curve, and an

image panel of each of the six gelatin standards (Figure 4.6 (B)) obtained from ablation of a 300 μm by 300 μm square of the first layer in the horizontal direction with a 15 μm spot size, scanning speed of 30 $\mu\text{m s}^{-1}$, and a total integration time of 0.25 seconds.

In this case, the lateral resolution was 7.5 μm , and the axial resolution was 15 μm , representing an AR of 2. Similarly, Figure 4.6 (C) shows the calibration curve and the image panel of the six gelatin standards (Figure 4.6 (D)) at 300 μm x 300 μm ablated from the second layer diagonally offset at 7.5 μm (half the magnitude of the spot size) from the first. A representative post-ablation raster pattern of a standard is shown in Figure 4.5.

The analytical figures of merit for these acquisitions and the subsequent processing algorithms are shown in Table 4.4. The calibration curve of the horizontal layer has excellent linearity and a y-intercept close to the origin at 2.4 CPS, and a slope of 0.1433 CPS.ppb⁻¹. The calibration curve of the second vertical layer (Figure 4(C)) also has excellent linearity and a y-intercept close to the origin at 2.0 CPS, and a slope of 0.1237 CPS.ppb⁻¹. Summation of the slopes of these two curves yields a value of 0.2670 CPS.ppb⁻¹, and a y-intercept of 4.4 CPS. The LODs and LOQs are similar for both acquisitions.

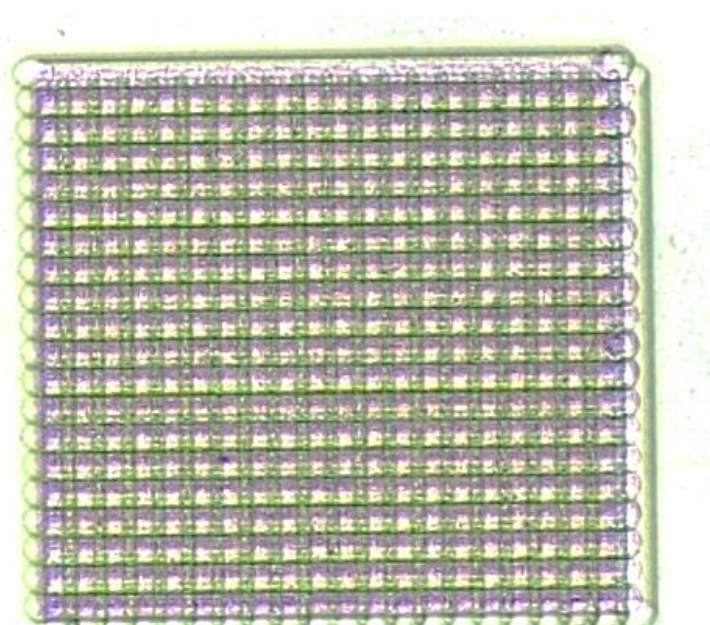


Figure 4.5: Post ablation raster pattern after two passes in the horizontal and vertical directions.

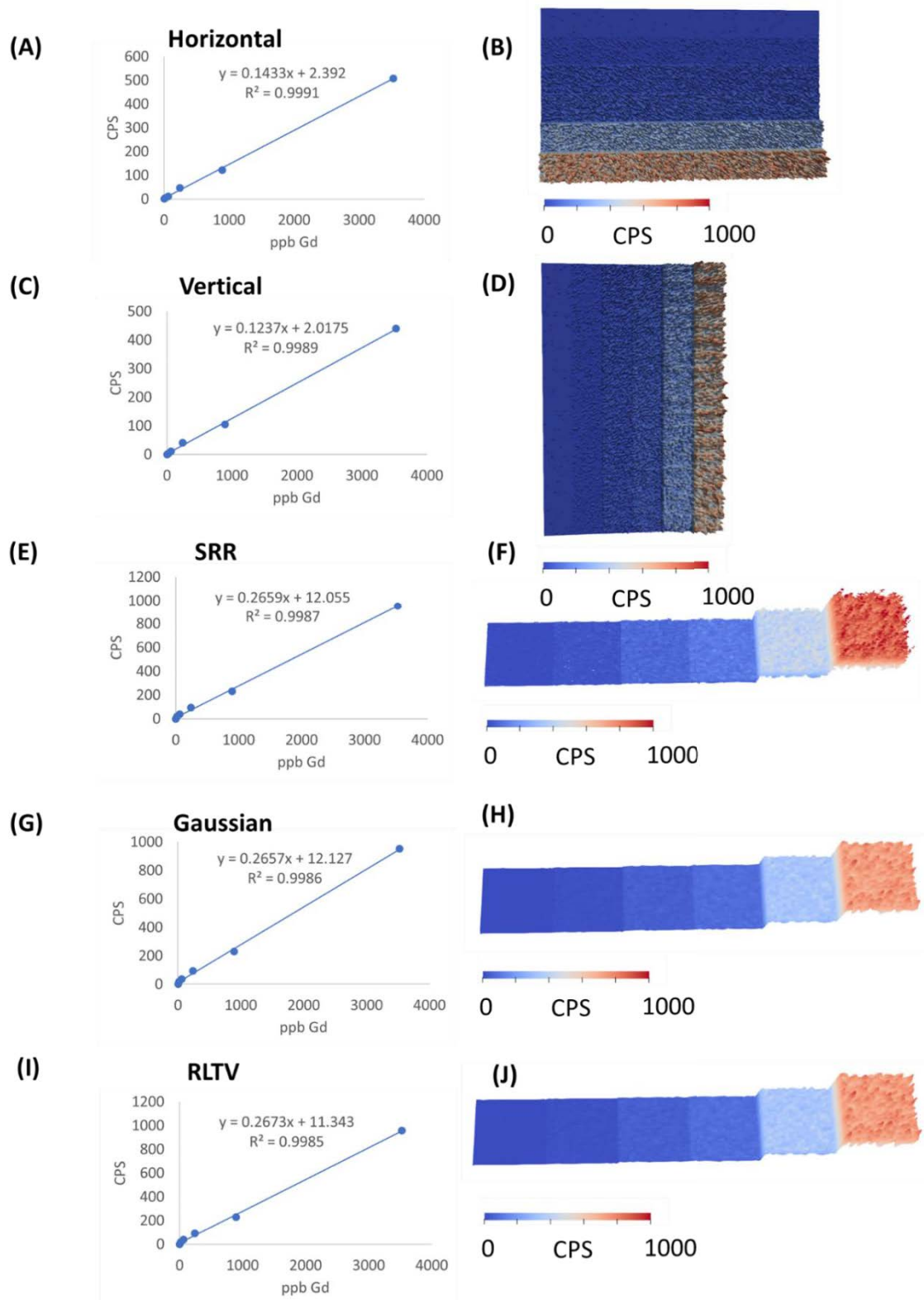


Figure 4.6 Representative calibration curves and image panels. (A) Anisotropic single layer calibration curve in horizontal direction. (B) Image of calibration standards in horizontal direction. (C) Anisotropic single layer calibration curve in vertical direction. (D) Image of calibration standards in vertical direction (E) Calibration curve after SRR with $AR = 2$. (F) Image of calibration standards after SRR. (G) Calibration curve after application of the Gaussian filter. (H) Image of calibration standards after Gaussian filter. (I) Calibration curve after RLTV. (J) Image of calibration standards after RLTV.

The effects of the first processing step combining two offset layers of orthogonal acquisition using SRR representing an AR of 2 is shown Figure 4.6 (E). The calibration curve remains linear and again is close to the origin at 12.1 CPS. The slope of the calibration curve was 0.2659 CPS.ppb⁻¹ and was not significantly different (p-value 0.870) from the summation of the slopes of the two previous cases. This was consistent with an expected doubling of the slope due to interlacing two layers into a single layer, i.e. two passes of the laser would be expected to double the signal intensity per voxel as twice the amount of material was ablated when compared against a single pass.

Table 4.4: Analytical Figures of Merit after application of the processing algorithms.

	Gradient (CPS.ppb ⁻¹)	Intercept (CPS)	Linearity (r ²)	LOD (ppb)	LOQ (ppb)
Horizontal	0.1433	2.4	0.9996	72	219
Vertical	0.1237	2.0	0.9994	82	248
Summed	0.2670	4.4	0.9995	77	234
SRR	0.2659	12.1	0.9993	89	270
Gaussian	0.2657	12.1	0.9993	91	275
RLTV	0.2673	11.3	0.9993	94	285

The calibration image panel (Figure 4.6 (F)) now consists of square voxels brought to congruence by application of the Kronecker product and bilinear interpolation of null values in the product matrix. Inspection of this standard image panel clearly shows the homogeneous distribution of Gd throughout each level of standard. The LOD of 89 ppb and the LOQ of 270 ppb have increased by approximately 15% when compared against average values from acquisitions of the single layers.

After application of the Gaussian function (Figure 4.6 (G)), the slope was not significantly different from the SRR (p-value 0.326), whilst the intercept, linearity, LOD

and LOQ were similar to the SRR processing step, indicating that for homogeneous distributions of Gd, this smoothing function would have negligible impact on quantification. Final application of the RLTV algorithm (Figure 4.6 (I)), again had no significant difference in the slope compared against the Gaussian (p-value 0.117), and negligible impact on the linearity, y-intercept, LOD and LOQ. The image panel (Figure 4.6 (J)) appears almost identical to the Gaussian smoothed image.

The average response (CPS) and % RSDs for standards near the LOQ or above (standards 4 to 6) is shown in Table 4.5 for each of the described scenarios. A one-way ANOVA showed a significant difference for averages of the response in all standards when the summed responses were compared against the processed averages (p-values < 0.05). In contrast, no significant difference was observed after application of one-way ANOVA for SRR, Gaussian and RLTV (p-value 0.24 std 4; p-value 0.09 std 5; and p-value 0.07; std 6). The initial processing with SRR, which included trilinear interpolation, decreased the %RSD in all levels of standards when compared against simple summation. Subsequent application of the Gaussian function decreased the %RSD further still, whilst application of the RLTV increased the %RSD to levels like that of the SRR processing. In all three post-processing cases the %RSD were lower than the raw acquisition data. These data demonstrate that the post processing algorithms were quantitatively invariant for homogeneous standards, whilst the Gaussian filter provided the lowest %RSDs.

Table 4.5: Average Response and %RSD for calibration standard near or above the LOQ.

	Standard 4		Standard 5		Standard 6	
	Average Response (CPS)	%RSD	Average Response (CPS)	%RSD	Average Response (CPS)	%RSD
Summed	86	44	221	31	897	23
SRR	93	36	230	24	952	14
Gaussian	93	24	230	16	952	11
RLTV	92	36	228	26	958	20

4.4.3 Quantification

In order to determine the effect of the calibration processing algorithms on quantification of heterogenous distributions within tissue sections, a single layer was ablated in the horizontal direction with a 15 μm spot at 30 $\mu\text{m}\cdot\text{s}^{-1}$ and 0.25 integration time, equivalent to an AR of 2 (acquisition 3). This same horizontal data matrix was transposed vertically (layer 2) to simulate the ablation of a second layer, offset diagonally at 7.5 μm and subjected to each of the processing steps described above. The average concentrations and % RSD this double layer test shown in Table 4.6. This test was designed to ensure that that the workflow was also quantitatively invariant for heterogenous specimens as no significant difference would be expected for average concentrations of Gd within the post-processing algorithms, and a similar trend for RSDs as was observed for the calibration data. For each processing step, the simulated two-layer sample was quantified by application of the corresponding processing step to the calibration data.

Table 4.6: Average concentrations and %RSD for simulated two-layer sample.

Layer	Concentration (ppb)	%RSD
Horizontal	690	110
Vertical	690	110
Summed	690	110
SRR	756	70
Gaussian	756	58
RLTV	772	86

As expected, application of one-way ANOVA showed there was no significant difference in average concentration of Gd between layer 1, layer 2 and the summed layers (p-value 1). However, there was a significant difference between the average concentrations when all scenarios were compared (p-value <0.05). There was no significant difference in average concentration of Gd within post processing algorithms (p-value 0.15). As before, the %RSD was reduced after SRR processing when compared against the raw data quantification. The %RSD was further reduced after application of the Gaussian filter and increased after application of the RLTV processing step.

Figure 4.7 shows the effect of each of the processing steps on image construction for the simulated scenario described above. Figure 4.7 (A) and (B) depict the horizontal anisotropic acquisition, and the transposed image, respectively. The image is of low clarity and characteristic “honeycomb” structure is difficult to discern. Application of SRR (Figure 4.7 (C)) shows the SRR composite image, demonstrating increasing clarity, whilst the Gaussian filter smooths the image further (Figure 4.7 (D)). Finally, the importance of the RLTV algorithm is shown in Figure 4.7 (E), where the distribution of dystrophin is clearly seen.

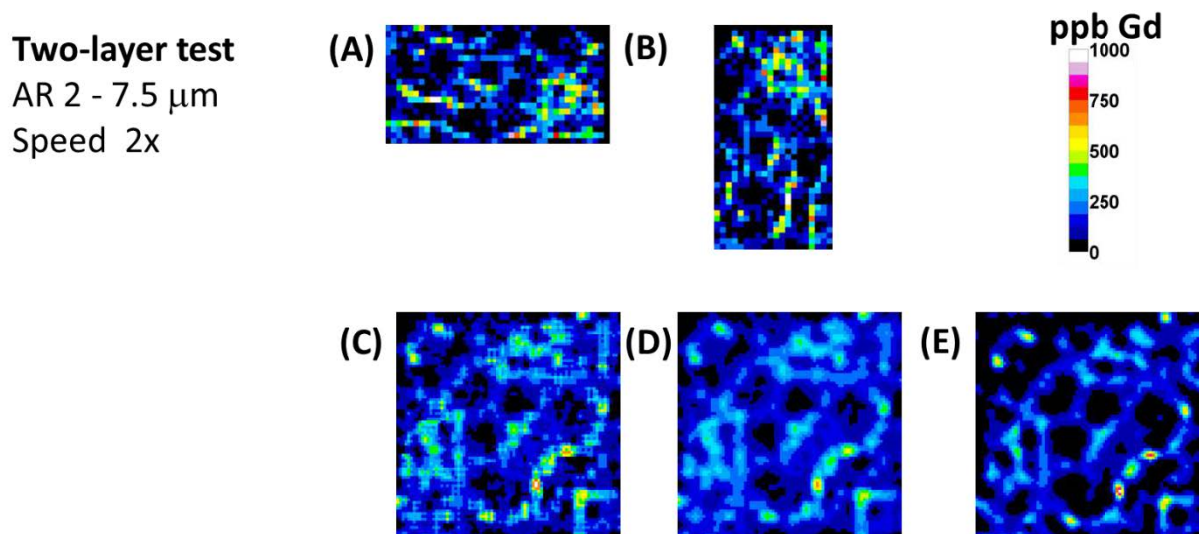


Figure 4.7: Effect of image processing on two-layer test. (A) Anisotropic acquisition of single layer in horizontal direction. (B) Same layer as (A), transposed to vertical direction. (C) SRR of (A) and (B). (D) Application of Gaussian filter. (E) RLTV image.

4.4.4 Three-Dimensional Reconstruction

Two scenarios were considered for three-dimensional reconstructions, single focus ablation, and refocusing the laser after each laser pass. These two scenarios were considered to examine the possibility that the collimated top hat beam shape of the laser and the depth of field for ablation may generate artefacts in areas where the sample may have different densities, or thicknesses. Two regions of 300 μm x 300 μm were ablated at an AR of 4 with a spot size of 15 μm and at 30 $\mu\text{m}\cdot\text{s}^{-1}$ and a total integration time of 0.125 s, with a single focus continuous acquisition; and refocusing at each pass in increments of 5 μm on 50 μm sections. In both cases, the specimen was removed completely after 10 passes. Each acquisition was processed with SRR, Gaussian filtering and RLTV and is shown in Figure 4.8.

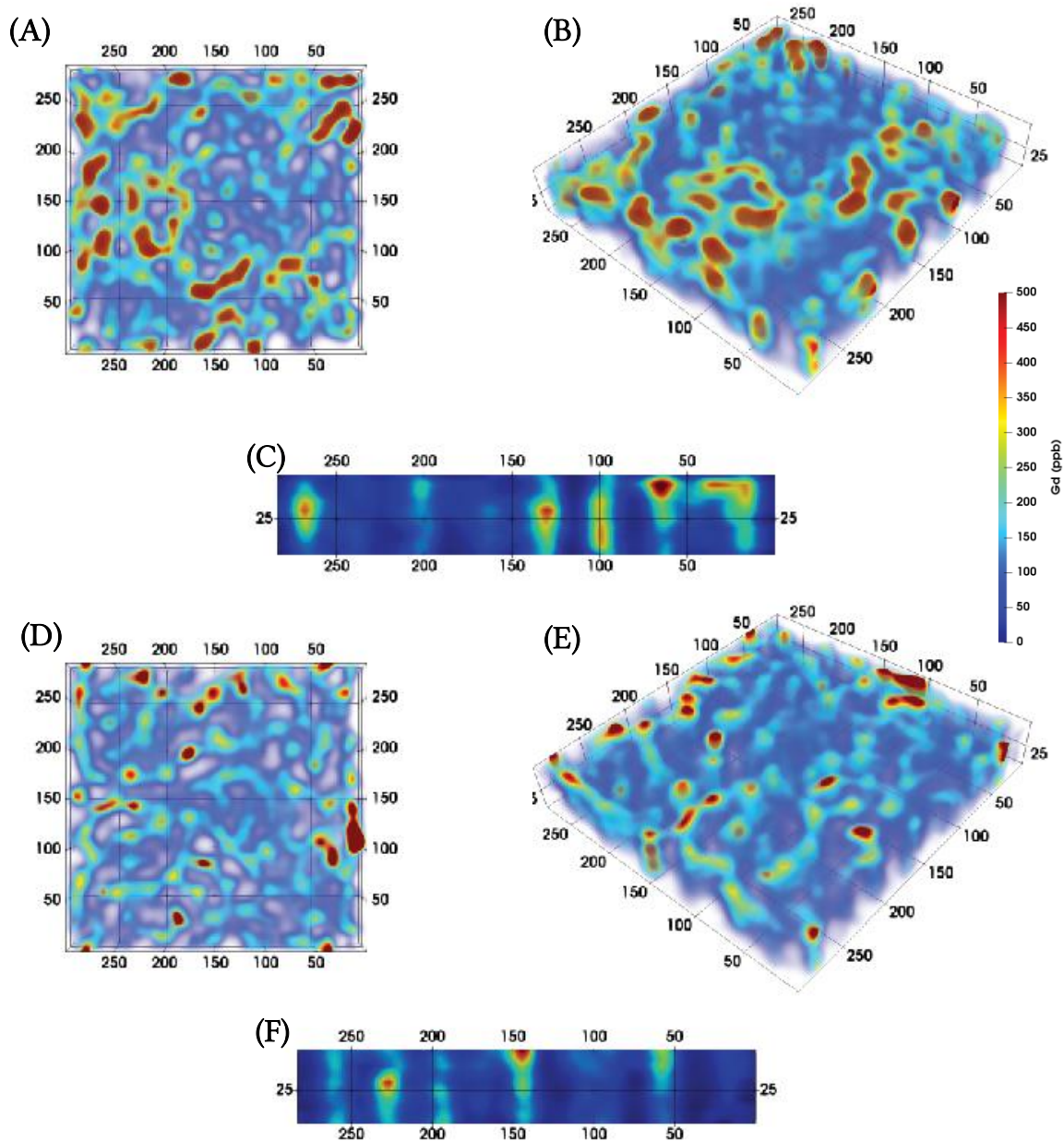


Figure 4.8: Three-dimensional reconstructions of continuously ablated 50 μm section. (A) Planar view of single focus acquisition. (B) and (C) Oblique and isometric views of refocused laser acquisition at 5 μm for each pass. (D), (E), and (F) Planar, oblique and isometric views of single focus laser acquisition. The structural integrity of the dystrophin is clearly seen throughout the 10 layers.

Figure 4.8(A) and (B) show the planar and oblique views, whilst Figure 4.8 (C) shows the isometric view of the refocussed laser acquisition. The distribution of dystrophin is seen throughout the 10 sections of acquisition. The continuity of the dystrophin along the muscle fibres in the third dimension was maintained, indicating that refocussing of the laser beam was viable method for three dimensional acquisitions.

Similarly, Figure 4.8 (D) and (E) show the planar and oblique views, whilst Figure 4.8 (F) shows the isometric view of the single focused laser acquisition. The distribution of dystrophin is clearly seen from the planar view. The isometric view displays a generally lower signal of Gd when compared to the refocussing method possibly due to reduced ablation efficiency when not refocusing. However, the oblique view shows equivalent signal down the full 10 layers of ablated muscle fibre, and the signal difference was most likely due to sample heterogeneity. Therefore, the single focus method was comparable to the refocusing method for up to a sample thickness of 50 μm . The advantage of no focus is that no prior testing of ablation depth per laser pass is required saving both sample tissue and time.

4.5 Conclusions

In summary, these data demonstrate that the SRR, Gaussian and RLTV post processing algorithms provide superior image fidelity, with no significant differences in concentration quantification within the post-acquisition processing procedures. The average concentrations of Gd across the heterogeneous sample increased by approximately 10 %, when compared against the raw data. Although this change was significantly different at $\alpha = 0.05$ when compared against the raw data, the processing steps would not affect the final interpretation of the distributions of dystrophin as relative quantification is required for this application. The lowest %RSD were obtained with the Gaussian filter, so all quantification should be reported after application of the Gaussian filter on whole tissue sections. On the other hand, the best image clarity was obtained after RLTV, so visual interpretation of structures within tissue sections should be performed after the final RLTV processing step.

Continuous ablation of 50 μm thick tissue sections and methods of a single focus and refocusing of the laser at 5 μm increments with each pass were equivalent for three-dimensional images. When compared against conventional approaches, the single focus and refocussing methods were improved in both terms of image clarity, resolution and simplicity. The single focus method is recommended up to a sample thickness of 50 μm due to the simplicity of setup. The conventional approach usually requires ablation of individual sections followed by image registration and reconstruction of the final image

by stacking the slices into a contiguous representation of the specimen. The SRR approach removes the requirement for serial sectioning and image registration and eliminates anomalies associated with cutting artefacts. Furthermore, the three-dimensional volume of the SRR approach is only limited by the focussing range of the laser, and could potentially be applied to whole organ imaging such as murine brain, kidney, pancreas etc.

The ablation cell wash-out was the most significant limitation for the total acquisition time of the specimen for any given experiment and was limited to laser scan speeds of approximately $2 d_l \mu\text{m/s}$. Beyond this speed, image blur effects negated the benefits of SRR processing. It is anticipated that this image blur problem would not be significant at speeds greater $2 d_l \mu\text{m/s}$ with new cell designs with significantly reduced washout times. Limitations of the “speed limit” of acquisitions and the maximum ARs would then migrate primarily to factors such as laser pulse frequency and speed of the mass spectrometer duty cycle, requiring the use of higher frequency laser systems and sensitive time of flight instruments.

5 Muscular Dystrophy

5.1 Abstract

There are many emerging interventions for the treatment of Duchenne muscular dystrophy, however drug approvals and clinical translations area being hampered by the challenges of quantifying functional dystrophin and related components of the dystrophin-glycoprotein complex. Standard approaches to quantification and localisation of dystrophin rely on Western blots and concomitant immunofluorescence. These approaches lack reproducibility and accuracy, require large amounts of tissue, are difficult to standardise, and not amenable to multiplexed measurements.

The chapter details the development of an immuno-mass spectrometry imaging method to simultaneously quantify and localise dystrophin in murine and human muscle sections. The samples were stained using standard immunohistochemical protocols with a dystrophin antibody labelled with gadolinium, followed by spatial quantification by laser ablation-inductively coupled plasma-mass spectrometry. The coefficients of variation were 12% and 9% for mouse and human tissue, respectively; an improvement over standard approaches, and within the FDA guidelines.

This novel application of immuno-mass spectrometry imaging facilitated the absolute quantification and sarcolemmal localisation of functional dystrophin and has the potential to quantify up to 32 dystrophin-glycoprotein complex components in a single muscle biopsy. This method will benefit research in Duchenne muscular dystrophy and will allow the interrogation of the stoichiometry of the dystrophin-glycoprotein complex. Implementation of this method in the clinic will improve the use of valuable patient resources and provide enhanced information on drug efficacy and safety and speed the pace of clinical translation for drugs in the development pipeline.

5.2 Introduction

The dystrophin-glycoprotein complex (DGC) is a multimeric transmembrane protein complex that links the intracellular cytoskeleton and the extracellular matrix [181] and

confers structural stability to the sarcolemma during muscle contraction [182]. Alterations in the protein expression of DGC components often result in muscular dystrophies, with Duchenne (DMD) and Becker (BMD) muscular dystrophy characterised by an absence or decreased expression of dystrophin. Dystrophin quantification and localisation are critical outcome measures for therapeutic trials in DMD [183]. Challenges for accurate dystrophin quantification include the absence of standards, the large size and low expression of the dystrophin protein, dystrophin-positive revertant fibres, and residual trace dystrophin [184]. In addition, tissue heterogeneity of dystrophin expression may obscure successful therapies, especially when the amount of restored dystrophin is small [184]. Regulatory authorities consider the lack of consensus on standardised methods for dystrophin quantification as a critical barrier to progress in the field [185] which has contributed to the recent controversies surrounding the approval of eteplirsen (Sarepta), the first FDA-approved DMD-specific treatment [186,187].

The current standard of dystrophin assessment is a combination of Western blotting (WB) and immunofluorescence/immunohistochemistry (IF/IHC). Assessing both the quantity and pattern of dystrophin expression is important because different patterns of expression leads to variations in the functional outcome regardless of the total amount of protein [183]. Quantification of dystrophin is confounded by high inter-laboratory variances when using Western blot and IF. A recent inter-laboratory study attempted to develop standard methods for IF and Western blotting of dystrophin [183]. Five laboratories analysed the same samples and obtained %RSDs of 23-23% for the Western blots and 22-67% using IF. These %RSDs exceed those recommended by the FDA for bioanalytical assays [188], and highlight the difficulties in standardising quantification approaches for dystrophin.

Recent advances in IF image analysis methods have led to improvements in precision in dystrophin measurement using algorithms to identify dystrophin positive fibres. Spectrin has been used as a control protein to normalise dystrophin IF images in DMD, BMD, and wildtype muscle fibres and resulted in no statistical difference between samples stained and imaged over two separate days [189]. Beekman *et al.* developed an

immunofluorescent image analysis method which improved the reproducibility with inter-assay %RSDs of 2-17%, and had sufficient sensitivity to measure small changes in dystrophin expression in a DMD patient before and after treatment with an experimental compound [190]. However the authors note that calibration curves are not available with IF, and that absolute fluorescence can differ between experimental days [190]. Aeffner *et al.* have further developed IF image analysis as an effective method of analysing dystrophin expression as a therapeutic biomarker for DMD and BMD [191]. An algorithm was developed using merosin as a mask to define the membrane of the muscle fibres, and the number of fibres in all samples were independently verified by pathologists. However, signals associated with dystrophin expression was only analysed in the areas associated with the mask.

There are currently several drugs under development to restore dystrophin production in sufferers of DMD. It is therefore essential that a reliable and reproducible method is available to measure dystrophin as a biomarker for therapeutic intervention [192]. The lack of a standardised method for the analysis of dystrophin has resulted in conflicting evidence on the use of dystrophin as a biomarker to measure therapeutic efficacy. There are reports that the data produced does not clearly establish a correlation between dystrophin levels and muscle function [192], and others suggest that dystrophin levels in a muscle biopsy correlates better with the phenotype than the genetic prediction [193]. Development of methods for biomarker measurements need to take into account that biopsies taken from patients with DMD may express low levels of dystrophin in large numbers of fibres [194], as well as account for revertant fibres [190]. Ideally, the biomarker should be reproducible and have a standardised method of quantification and demonstrate sensitivity across a range of dystrophin expression [189].

Here we present the use of iMSI as an alternative, quantitative imaging technique for analyzing protein expression in muscle fibres that may be applied to diseases such as DMD or investigate other focal muscle pathologies. Bodenmiller *et al.* have been key in establishing iMSI as an accepted technique for imaging heterogeneous cancer biomarkers. Their seminal paper qualitatively imaged 32 breast cancer biomarkers Highly multiplexed imaging of tumor tissues with subcellular resolution by mass

cytometry [195], with these authors developing new instrumentation and software to improve image resolution and cell segmentation [196,197], and expanding beyond measuring protein expression to include mRNA in their multiplexed analyses [198]. Postmortem use of quantitative iMSI has identified markers of early myocardial ischemia [199], and to show three-dimensional structural features in the murine brain [158].

This chapter details the use of iMSI for dystrophin quantification in murine and human tissue with the aim to develop a bioanalytical approach to assess therapeutic interventions of DMD and studies of DGC stoichiometry; as well as expanding the analysis to the third dimension to evaluate the effect of antibody incubation time with increasing tissue thickness.

Crucial to accurate quantification of the heterogeneous distribution of dystrophin is to objectively remove background signals due to non-specific bindings of the antibody. Therefore, three methods were evaluated; no correction, removal of data points based on a threshold of the median signal, a threshold determined by Otsu's method [200]. The latter assumes two classes of distributions (e.g. background and positive signal) that identifies a division such that the variance of each distribution is equivalent.

5.3 Methods

5.3.1 Materials

The dystrophin antibody (Mandys8) was purchased from Santa Cruz Biotechnology (Dallas, Texas, USA) and was labelled with Maxpar® Gd-158 reagent by Fluidigm (South San Francisco, CA, USA). The isotype control goat anti-rabbit antibody (ab6721 abcam, Cambridge, MA, USA) was labelled with the Maxpar® Lu-175 reagent also by Fluidigm. Bloxall and mouse on mouse (M.O.M.) basic kit were purchased from Vector Laboratories (Burlingame, CA, USA). Superblock was purchased from Thermo Fisher Scientific (Waltham, MA, USA). Tween-20 and 10x TBS from Bio-Rad (Hercules, CA, USA) to make 0.1% TBST.

Gadolinium(III) nitrate hexahydrate, lutetium(III) nitrate hydrate, tris-hydrochloride (Tris-HCl, pH 7.4), ethylenediaminetetraacetic acid (EDTA; 10 mM), polyethylene glycol (M_n 400) and gelatin from bovine skin (100 mg; Type B) were purchased from Sigma Aldrich (Castle Hill NSW, Australia).

Grace Bio-Labs (Bend, OR) supplied 6 Hybriwell™ gasket (20x9.8 mm) and clear polycarbonate cover with two ports (item number 612107, depth 0.25 mm, volume 50µL). Ultrapure HNO₃, Gd and Lu standard were supplied by Choice Analytical (Thornleigh, New South Wales, Australia).

5.3.2 Mouse models

Wild-type (C57BL/6J) and mdx (C57Bl/10ScSn background) mouse quadriceps tissues were a gift from Dr. Rachelle Crosbie-Watson from UCLA (Los Angeles, CA). Tissues containing the four quadricep muscles (rectus femoris, vastus lateralis, vastus intermedius, vastus medialis) were harvested from mice maintained following guidelines established by the Institutional Animal Care and Use Committee at the University of California, Los Angeles, and approval for the mice in this study was granted by the UCLA Animal Welfare Assurance. Muscles were frozen in OCT, sectioned at 10 microns thickness, and stored at -80 degrees C until used for immunolabelling.

5.3.3 Human tissue

Human muscle biopsies were obtained with informed consent from patients of the UCLA CDMD under University of California Los Angeles IRB-approved protocol (#11-001087). Skeletal muscle biopsies from the vastus lateralis were embedded in OCT, frozen in liquid nitrogen, and stored at -80 Celsius. The DMD patient in this study had a clinical diagnosis and prior muscle biopsy done 10 years ago that showed no or low dystrophin staining. The most recent biopsy demonstrated an intronic mutation (Intron 68) that caused an out of frame 88bp insertion. This mutation was expected to have some dystrophin expression, but low. The patient was ambulatory at age 16.

5.3.4 Histological preparation

After air-drying, the mouse muscle cryosections were washed with TBS before incubation with M.O.M. blocking reagent (Vector Labs, Burlingame, CA) for 60 min. Samples were further washed with TBST before a 5 min incubation with M.O.M. diluent followed by a 30 min incubation with the gadolinium-labelled primary anti-dystrophin antibody (Mandys-8; 1:100). Additionally, isotype controls were incubated with lutetium-labelled isotype control goat anti-rabbit antibody (ab6721 abcam, Cambridge, MA, USA; 1:500). The slides were then washed with TBST, rinsed with double distilled H₂O, and allowed to air dry overnight.

The human muscle biopsy cryosections were air dried, washed with TBS and incubated with Bloxall blocking reagent (Vector Labs, Burlingame, CA) for 10 min. The samples were then washed with TBST before a 30 min incubation with gadolinium-labelled primary anti-dystrophin antibody (Mandys-8; 1:500). The slides were washed with PBS, rinsed with double distilled H₂O, and allowed to air dry overnight.

5.3.5 3-dimensional sample preparation

To explore dystrophin expression in three dimensions, cryosections of wildtype (WT) mouse quadriceps muscle were cut at thicknesses listed in Table 5.1 and prepared for immunohistochemistry with the procedure describe above. It was necessary to determine if changing the tissue thickness required longer incubation times for the antibody to fully penetrate the tissue. Table 3 lists the incubation times and section thicknesses tested.

Table 5.1: Incubation and section parameters for 3D atlas incubation.

Title	Thickness (μm)	Incubation time (min)
A	10	30
B	30	30
C	30	60
D	30	120
E	10	30
F	30	30
G	50	30

5.3.6 Preparation of iMSI standards

Matrix matched gelatin standards were prepared from modification of a previously described method in Chapter 3.3.1. A stock solution of 25000 ppb Gd and 15000 ppb Lu was prepared by dissolving 323.89 mg of gadolinium(III) nitrate hexahydrate and 111.71 mg of lutetium(III) nitrate hydrate in 100uL pH 7.4 aqueous buffer comprising 100mM Tris-HCl, 10 mM EDTA, and 1% w/w polyethylene glycol. A series of gelatin standards were prepared by dilutions of this stock solution in the buffer to levels shown in Table 4.1; and addition of 100 mg of gelatin to 900 μl of the dilutions at 53°C with periodic vortexing.

Table 5.2: Concentrations of gelatin standards (ng/g± ng/g).

Element	Blank	1	2	3	4	5
Gd	1.33±0.06	16.8±0.15	61.2±0.4	241±2	892±5	3523.06±14
Lu	2.85±0.07	22.0±0.16	80.0±0.5	299±2	1179±4	4674.10±16.

5.3.7 iMSI

All mass spectrometry imaging experiments were performed on a New Wave Research NWR-193 excimer laser (Kennelec Scientific, Mitcham, Victoria, Australia) hyphenated to an Agilent Technologies 7700s series ICP-MS (Agilent Technologies, Mulgrave, Victoria, Australia). To maximize sensitivity and ensure a low oxide formation (ThO/Th<0.3%) with LA-conditions, a NIST 612 Trace Element in Glass CRM was ablated. High purity liquid Ar boil-off was used (Ace Cryogenics, Castle Hill, New South Wales, Australia) as the carrier gas. The low-resolution image was obtained with a laser spot size of 15 µm with a scan speed of 60 µm/s at 20 Hz, and the high-resolution images a spot size of 15 µm and a scan speed of 30 µm/s at 20 Hz. The SRR regime was used as outlined in Chapter 4.3.6

5.3.8 Image processing

Image processing was performed using MATLAB for reconstructing the high-resolution images, followed by FIJI for image filtering as outlined in Chapters 4.3.7 and 4.3.8.

5.3.9 Statistical analysis

The averages per section obtained from Otsu's thresholding were processed and calculated by Microsoft Excel.

5.4 Results and Discussion

5.4.1 iMSI in wild-type and mdx mouse skeletal muscle

Therapeutics for DMD are initially evaluated in wild type and *mdx* murine models. The feasibility of the iMSI method was therefore evaluated for the detection and spatial quantification of dystrophin with a Gd-158-labeled anti-dystrophin primary antibody in murine skeletal muscle tissue. The iMSI method was applied across a full muscle section at low-resolution of 15 μm (Figure 5.1 A), and in high-resolution at 1.75 μm (Figure 5.1 B). Here, external standards of Gd were used for quantification that were validated according to the methods outlined in Chapter 3.

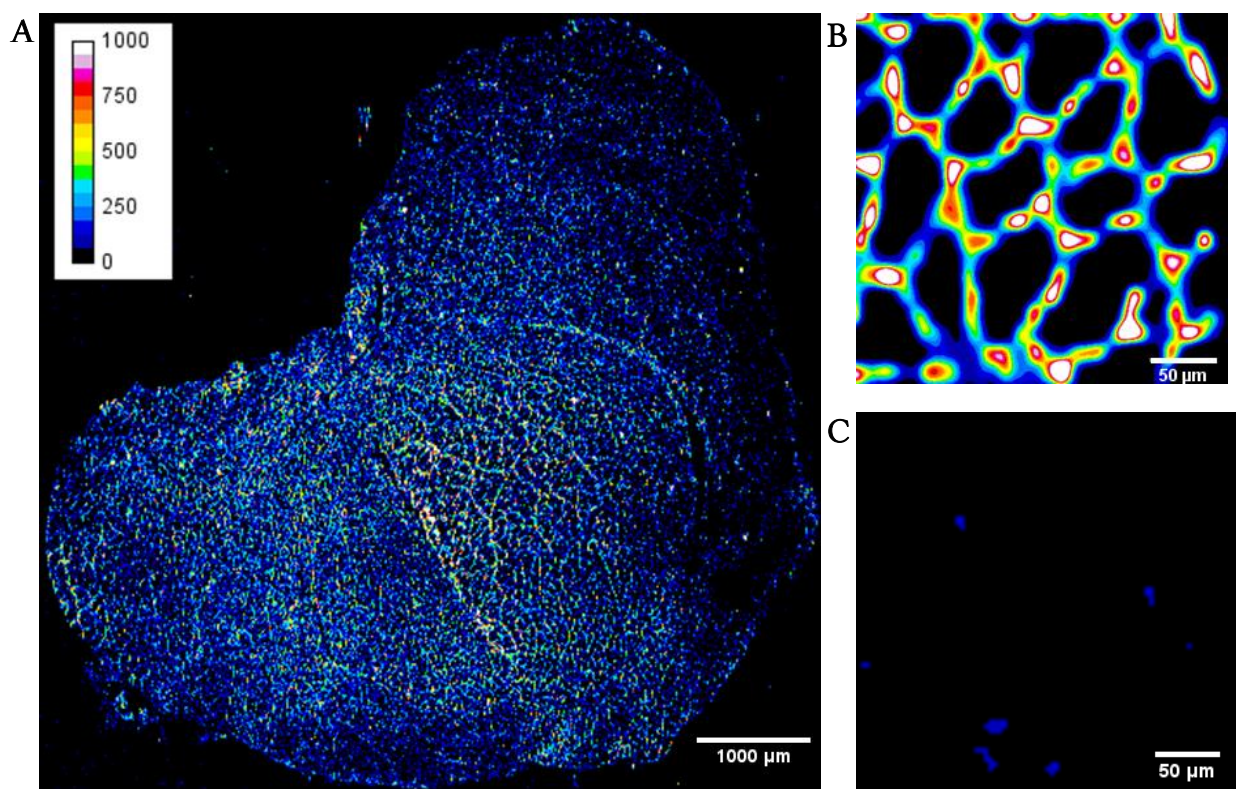


Figure 5.1: Dystrophin iMSI in wild type and mdx mouse quadriceps muscle. A, low-resolution iMSI (15 μm) of whole mouse quadriceps cross section showing expected sarcolemmal distribution of dystrophin. High-resolution (1.75 μm) images of dystrophin by iMSI in wild-type (B) and mdx mouse quadriceps (C). Quantification scale in A denotes ppb of gadolinium for all panels.

In Figure 5.1 A, the expected sarcolemmal pattern was observed, however the resolution was inadequate to discern the necessary fibre-specific concentrations. Figure 5.1 B and C show representative images obtained using the high-resolution protocols from Chapter

4.3.6 across a 300 x 300 μm section of the WT and *mdx* mouse quadriceps, respectively. As expected, the wild type image showed the characteristic sarcolemmal pattern, whilst the sarcolemmal pattern was not observed in the *mdx* mouse, which does not express dystrophin. A lutetium-labelled goat-anti-rabbit IgG antibody was applied to wild-type mouse muscle sections as an isotype control. No Lu signal by iMSI was observed above the instrument detection limits (data not shown).

Thresholding is an essential step for the quantification of proteins visualised by IHC in order to remove background signal, determine what is a “true” positive signal, and for normalising analyses between replicates. The best thresholding method for the quantification of dystrophin would ideally contain areas where dystrophin was known to be present (i.e. the sarcolemma) without biasing areas where dystrophin was not present due to non-specific bindings of the anti-body or other unexpected areas of signal. The threshold should be objectively chosen at a value that does not alter the specificity or sensitivity to identify revertant fibres nor low abundant dystrophin expression presented by the majority of DMD cases [184].

Accordingly, three approaches were investigated: no threshold, median thresholding and Otsu’s method. Median and Otsu’s thresholding were examined as these techniques are typical basic methods of thresholding for IHC analyses and are used as the foundation of more complex thresholding and segmentation algorithms.¹¹ Figure 5.2 details the analysis of a representative section of a wild type murine quadricep after acquisition of a 300 μm x 300 μm section by iMSI and application the post-acquisition processing algorithms (Chapter 4.3.6) SRR, Gaussian filtering and RLTV, equivalent to a resolution of 1.75 μm . Figure 5.2A details the histograms of the concentrations of Gd; Figure 5 B the resulting image; and Figure 5 C-E the areas of the image that were used for calculation of the final concentration with no thresholding, median thresholding and Otsu’s method, respectively.

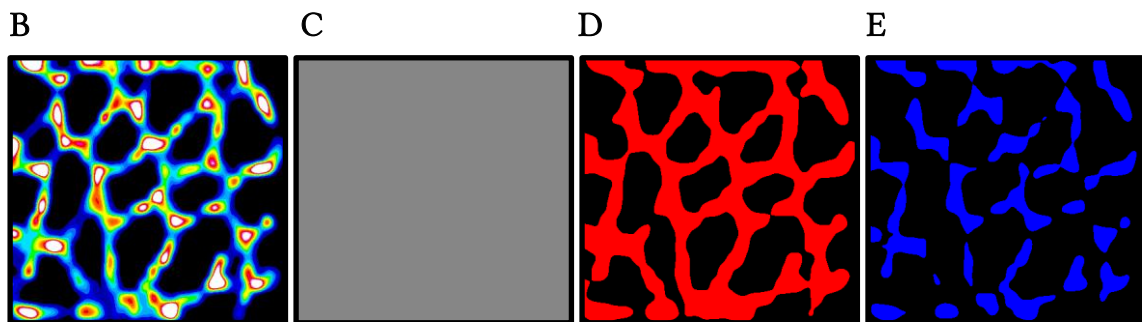
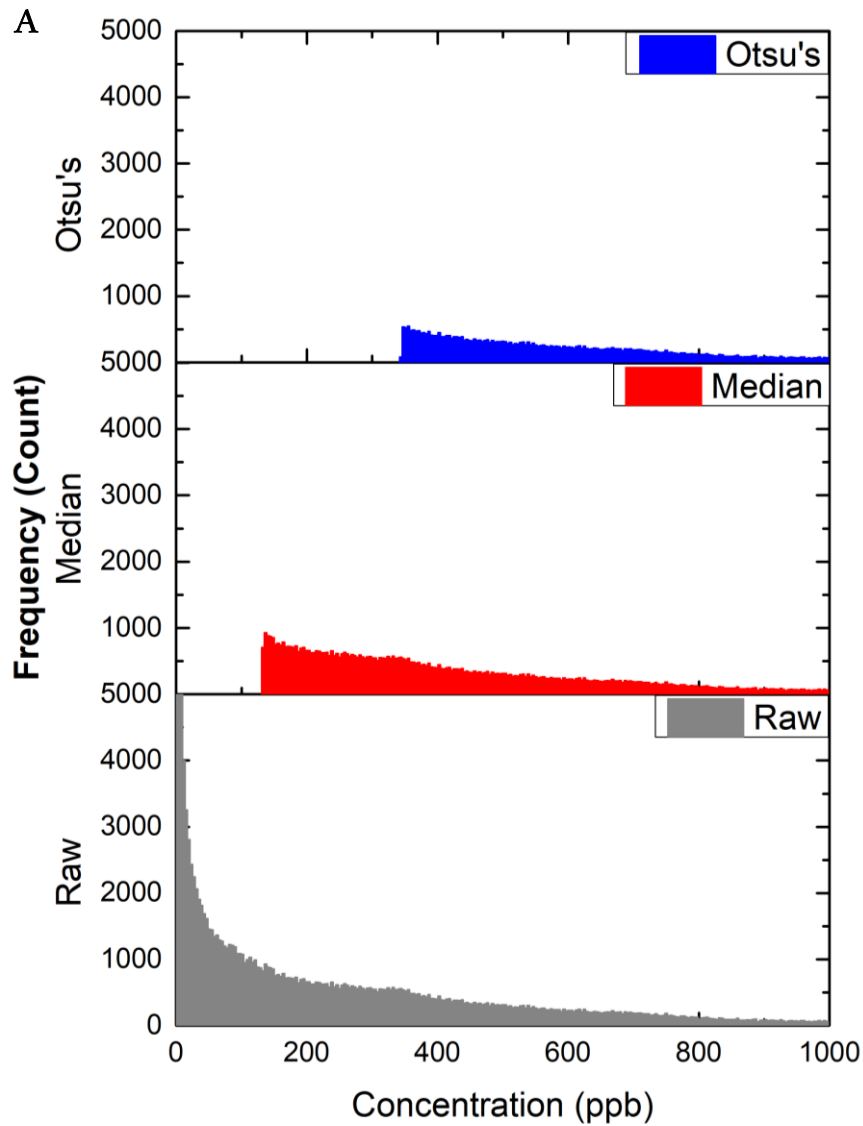


Figure 5.2: Histograms with the 3 tested thresholding methods (A). Intensity map of WT quadriceps (B) with the correlating threshold methods: Raw (C), Median (D) and Otsu's (E) using the histogram colours to represent the areas of the image used for quantification.

The raw histogram shows that roughly half of the data points (53%) were due to background signals below approximately 100 $\mu\text{g}/\text{kg}$, and calculation of the average

concentration using the entire data set (Figure 5.2C) without thresholding would clearly bias the results to well below the true value. Removal of data points below the median threshold of 132 $\mu\text{g}/\text{kg}$ from the raw image (approximately 50% of the dataset) thickened the network of membranes as represented by Figure 5.2D, although the typical honeycomb structure is easily seen. On the other hand, Otsu's method of assuming two distributions and settling on a threshold where the variances were equal resulted in a higher threshold value of 343 $\mu\text{g}/\text{kg}$, representing approximately 30% of the dataset. Thresholding by Otsu's (Figure 5.2E) method closely resembled the SRR, Gaussian and RLTV processed image (Figure 5.2B) for improved discrimination of positive dystrophin signals compared to the median method.

The method was further evaluated by analyzing six serial wild type, seven *mdx*, and seven wild type isotype control murine muscle sections. Each iMSI run consisted of the ablation of a 300 x 300 μm sections from three representative areas from each of the sections of quadriceps tissue from the WT, *mdx*, and WT isotype control samples, as shown by a representative section in Figure 5.3. Each section was calibrated against the gelatin standards before and after the acquisition of each section. The linearity of each wild type analysis ranged between 0.997-1.00. The LOD was calculated for each run, and the method LOD of 78 ppb Gd was an average of six recorded values, with one wildtype acquisition excluded as an outlier by the Grubb's test.

As expected, the *mdx* control sections showed no evidence of the

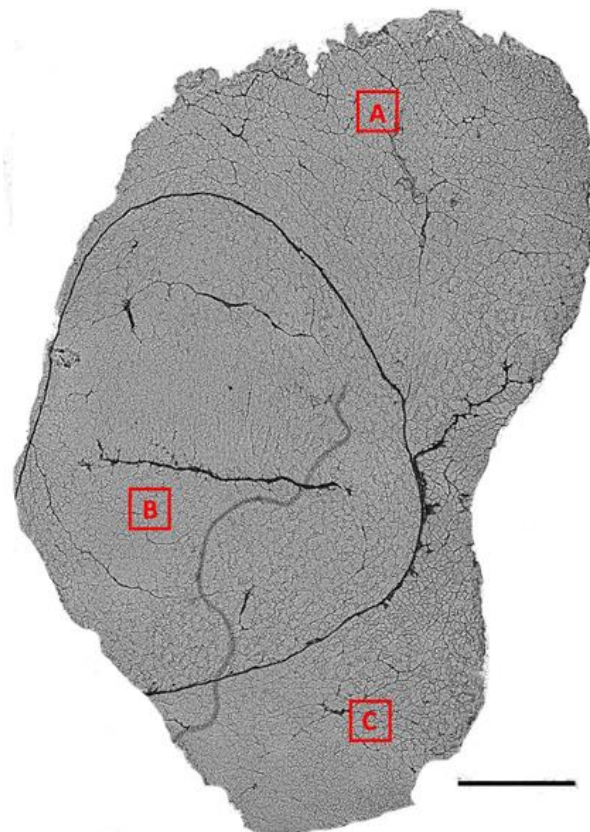


Figure 5.3: Representative areas of ablation of murine quadriceps, A, B and C. Black scale bar represents 1000 μm .

sarcolemmal pattern (data not shown), whilst Lu was below the detection limits for the isotype controls, indicating that the method was specific for dystrophin across all sections.

In all analyses of the wild type sections, the expected sarcolemmal pattern was observed. The averages of each of the six sections from each region and application of the thresholding approaches are shown in Table 5.3 below.

Table 5.3: Average values of gadolinium (ppb) and % RSDs from the regions of interest and thresholding methods for wildtype murine quadriceps

	MUSCLE REGION A			MUSCLE REGION B			MUSCLE REGION C		
	Raw	Median	Otsu	Raw	Median	Otsu	Raw	Median	Otsu
Section 1	458	689	830	427	619	687	548	786	875
Section 2	405	603	662	395	584	716	285	422	468
Section 3	328	475	558	408	614	680	432	637	718
Section 4	386	574	700	460	693	834	133	210	284
Section 5	378	591	729	474	703	801	174	250	293
Section 6	348	526	650	400	613	836	195	293	349
Average	384	576	688	427	638	759	294	433	498
% RSD	12	13	13	8	8	10	56	54	49
	Raw	Median	Otsu						
Overall Average	369	549	648						
Overall % RSD	28	28	27						

Inspection of the values in Table 5.3 show the effect of each of the thresholding methods on the calculated averages of Gd and subsequent inference of the relative amounts of dystrophin. As before, the averages of the raw data were consistently below those of the median and Otsu's thresholding, whilst the median was consistently below Otsu's method. The overall % RSD were not significantly different at approximately 28 %. As was shown in Chapter 4, that the various processing algorithms were quantitatively invariant, these % RSDs indicate that there were biological variations in the amounts of dystrophin through the muscle tissue, indicating that sampling areas and volumes must be considered before interpretation of diagnostic significance. Specifically, biopsies and sampling areas should be carefully chosen to evaluate efficacy of drug interventions or other forms of treatments. The higher values of Gd obtained from Otsu's method was

indicative of a positive bias towards larger values of Gd and is a more cautious approach to identifying positive dystrophin expression, and therefore favourable for the intended diagnostic. Therefore, Otsu's thresholding was selected for all further analyses.

5.4.2 iMSI in normal human and DMD skeletal muscle

In order to determine if iMSI provided an adequate alternative to IHC, healthy human quadriceps sections taken from a biopsy obtained from an 80-year-old were stained using a primary antibody labelled with Gd158, an avidin biotin secondary with DAB as the visualisation agent, and hematoxylin as the counterstain. The IHC section was imaged optically using a slide scanner, and a sequential section was analysed with LA-ICP-MS. Figure 5.4 shows excellent spatial correlation between the iMSI image and the IHC image. Again, the expected sarcolemmal staining pattern was observed with similar distribution amongst the individual fibers obtained with both techniques. The average concentration of Gd was 308 ppb with 18% RSD.

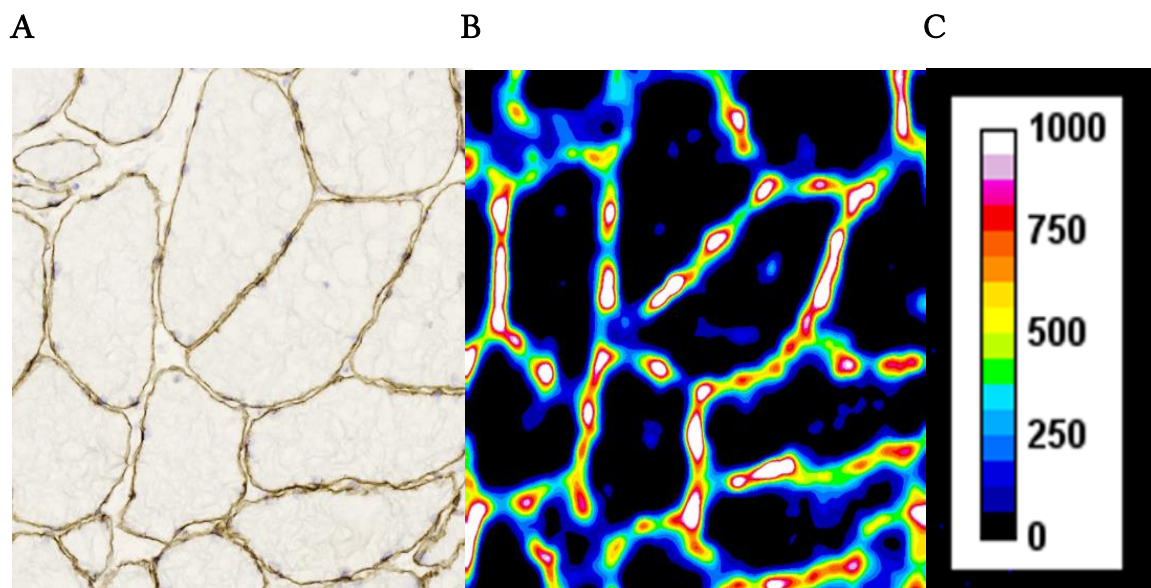


Figure 5.4: IHC with hematoxylin counterstain (A) and iMSI (B) for dystrophin in serial sections of human quadriceps muscle (80 year old). Scale bar in A denotes 100 microns and applies to both images. The same gadolinium-labeled anti-dystrophin antibody was used in both. Quantification scale in C denotes ppb of gadolinium.

A human muscle biopsy was also obtained from an 18-year-old man analysed by iMSI and is shown Figure 5.5. Dystrophin is clearly visible with the typical sarcolemma

pattern evenly distributed across the entire section. The average concentration of Gd was 293 with 9 % RSD.

A muscle biopsy was obtained from a DMD patient expected to have low dystrophin expression by genetic studies. The section was stained with the primary and secondary antibody as above. After the IHC image was taken via slide scanner, the coverslip was removed, and the section was imaged using iMSI (see Figure 5.6). The IHC image showed weak dystrophin expression, and this is confirmed by iMSI. The Gd concentration ranges from <LOD to 617 ppb, with an average value across the biopsy of 136 ppb.

It is important that new approaches to reduce the complexity of analysis provide the same information as the techniques replaced. Therefore, the first assessment is ensuring that the spatial information provided by immunohistochemistry and

the values from Western blot are improved or not lost. The results shown in Figure 5.4 and Figure 5.6 improve upon separate Western blot and IF by providing simultaneous localisation and quantification of dystrophin. iMSI uses single muscle sections, which are easily obtainable from muscle needle biopsies and does not require bulk tissue needed for Western blot and gene analysis which is generally taken through surgical procedures. It does not require changes to standard IHC procedures and reduces complexity as a secondary antibody is not required. The imaging protocols applied here had a theoretical resolution of 1.75 μm , which provided appropriate resolution and signal response to measure dystrophin expression in a range of samples that included the low expression

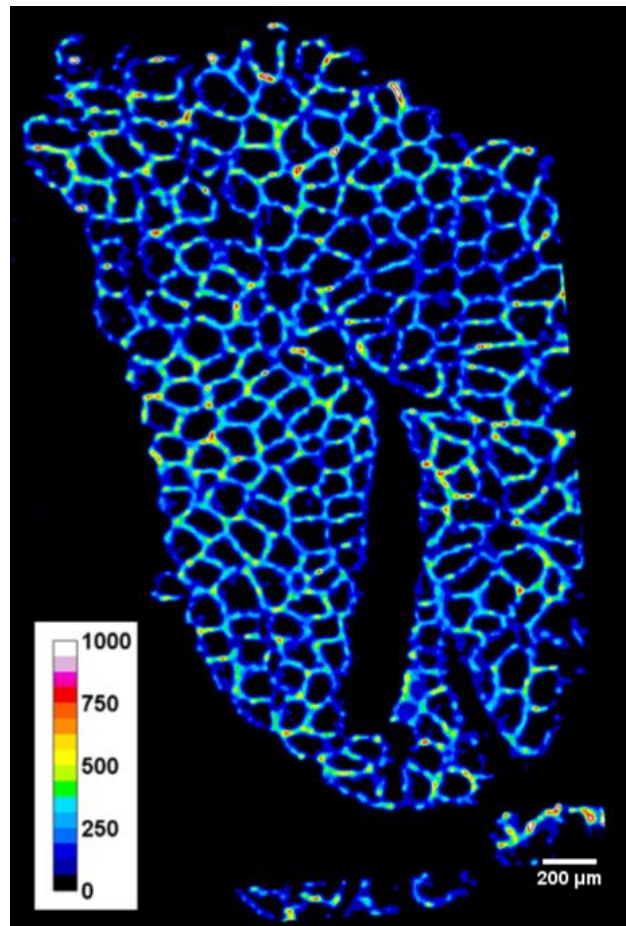


Figure 5.5: Exemplar iMSI image of section from 18-year-old male vastus lateralis biopsy. Scale bar is in ppb Gd.

in a DMD sample. Furthermore, iMSI uses easily prepared and validated external standards that facilitates comparison between clinical studies and sites. The protocol was validated for murine and human tissue and therefore can be used from the initial stages of drug development through to clinical trials.

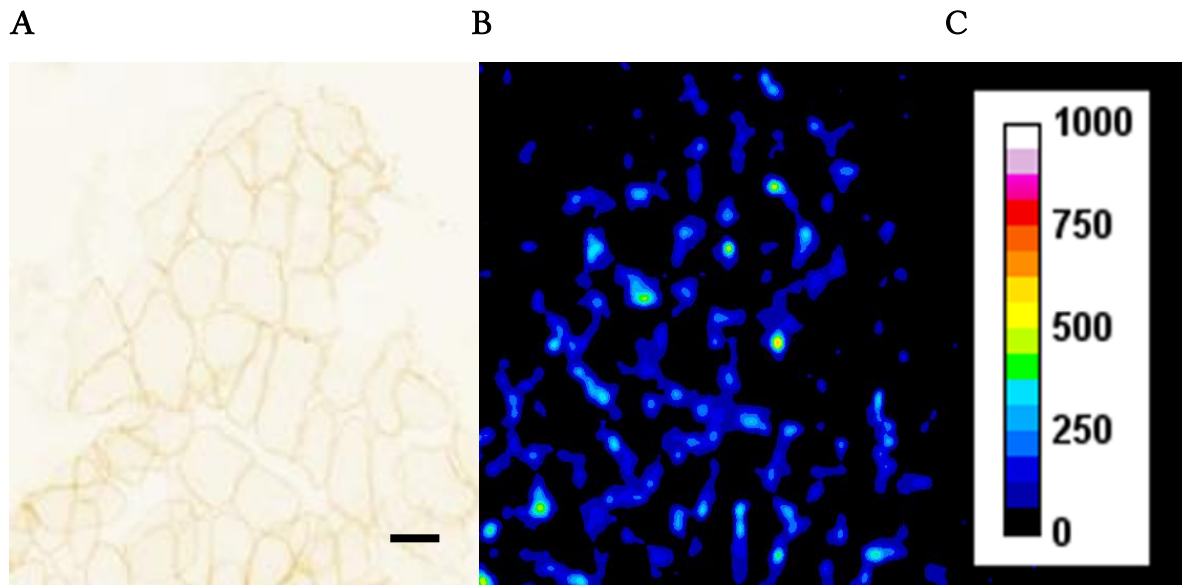


Figure 5.6: IHC (A) and iMSI (B) of dystrophin in serial muscle sections from a patient with Duchenne muscular dystrophy. Quantification scale in C denotes ppb of gadolinium in panel B. Black bar in A denotes 100 microns.

The iMSI data shown here was collected over several days, and the use of an external calibration curve provided quantitative data that measures differences in protein expression and increases the reproducibility of the technique as day-to-day variations in instrument response are accounted for. The Otsu's thresholding is not as specific as applying a mask for a membrane protein such as spectrin or merosin, however it is advantageous in other ways. Many promising therapeutics are targeting other member of the DGC such as sarcospan, with results showing that an increase in sarcospan in the muscle fibres of the mdx mouse model improved sarcolemmal defects [201]. Here, the IF images of sarcospan show that the increased expression was not confined to the sarcolemma. This increase would be identified as a positive signal using Otsu's thresholding, however, would not be measured with a masking approach. The high-resolution images shown in Figure 5.4 B and Figure 5.6 B show that the amount of

dystrophin differs fibre to fibre. This is consistent with the findings of Beekman *et al* [190], and highlight the necessity for quantitative methods that allow greater data interrogation.

The US Food and Drug Administration (FDA) industry guide for bioanalytical method validation [188] was consulted when validating this method. The document is designed as a guide only, as definitive quantitative [202] bioassays are validated according to “fit-for-purpose” steps similar to those undertaken in standard analytical protocols [203]. Accordingly, Table 5.4 summarises the analysis of Gd as a marker of dystrophin expression. The method has appropriate sensitivity to measure different levels of dystrophin expression, has high linearity with all analyses of our characterised external standards showing an R^2 greater than 0.99, and importantly the analysis was reproducible. The FDA guidance recommends that ligand binding assays should have a %RSD $\pm 20\%$, and the values obtained here for the mice and human images are below that threshold. In general, ligand binding assays such as ELISAs or Western blots are performed on homogenised tissue, reducing variability. The values obtained here highlight the quantitative reproducibility of iMSI as an appropriate method for analysing dystrophin as a biomarker of therapeutic efficacy in DMD.

Table 5.4: Technical replicates of dystrophin iMSI from consecutive serial muscle sections.

Samples	Gadolinium concentration	%RSD (Otsu's)
WT mouse Region A	759	10
WT mouse Region B	688	13
mdx mouse quadriceps	<LOD	na
Normal 18yo human vastus lateralis	293	9
Normal 80yo human vastus lateralis	308	18
DMD human vastus lateralis	136	65

5.4.3 3D iMSI of thick sections

Figure 5.7 shows the quantified images of four consecutive slices of the 80-year-old human tissue. The concentration and image clarity decreased across the four slides, with the higher %RSD shown in Table 5.4. This could potentially be caused by storage and staining artefacts or cryosectioning error, however the available data does not allow us to confirm this theory. The morphological change between slice 1 and 4 could also be explained by the structural variation along the length of the imaged fibres. The sections can be seen to be of the same region qualitatively, however the structure of some of the fibres appear altered. The changing structure of the fibre in consecutive slices highlights a potential issue when single sections are used for diagnosis or checking drug efficacy. The wrong slice could potentially miss evidence of disease/efficacy, and alternatively it could provide a false positive reading that is not indicative of the muscle. Quantitative 3-dimensional analyses may therefore be necessary to provide a clearer picture of the efficacy through a system.

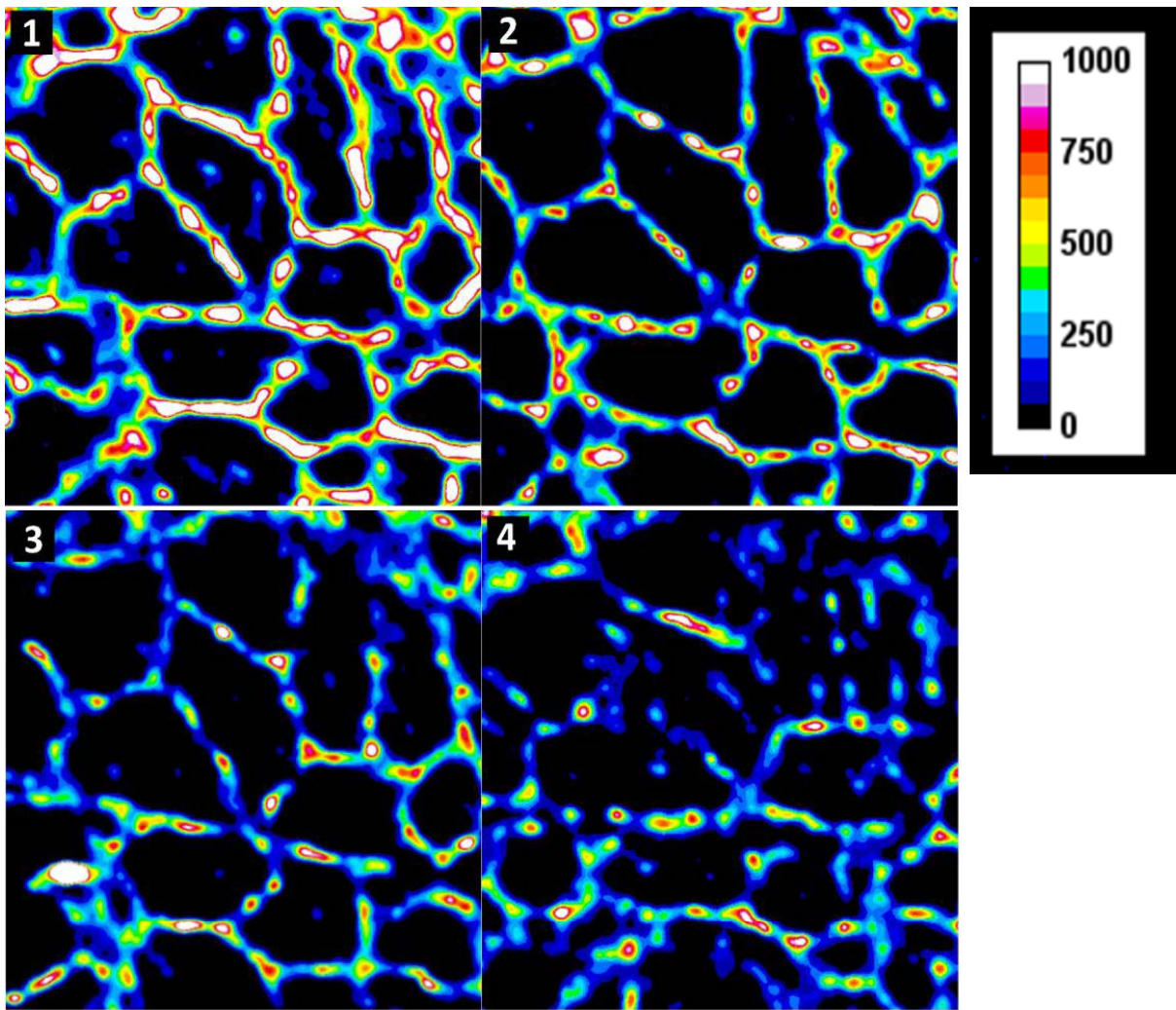


Figure 5.7: Consecutive sections of human quadricep tissue (1-4) on the same intensity scale.

Chapter 4.4.4 demonstrated that SRR iMSI of intact thick sections was a direct, quantitative equivalent to 3D optical microscopy and that the SRR imaging protocol was readily adapted to create 3-dimensional images SRR. 3D SRR iMSI required further validation of the incubation time to ensure that the antibody penetrates through the entire thickness of the tissue section. With a tissue thickness of 30 μm , the incubation time was increased in four 30-minute increments from 30 minutes, the incubation time used for the 10 μm sections, up to 120 minutes. Figure 5.8 & Figure 5.9 shows a side view of each 3D section stack's distribution of dystrophin with depth. As expected, the dystrophin distribution was not homogenous as dystrophin was only expressed in muscles fibre membranes. Dystrophin expression varied along the muscle fibre with depth, matching the earlier observation from Figure 5.7.

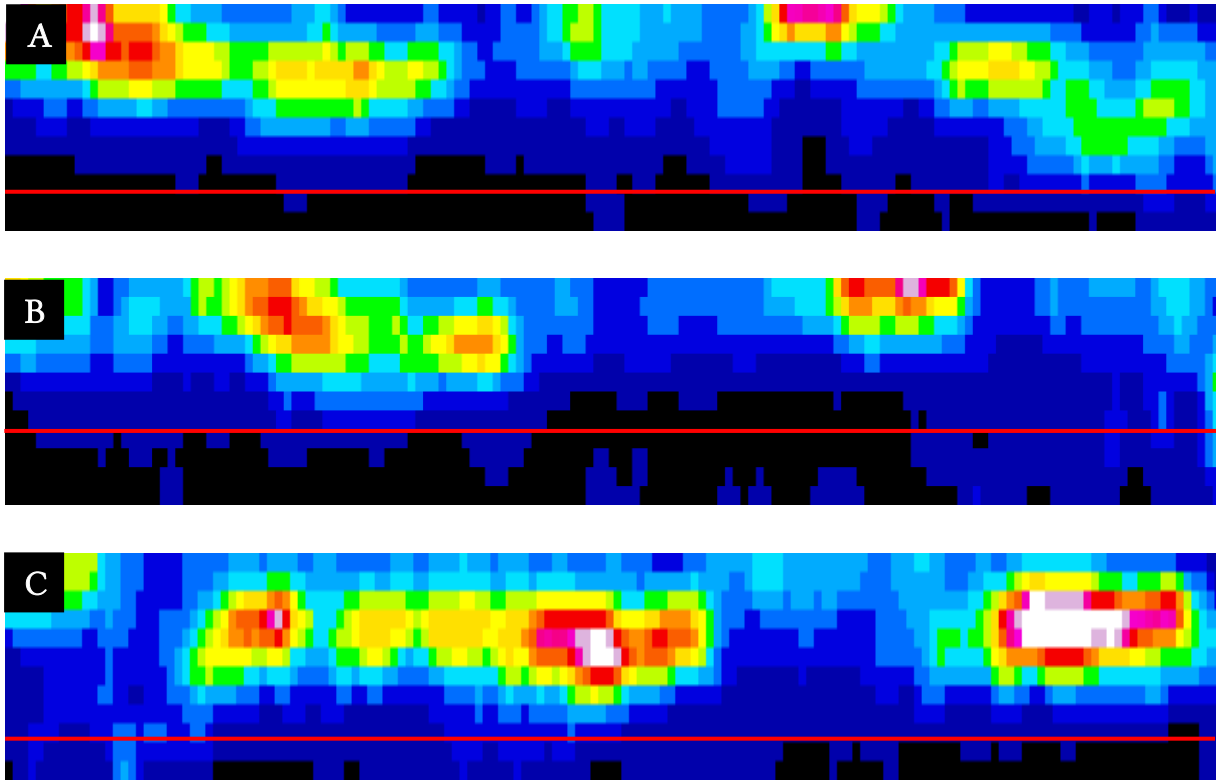


Figure 5.8: Two-dimensional image in the X-Z plane of 12-layer 3D stack of 30 μm thick sections incubated for 30 (A), 60 (B) and 120 (C) minutes on the same intensity scale. Red line signifies the final layer with signal above the LOQ.

Figure 5.8 A, B & C show that increasing the incubation time from 30 to 120 minutes did not affect the distribution of Gd and therefore dystrophin. The LOQ was used to designate the final layer of ablated tissue, which is represented in all images by the red line. The variation in the layer at the red line was ± 1 line between Figure 5.8 A, B & C. Despite this variation in the last layer, there were no signal trends between the first and last layer. It would be expected that if antibody penetration required more time that there would be an obvious gradient of signal which would be apparent in the heterogeneous distribution of dystrophin.

Figure 5.9A, B & C show the increase in SRR LA-ICP-MS ablation layers that contain dystrophin as the section thickness increases. Each section was continuously ablated until no Gd signal was observed above the LOQ, with the final layer for each thickness determined as the 3rd layer for 10 μm , 12th layer for 30 μm , and 14th layer for 50 μm . There is an indication of a linear relationship between thickness and layers of ablation (i.e. each layer is $\sim 3 \mu\text{m}$) between the 10 μm section and the 50 μm section, however the

30 μm did not closely follow this trend. This distribution variation could be explained either by changes in dystrophin expression levels between the lower layers of the different section, or cryosection effects which include uneven cuts and differences in the amount the tissue shrinks once dried.

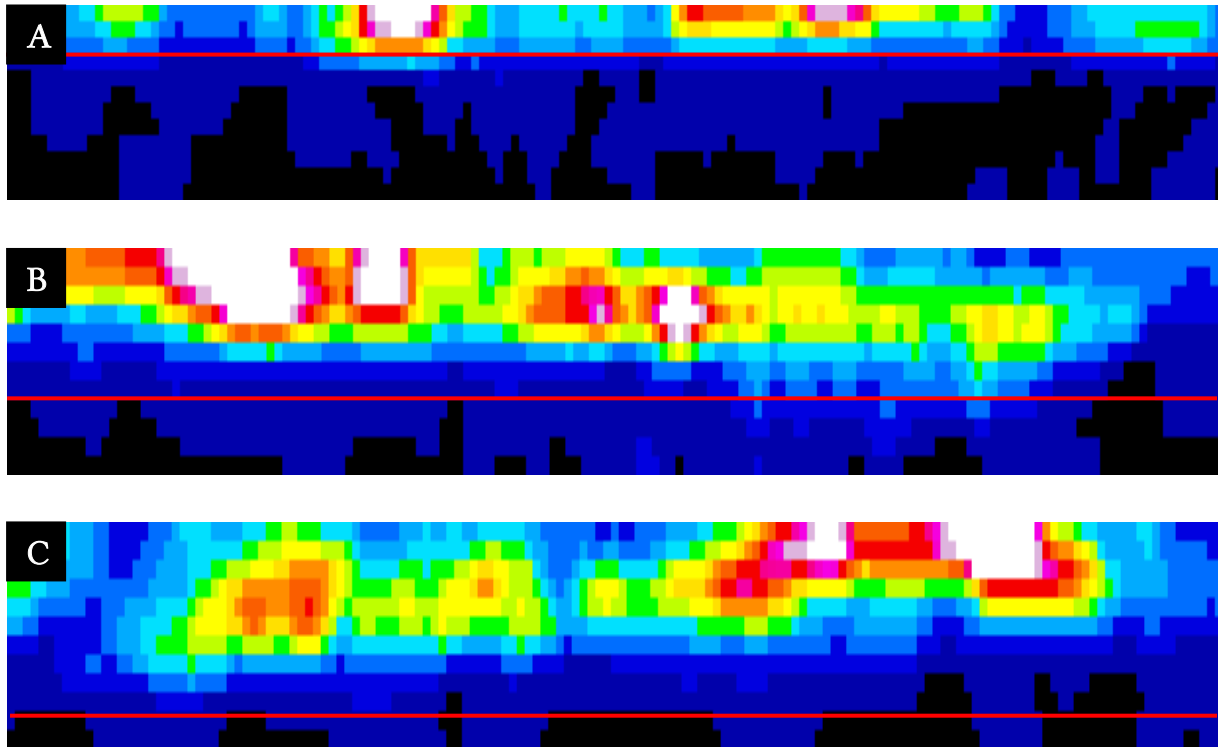


Figure 5.9: Two-dimensional image in the X-Z plane of 16-layer 3D stack of 30min incubated tissue of thickness 10 μm (A), 30 μm (B) 50 μm (C) on the same intensity scale Red line signifies the final layer with signal above the LOQ.

Further evidence of cryosection variance away from calibrated thicknesses were found in literature [204–206] which lists not just bulk accuracy issues with thickness increasing from 10 μm , but also precision issues across the surface of sections where the thickness varies significantly. Another source of error is with z-axis shrinkage of the tissue section which can vary with the density [144,207,208]. Given the heterogenous structure of muscle fibres with depth, and the density difference between fibre membrane and cytoplasm, this is likely the largest contributor of error. Despite the possible morphology related artefacts, the extra information gained from 3D analysis of quadricep tissue using SRR LA-ICP-MS over 2D analysis was evident from Figure 5.10. There are numerous interesting morphologies which mirror morphologies found using 3D fluorescent microscopy which merit further investigation [209–213]. Dystrophin expression varied

down the length of the fibre, illustrating that single section analysis of heterogeneous proteins may not provide adequate information in diagnostics and determining drug efficacy.

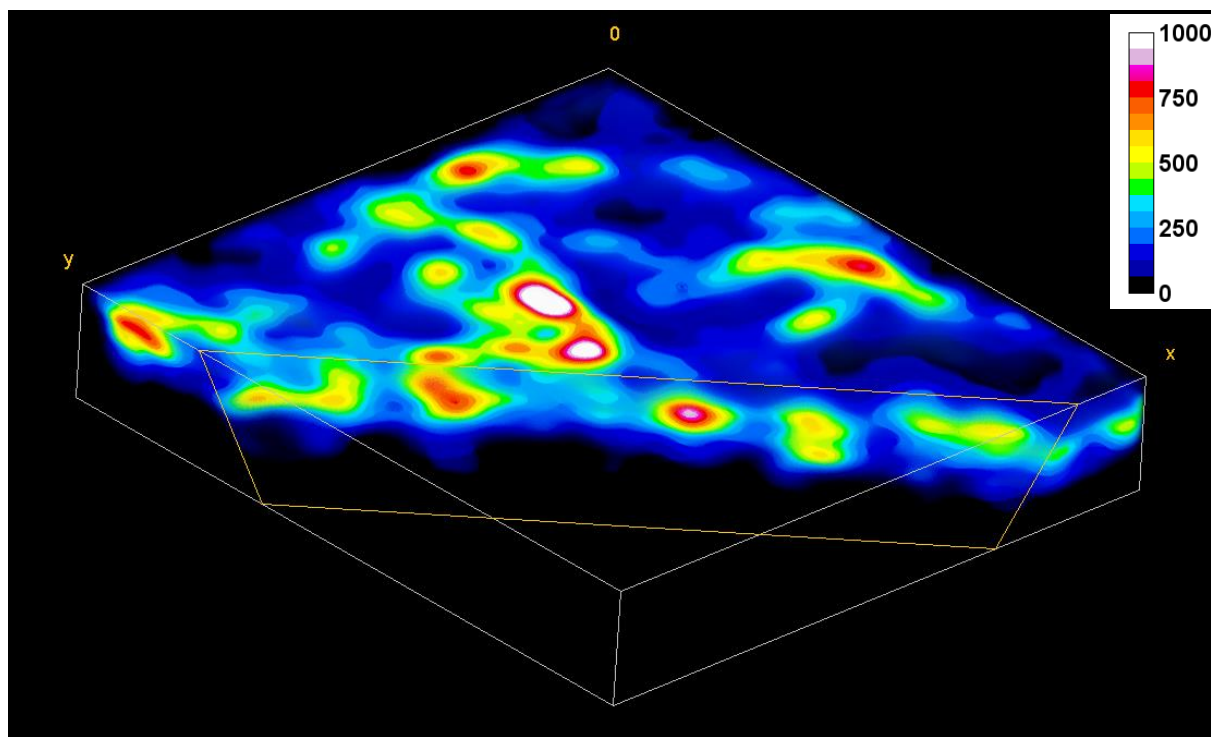


Figure 5.10: 3D image of 120min incubation time 30um section, scale in ppb of Gd.

SRR iMSI is the only 3D self-registered high-resolution LA-ICP-MS method which analyses tissue as a single section. All other 3D strategies require registration of individually cut slices into a 3D stack [69,168,205,214]. Registering images in 3D is a computationally heavy operation [215] and has “rare use of registration in diagnostic clinical practice” for the medical field [216]. Overall a registration free approach is always more desirable as it requires less computational resources and less time to process. These qualities are favourable when analysing large complex systems required for discovery in fundamental biology [217–220].

5.5 Conclusion

Quantification of dystrophin distribution in quadricep tissue was shown for murine and human tissues using SRR LA-ICP-MS and an Otsu’s threshold to segment the data analysis to only the dystrophin containing membrane. Low %RSDs were obtained across all tissue types, and the method was sensitive enough to detect the low expression in a

DMD biopsy sample. Furthermore, A 3D SRR iMSI method was developed to explore changes in tissue morphology and dystrophin expression, which negates the need to account for changes due to inherent structural variation and potential cryosectioning error. This method was simpler than other 3D LA-ICP-MS methods as it did not require image registration, and it was comparable with 3D fluorescent microscopy of muscle tissue with similar morphologies observed. Further investigation of the 3D distribution of dystrophin down muscle fibres is necessary as it may show that single section IHC is missing vital data, however the proposed workflow showed promise as an alternative tool to conventional IHC analysis of single sections.

6 Towards aptamer imaging

6.1 Abstract

Antibodies are the probe of choice for iMSI as they have a long and proven history in IHC. However, antibodies have some limitations such as steric hinderance effects and non-specific binding, or lack of specific binding efficiencies. Aptamers are novel probes comprising of structured sequences of nucleic acids which can be selected to bind to any biomolecule of interest and have not previously been used iMSI. This chapter demonstrates the feasibility of using tagged aptamers for iMSI of myelin basic protein in murine brains.

6.2 Introduction

Antibodies are the most common immunolabeling probe since their first use by John R Marrack in 1934 [221]. Naturally secreted by B cells during immune responses, antibodies bind to epitopes of specific antigens, and they have since been adopted as probes to specifically bind to targets of interest generally carrying some type of visualisation tag. This method is the foundation to the field of IHC and remains the primary method for the study of conditions and diseases.

The majority of antibodies are produced by harvesting and purifying live animal serum after incubation with a given antigen [222]. Recombinant antibodies have also been developed which are manufactured via phage libraries amplified via infection with *Escherichia coli* (E.Coli), thus reducing the requirement of production animals [223]. Antibodies produced by these methods can differ in clonality which effects their tagging abilities. Animal produced antibodies are generally polyclonal meaning they can bind to various epitopes of a single antigen. Recombinant antibodies are monoclonal and can only bind to a single type of epitope on an antigen [224]. This means, theoretically, the signal from immunolabelling with polyclonal antibodies should be higher than monoclonal antibodies. This signal increases up to a limit of what is physically possible before antibodies start blocking each other from binding to epitopes which is known as steric hinderance [225]. Steric hinderance becomes a significant problem when

multiplexing; using multiple types of antibodies to bind several different epitopes, where staining the maximum possible number of antigens is desirable. For either traditional or recombinant antibodies there is a limitation that they can only target antigens which are produced in an immune response meaning there is a limit to the number possible targets of analysis.

Aptamers are a recently developed class of probes which solve some of these antibody restrictions and are currently untested in iMSI. Aptamers are strands of oligonucleotides consisting of DNA or RNA which bind selectively to a specific molecular target [226]. They are produced in vitro via the systematic evolution of ligands by exponential enrichment (SELEX) method [227,228]. SELEX works by exposing a random artificially produced library of oligonucleotides to a molecular target, filtering out the oligonucleotides that do not bind, amplifying the bound oligonucleotides via a polymerase chain reaction [229] and then cyclically each step until the oligonucleotides with the highest binding constants remain. This makes aptamers a cheap and animal-free probe which can bind to a target even when it does not induce an immune response increasing the range of possible targets [223].

Aptamers have some additional advantages and flexibilities over antibodies. Aptamers are smaller in physical dimensions reducing incubation times for staining due to improved diffusion as well as reducing the steric hinderance issues that a larger probe may encounter [230]. Aptamers are very stable to store due to being manufactured synthetically and do not require additional reagents to keep them functional [231]. Aptamers also have the flexibility to be used as part of existing IHC protocols by replacing a secondary antibody [232]. These hybrid probe systems mean that new protocols do not need to be developed for new probes, reducing research development time. However, they are generally equivalent in clonality to a monoclonal antibody meaning reduced overall signals. This intensity issue can be compensated for by the type of tagging agent used.

Tagging agents used for iMSI by LA-ICP-MS generally contain rare earth metals or lanthanides due to their lack of natural abundance in most biological samples. The most popular tags are functionalised metal chelators such as SCN-DOTA, MeCAT and

MAXPAR™ reagents. With these tags isotopically enriched elements are used to maximise the signal measured by the ICP-MS. Recently Au nanoparticles have been used as labels for iMSI [233]. While these nanoparticles are not isotopically pure, they contain many more atoms of metal than a chelator tag in order to increase the signal measured. Another improvement of using nanoparticles is their ability to be measured by microscopy due to their fluorescence properties. For example, semiconductor nanoparticles such as quantum dots (Qdot) are used for fluorescence microscopy (FM) but are made of cadmium and selenium with lanthanide dopants all of which can be detected via iMSI [234]. They are commercially available in many formats for use in conventional IHC making them easy to adopt to iMSI. The ability to use these probes in both optical and elemental analysis allow for confirmation of the distribution of the tag. This hybrid tag has the added improvement of taking maximum advantage of either optical or elemental analysis e.g. the resolution of microscopy with the sensitivity of LA-ICP-MS.

Myelin basic protein (MBP) is a fundamental protein of life and the second most abundant of the central nervous system (CNS) [235]. MBP is produced by oligodendrocytes to supply MBP to the myelin sheath, the protective insulating layer of nerves, in the central nervous system. This protective layer of myelin sheathing can be affected by various diseases to the point of damage, known as demyelination. Thus MBP is used as a biomarker for a number of diseases primarily multiple sclerosis (MS) and neurodegenerative conditions such as dementia [236]. The diameter of these MBP containing cells are between 0.1-10µm for myelin sheaths [237] and 5-50 µm for oligodendrocytes [238] making them ideal targets to further evaluate the SRR-LA-ICP-MS method developed in Chapter 4. MBP is also a thoroughly imaged protein in mouse brains using colourmetric [239] and fluorescent tags [240] allowing easy comparison and confirmation of probe tagging of all areas of the brain under analysis. Additionally, there is a published sequence for an aptamer which binds MBP [241] thereby reducing the need for generating a new aptamer via SELEX.

This chapter demonstrates the feasibility of using a tagged aptamer to image MBP in murine brains.

6.3 Method

6.3.1 Animal Handling

As described in Chapter 2.5 harvested frozen 30 µm thick coronal sections of mouse brain were used for all experiments.

6.3.2 Lanthanide Labelling of antibodies

MaxPar[®] antibody conjugation kits were obtained from Fluidigm; (formerly DVS Sciences, San Francisco, CA) was used to label antibodies with isotopically purified europium (¹⁵³Eu) according to the manufacturer's instructions with the following modification. Tris(2-carboxyethyl)phosphine hydrochloride (TCEP; Sigma, St Louis, MO USA) was obtained as the crystalline solid and a 0.5M solution prepared fresh daily in RNase free water. The final concentration of the labelled antibodies was estimated by measuring the absorbance at 280nm using a microvolume UV-Vis spectrometer. Following estimation of the concentration, the labelled antibodies were diluted 1:2 with PBS-based Antibody Stabiliser (Candor Biosciences GmbH, Wangen, Germany) and stored at 2-8°C until required.

6.3.3 MBP Antibody labelling

The MBP antibody was labelled by 3 methods: directly labelled using MaxPar reagent, indirectly labelled with a secondary antirabbit antibody labelled with MaxPar and indirectly labelled with a secondary antirabbit antibody labelled with Fluorescein isothiocyanate (FITC).

Unconjugated carrier free rabbit anti myelin basic protein (mouse, human rat) raised against aa49-62 was supplied by LifeSpan BioSciences (LS-B6794; Seattle, WA, USA), sheep anti-rabbit secondary (STAR36Bm Bio-RAD, Gladesville, NSW Australia) and rabbit isotype control (ab37415, abcam, Melbourne, VIC, Australia) were used to stain mouse brain sections.

Mouse brain cryosections were prepared as described in Chapter 2.5. Following equilibration in PBS, the sections were blocked in a buffer comprising 1% w/v bovine serum albumin (BSA; Jackson Immunoresearch, West Grove, PA, USA), 0.3% Triton X-

100, 3% v/v normal goat serum (Sigma Aldrich) in PBS. Following blocking, the sections were incubated for 16 hours at room temperature with unlabelled or ^{153}Eu labelled MBP-antibody diluted 1:500 in the same buffer. After this time, sections were rinsed 3 x 5 min in PBS and 1 x 5 min in water or secondary. Sections were air dried and stored at room temperature until analysis.

Alternatively, MBP was visualised via a 2-hour incubation in the dark with a 1:200 anti-Rabbit-FITC secondary (Goat anti-Rabbit IgG (H+L) Secondary Antibody [FITC] NB7182 Novus Biologicals, Littleton CO).

Sections incubated with the same concentration (1:500 from 1 mg/ml neat concentration) of antibody determined from the A_{280} nanodrop readings which were 0.6mg/ml for anti-MBP and 0.55mg/ml for labelled isotype control.

6.3.4 MBP Aptamer labelling

A Myelin Basic Protein specific deoxyribonucleic acid (DNA) aptamer and a scrambled-sequence using a DNA shuffler [242] DNA control aptamer were purchased with either biotin or cysteine functionalisation at the 5' terminal end from Sigma Aldrich Customised Oligonucleotide Service (Castle Hill, Australia; Table 6.1). The oligonucleotide sequence was previously published by Rosenblum *et al.*, [241].

Aptamers were suspended in 10mM Tris pH 7.0 containing 1mM EDTA (TE) buffer to final concentration of 100 μM .

The MaxPar[®] antibody conjugation kit was used to label thiol functionalised aptamers with isotopically purified europium (^{153}Eu) according to the manufacturer's instructions with the following modification. Tris(2-carboxyethyl)phosphine hydrochloride (TCEP; Sigma, St Louis, MO USA) was obtained as the crystalline solid and a 0.5M solution prepared fresh daily in RNase free water. The final concentration of the labelled aptamer was estimated to be 40 μM by measuring the absorbance at 280nm using a microvolume UV-Vis spectrophotometer. Tagged aptamers were stored as is at 2-8°C until required.

Table 6.1: Sequences and Functionalisation of Oligonucleotides.

Aptamer	Sequence 5'-3';
Myelin Basic Protein	[Biotin]GCGTCGATTGCCATGGGTTGGGTCCGCGCAGTG AGCTCTCCTGGACCACGCAGTGAGCTCCCCTGGACC
	[cysteine]CGCGTCGATTGCCATGGGTTGGGTCCGCGCAG TGAGCTCTCCTGGACCACGCAGTGAGCTCCCCTGGACC
Scrambled	[Biotin]GGCGTCGTCACACGCTTGCCGGTGTGGCGACTC AGGCGGTGATTCGGCACGCACACTTCCGTGCTCCAG
	[cysteine]GGCGTCGTCACACGCTTGCCGGTGTGGCGACT CAGGCGGTGATTCGGCACGCACACTTCCGTGCTCCAG

Aptamers were refolded prior to use if not otherwise stated. Aptamers were diluted in folding buffer (1 μ M Magnesium Chloride $MgCl_2$ in PBS pH7.4) to a final concentration of 1 μ M. The resulting aptamer solution was heated to 95°C for 5 mins on a dry heat block then rapidly cooled on ice for 5 mins.

Myelin basic protein was detected in mouse brain cryosections using aptamers by the method of Rosenblum *et al.* [241] with the following modifications. Briefly, sections cut at 30 μ m were brought to room temperature then post fixed in in PBS containing 2% Paraformaldehyde and 0.3% Triton. Sections were washed 3 x 5min in DNase free PBS before blocking with 2% Bovine Serum Albumin (Jackson Labs) in PBS for 30 mins. For MaxPar labelled aptamers, the sections were then incubated with 1 μ M solutions of the appropriate aptamer in PBS pH7.4 containing salmon sperm DNA (4 μ g) for 2 hours at room temperature.

For biotinylated aptamers, Avidin/biotin Blocking kit (Endogenous Avidin/Biotin Blocking Kit (ab64212) Abcam) was used to block endogenous biotin in the brain [243]

according to the manufacturer's directions . Following biotin blocking, the sections were incubated with 1 μ M solutions of the appropriate aptamer in PBS pH7.4 containing salmon sperm DNA (4 μ g) for 2 hours at room temperature. MBP labelled with biotinylated aptamer was then visualised with either europium (DELFLIA Eu-N1 Streptavidin, Perkin Elmer, Glen Waverley, Melbourne, VIC, Australia), Fluorescein isothiocyanate- (FITC- Streptavidin, Sigma Aldrich, Castle Hill NSW, Australia) or Qdot (Qdot 705 Thermo Fisher Scientific, North Ryde, NSW, Australia) labelled with streptavidin.

For Eu-streptavidin, sections were washed 3x 5mins in PBS. Eu- streptavidin was diluted 1:200 in a 1X PBS and sections were covered with the solution and incubated for 2 hours at room temperature. Finally, the sections were washed 3 x 5 mins in PBS and 1x 5 mins in water before being allowed to air dry in a dust free environment.

For FITC- Streptavidin, the sections were washed 3 x 5 mins in PBS and FITC- Streptavidin (GTX30950 GeneTex) diluted 1:200 in a 1X PBS and incubated for 2 hours in the dark at room temperature. Finally, the sections were washed 3 x 5min in PBS in the dark before incubation with Hoechst 33342 diluted 1in 5000 in water (Hoechst 33342, Trihydrochloride, Trihydrate - 10 mg/mL Solution in Water H3570, ThermoFischer Scientific) for 10min in the dark. Excess solution was removed and the sections coverslipped with 80% (v/v) Glycerol in water and stored in the dark prior to examination by fluorescence microscopy.

For Qdot-Streptavidin, the sections were washed 3 x 5 mins in PBS and Qdot- Streptavidin (Qdot 705) diluted 1:200 in a 1X PBS and incubated for 2 hours in the dark at room temperature. Finally, the sections were washed 3 x 5min in PBS in the dark before incubation with Hoechst 33342 diluted 1in 5000 in water (Hoechst 33342, Trihydrochloride, Trihydrate - 10 mg/mL Solution in Water H3570, ThermoFischer Scientific) for 10min in the dark. Excess solution was removed and the sections coverslipped with 80% (v/v) Glycerol in water and stored in the dark prior to examination by fluorescence microscopy.

6.3.5 Myelin Basic Protein Antibody and Aptamer specificity analysis

MBP aptamer Biotin 5', MBP and aptamer Cysteine 5' (Sigma Aldrich, Castle Hill NSW, Australia) were tested for specific binding to Pure Myelin Basic Protein (mouse $\geq 95\%$ SDS-PAGE purified M2941 Sigma Aldrich, Castle Hill NSW, Australia). Aptamers were folded as per section 6.3.4 before usage. Relevant primary emission, irrelevant target (human serum albumin (HSA) SRP6182 Sigma Aldrich, Castle Hill NSW, Australia) and probe emission blanks were run in parallel. 2 μ L of 0.5mg/mL MBP diluted in PBS was spotted onto nitrocellulose membrane (0.45 μ m Bio-Rad Laboratories, Gladesville NSW) and left to air-dry. Denhardt's solution (1X Astral) was used to block aptamers membranes and Antibody Blocking Buffer (see Chapter 6.3.3) for antibody membranes. Membranes were blocked for 1 hours with the respective blocking solutions. Once the hour was up 3x5min wash 1X PBS and appropriate solutions were pipetted (1:100 dilution of aptamer in Aptamer buffer, and 1:500 dilution of antibody in Antibody buffer) on to membrane and incubated for 2 hours. Once the 2 hours was up 3x5min wash 1X PBS.

Optical mapping was performed using Horseradish peroxidase (HRP) functionalised to either streptavidin (for aptamer) or anti-rabbit antibody (for anti-MBP antibody) diluted 1:200 in respective incubation buffers. After 2 hours incubation with HRP probe solution wash 3x5min in 1X PBS, followed by pipetting TMB Enhanced One Component HRP Membrane Substrate (T9455 Sigma) until the membrane was covered and until a blue spot developed (~10min), then washed with MQ 3x5min.

Elemental mapping was performed using Europium (Eu) functionalised to either streptavidin (for aptamer) or anti-rabbit antibody (for anti-MBP antibody) diluted 1:200 in respective incubation buffers. After 2 hours incubation with Eu probe solution wash 3x5min in 1X PBS and leave to air-dry then analyse using LA-ICP-MS as per Chapter 6.3.7

6.3.6 Microscopy

Brightfield microscopy was performed using a Leica FS CB. Objectives of 5x, 10x, 20x and 50x with a 10x eyepiece were used to manually snake-wise raster capture the regions

of interest. Fluorescent images of FITC and stains were taken using a Leica EL6000 fluorescent light source. All comparative images were taken using the same exposure, saturation, gamma and gain. H3 and A filters were used to isolate Qdot705, FITC and 33342 Hoechst. Images were saved in a Tagged Image File Format (tiff).

6.3.7 LA-ICP-MS

LA-ICP-MS was performed on tissue using the SRR-LA-ICP-MS method as described in Chapter 4.3.6 with the following modifications. A 10 μ m laser spot size was used with a scanning speed of 20 μ m/s and a total integration time of 0.125s for high resolution images and a 35 μ m laser spot size was used with a scanning speed of 70 μ m/s and a total integration time of 0.125s for low resolution images. For elementally imaging of dot blots a conventional LA-ICP-MS was used as per Chapter 2.2 using a 35 μ m spot size, a scanning speed of 140 μ m/s and an integration time of 0.25s. The isotopes ³¹P and ¹⁵³Eu were analysed for all respective samples.

6.3.8 Preparation of iMSI standards

Matrix matched gelatin standards were prepared from modification of the previously described method in Chapter 3.3.1. A stock solution of 25000 ppb Eu was prepared by dissolving 844.95 mg of europium(III) nitrate hydrate in 100 μ L pH 7.4 aqueous buffer comprising 100mM Tris-HCl, 10 mM EDTA, and 1% w/w polyethylene glycol. A series of gelatin standards were prepared by dilutions of this stock solution in the buffer to levels shown in Table 4.1; and addition of 100 mg of gelatin to 900 μ l of the dilutions at 53°C with periodic vortexing.

Table 6.2: Concentrations of gelatin standards (ng/g).

Element	Blank	1	2	3	4	5
Eu	61.8 \pm 0.51	291.7 \pm 2.63	560.4 \pm 5.70	1076 \pm 19	2591 \pm 31	4931 \pm 57

6.4 Results and Discussion

6.4.1 Antibody vs Aptamer

As antibodies are the traditional means of staining tissue for a specific epitope they were used as benchmarks to which aptamers were compared. Comparison was done both by a conventional IHC methods using fluorescence microscopy and using LA-ICP-MS for elemental imaging. Before this comparison the aptamer sequence used for the MBP aptamer needed to be confirmed for binding specificity. This was done by dot blot analysis in the following section.

6.4.2 Aptamer binding confirmation via dot blot

Dot blots are a simple way to simulate the labelling of an antigen using a membrane instead of tissue. Conventionally done using colourmetric tags, the MBP aptamers were tested using both the colourmetric and elemental tags. This was done to first confirm the aptamers were binding visually, and then to more closely simulate the final labelling regime using elemental tags and LA-ICP-MS.

Figure 6.1 displays the five membranes used to test the binding of MBP aptamer via a colourmetric tag. To show that labelling is specific 3 controls were performed (seen in Figure 6.1 A-C) where either the protein or the probe was omitted from the protocol or where another protein was used, in this case HSA instead of MBP. All these controls show no positive signal thereby no contamination of solutions was assured. Figure 6.1 D & E are the only membranes which show signal, and both contain the MBP aptamer. Figure 6.1 D is the unfolded MBP aptamer which was assumed to be the non-binding state of the aptamer. Figure 6.1 E is the folded MBP aptamer and shows equivalent signal to the unfolded aptamer. Both aptamers were diluted in the folding buffer, so it is possible that the heating step of the folding protocol was not required to conform the aptamer into a binding form. Despite this the MBP aptamer was shown to bind selectively to MBP with colourmetric tag visualisation.

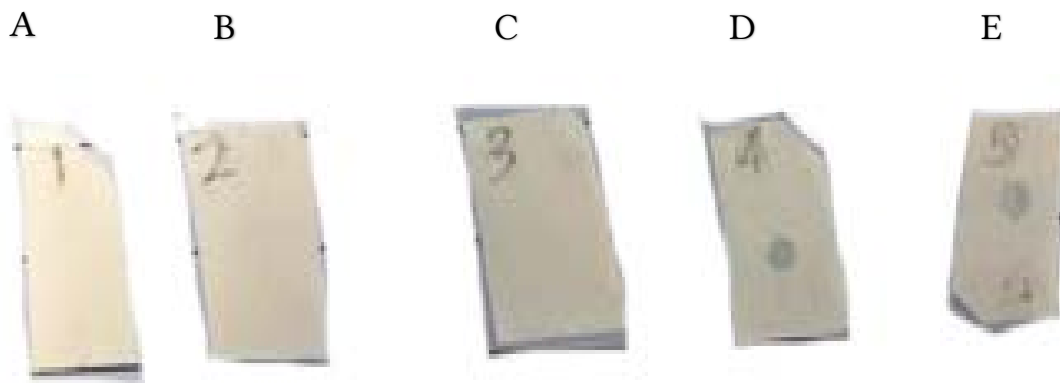


Figure 6.1: Dot blots of MBP only control (A), MBP Aptamer only control(B), human serum albumin control (C), unfolded MBP aptamer 5' biotin (D), and folded MBP aptamer 5' biotin (E) all visualized with streptavidin HRP and TMB substrate.

Figure 6.2 is the elemental image of the 7 membranes used to test primarily and secondarily tagged MBP aptamers visualized with elemental tags. For this study the controls were expanded with an isotype control comprised of a scrambled sequence aptamer. Of the 4 controls the two controls containing MBP (Figure 6.2 A & E) show faint signal while the other controls without protein show no signal (Figure 6.2 F & G). This faint signal can be attributed to incomplete blocking which can only be seen by elemental but not colourmetric imaging. This shows the sensitivity improvement between elemental and colourmetric tagging.

The dot blots of both thiol and biotin functionalised aptamers had positive signals to varying degrees. The folded aptamers (thiol 5' Figure 6.2 B and biotin 5' Figure 6.2 D) had clear high signals, showing the “coffee stain” patterns of the dried protein. The thiol 5' aptamer had significant background signal when compared to the biotin 5' aptamer. This was possibly due to degradation of the aptamer making it stick to the nitrocellulose. This change in binding likely comes from the TCEP reduction step during MaxPar tagging as this is the major protocol difference between the two dot blots. The third positive stain of unfolded biotin 5' aptamer is a clear dot shape but at a lower signal intensity. This confirmed the result from the colourmetric dot blots and gave further evidence of natural folding of the aptamer in the folding buffer despite lack of the heating

step. However the significantly lower signal reduced its efficiency for labelling of real tissue samples.

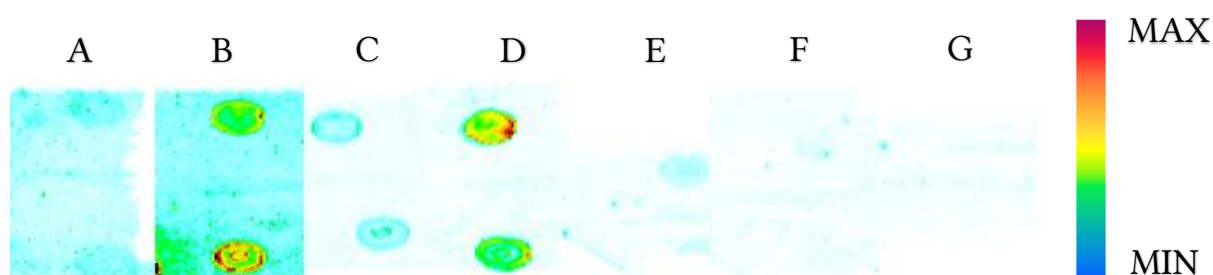


Figure 6.2: Elemental images of dot blots for folded Scrambled MBP aptamer 5' thiol tagged with ^{153}Eu control (A), folded MBP aptamer 5' thiol tagged with ^{153}Eu (B), unfolded MBP 5' biotin tagged with streptavidin Eu (C), folded MBP 5' biotin tagged with streptavidin Eu (D), MBP only control with streptavidin Eu (E), MBP aptamer 5' thiol tagged with ^{153}Eu only control (F), and MBP aptamer 5' Biotin only control (G).

The results from the colourmetric and elemental dot blots demonstrated the specificity of both the thiol and biotin functionalised MBP aptamers to MBP.

6.4.3 Fluorescence microscopy comparison

FM was used to investigate the distribution of MBP in mouse brain sections. Since MBP has not been mapped by iMSI, this was an important confirmation step to match distributions of fluorescent tags with the elemental tags used later in this chapter. FITC and Qdots were used to tag aptamers in order to compare their signal and distributions before elemental imaging. Hoechst 33342 was used for nuclear staining so that the nucleus containing region of oligodendrocytes could be isolated. Only the biotin 5' MBP aptamer was used for this section due to the simplicity of the protocol, thereby minimising additional variables of comparison.

FM serves as the first direct comparison of the binding differences between the MBP antibody and MBP aptamer. Given that a polyclonal antibody was compared to an aptamer, which is equivalent to a monoclonal antibody, the signal was expected to be lower for the aptamer. Figure 6.3 A & B shows this reduced signal for the MBP aptamer but not by a significant margin. For both images an oligodendrocyte was identified by a nucleus stained blue encapsulated in green tagged MBP probe as per the white arrows in Figure 6.3 A & B.

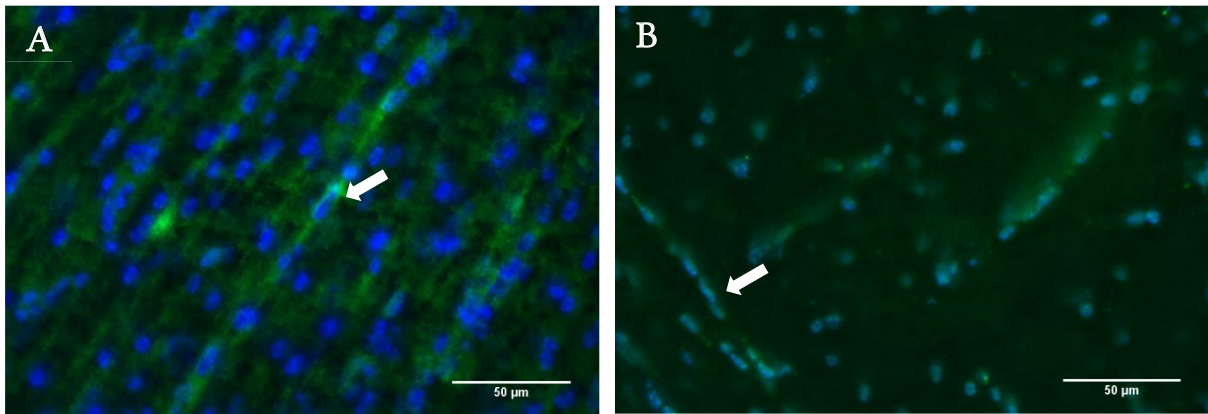


Figure 6.3: Mouse hippocampal formation stained with Rabbit antiMBP AntiRabbit-FITC (Green) and Hoechst 33342 (Blue) (A) and MBP aptamer 5' Biotin and Streptavidin FITC (Green) and Hoechst 33342 (Blue) (B). The white arrow points to an oligodendrocyte.

For staining via Qdot the signal from the aptamer stain was very high for the same microscope conditions as the FITC staining (see Figure 6.4). A portion of this was attributed to increased tag brightness as Qdots are known to be much brighter than fluorescent chemical tags [244] but the lack of specificity in most areas also point towards a staining related issues such as either overstaining due to high concentration of tag or insufficient blocking between the tissue and the Qdots. There was some evidence of specific tagging as shown by the oligodendrocyte but given the background signal this was less certain than the FITC tagged stains.

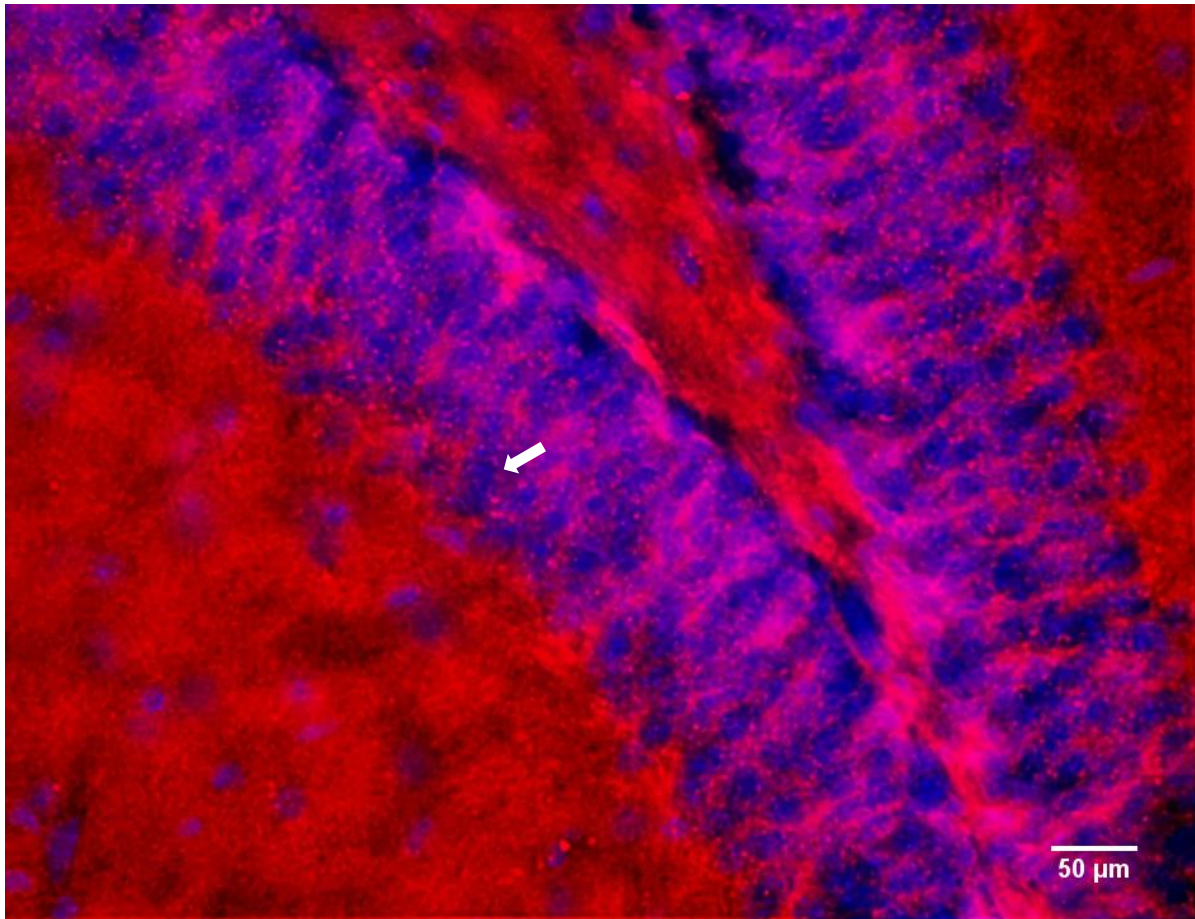


Figure 6.4: Mouse hippocampus stained with MBP aptamer 5' Biotin and Streptavidin Qdot (Red) and Hoechst 33342 (Blue). The white arrow points to a possible oligodendrocyte.

To further confirm the distribution of MBP by the stains equivalent areas were isolated from images provided by the Human Protein Atlas (HPA) [240] of anti-MBP tagged mouse brain. Figure 6.4 and Figure 6.5 A show the same relative regions of the hippocampus and have the same V-shaped distribution of nuclear staining with strands of MBP observed (green for Figure 6.5 A and red for Figure 6.4). Equivalently Figure 6.3 A & B show similar stranded MBP stain (green) encompassing nuclear stains (blue) as Figure 6.5 B. The signal of the HPA images (Figure 6.5) are generally sharper than the ones performed from our experiments due to tissue thickness related scattering [245] as they used 14 μm compared to our 30 μm . Despite this difference experimentally similar features were localised sufficiently that they could be identified for all labelled samples.

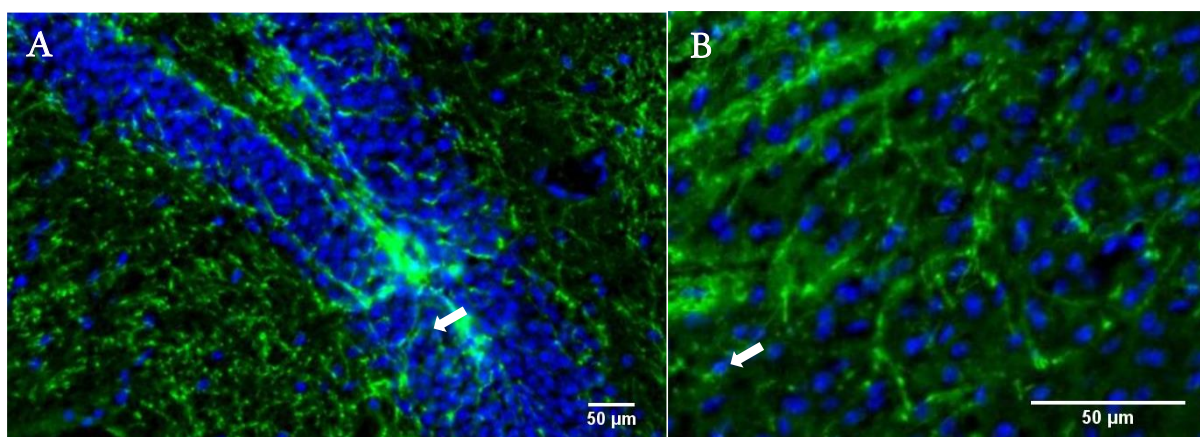


Figure 6.5: Mouse hippocampus (A) and hippocampal formation (B) stained with MBP aptamer 5' Biotin and Streptavidin FITC (Green) and Hoechst 33342 (Blue) courtesy of the Human Protein Atlas[240] The white arrows point to possible oligodendrocytes.

FM analysis demonstrated that all probes and tags were similar to literature reviewed images. Qdot aptamer staining though high in signal had staining related inconsistencies which tagged nonspecifically and was not further analysed by LA-ICP-MS. Both MBP aptamer and the MBP antibody were highly specific to MBP and showed characteristic features of MBP distribution. Elemental imaging was carried out with these probes using standard elemental tags.

6.4.4 LA-ICP-MS comparison

With confirmation of specific binding for the MBP aptamers and the MBP antibody by FM, elemental tagging was attempted. Due to the small size of MBP containing cells and the long run times of LA-ICP-MS experiments a low-resolution regime was used first where the antiMBP-¹⁵³Eu stain was used to judge general distribution of the staining by the MBP aptamers labelled via biotin 5' and thiol 5'. Once the aptamer stain matched the MBP antibody stain, a high-resolution regime was used to isolate the oligodendrocytes and myelin sheath within the sample.

The functionalisation of the MBP aptamer was an important factor for label specificity. Thiol 6' labelled aptamer trialled in Figure 6.2 B, where there was high background and a hypothesis of aptamer degradation was proposed, was confirmed by tissue staining (Figure 6.6 B) where all tissue stained with MBP aptamer thiol 5'-¹⁵³Eu had aggregates of high concentration and resembled the tagging of the antiMBP-¹⁵³Eu (Figure 6.6 C). In contrast, the MBP aptamer biotin 5'-streptavidin Eu (Figure 6.6 A) closely matched the

distribution of the antiMBP-¹⁵³Eu (Figure 6.6 C). The MBP aptamer biotin 5' streptavidin Eu was therefore chosen for high resolution mapping.

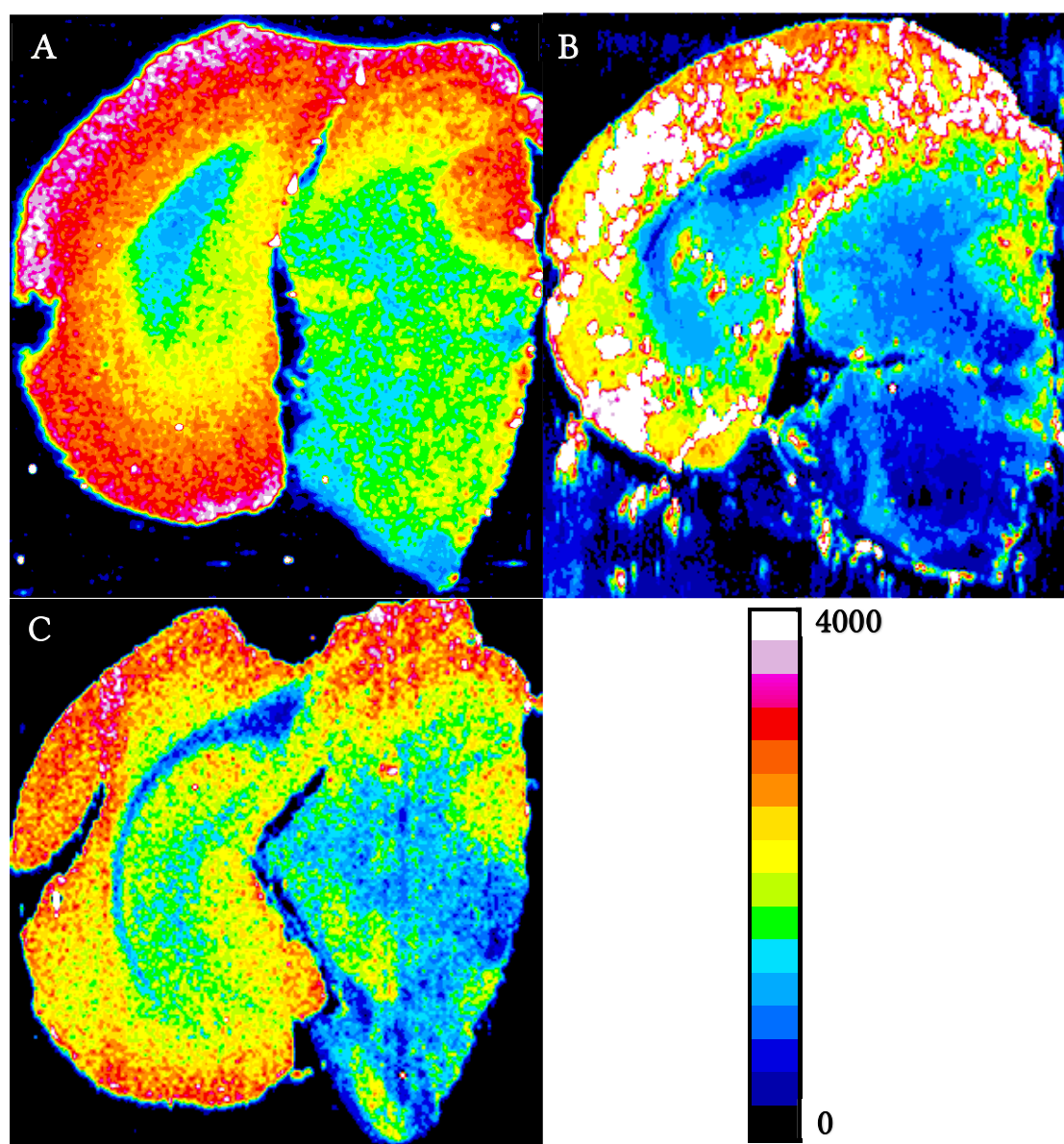


Figure 6.6: Low resolution images of MBP aptamer biotin 5'-Streptavidin Eu (A), MBP aptamer thiol 5'-¹⁵³Eu (B) and antiMBP-¹⁵³Eu (C). Calibration bar denotes ppb Eu.

Figure 6.7 A was the culmination of all the preceding confirmatory experiments to elementally image MBP using an MBP aptamer. The theoretical resolution of the high-resolution regime is 1.25 μm , but as can be seen with the comparative FM image (Figure 6.7 B) there were features which are beyond this limit of resolution for some MBP containing cells of the hippocampus. The gross distribution quite closely matched the

FM image but without an equivalent counter stain to highlight nuclei for elemental images it was difficult to fully confirm the fine structure shown.

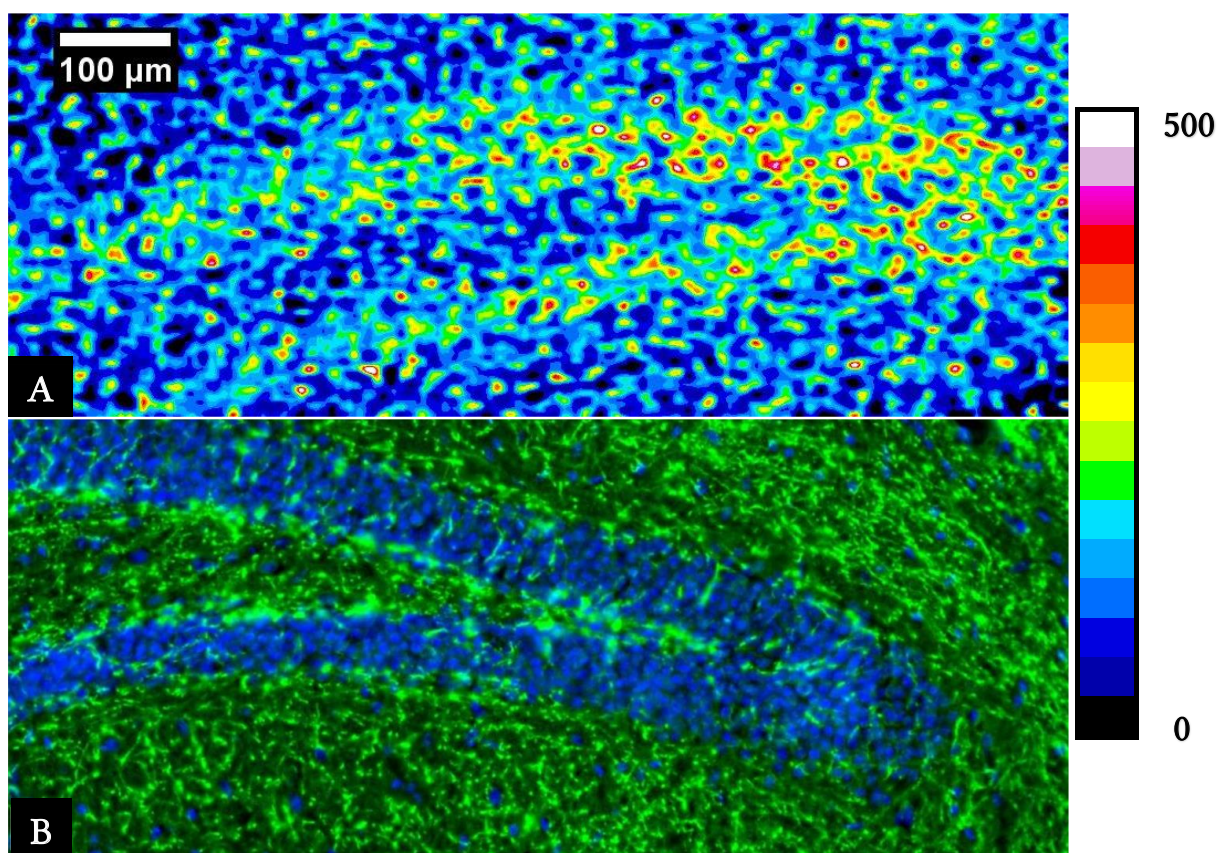


Figure 6.7: High resolution image of MBP aptamer 5'biotin-streptavidin Eu (A) and correlating antiMBP-FITC micrograph courtesy of the Human Protein Atlas [240] Calibration bar denotes ppb Eu.

The addition of the MBP aptamer as a new probe for iMSI was therefore feasible, however requires further development. Despite the biotin 5' streptavidin Eu functionalised MBP aptamer being the only successful iMSI tag, there was evidence that Qdot tagging and thiol functionalisation was worthy of further development.

6.5 Conclusion

MBP aptamers were developed as an addition to the iMSI probe toolbox. The MBP aptamers were confirmed to specifically bind MBP by colourmetric and elemental dot blots. The MBP aptamer was compared to an MBP antibody and literature images using FM for distributions in mouse brain tissue. FITC and Qdots were evaluated as tags for the aptamer with both successfully producing localised signal. Qdots were found to be

less specific in staining than the FITC stain due to protocol related issues. MBP antibodies and MBP aptamers matched literature images from the Human Protein Atlas [240]. With FM confirmation of tissue binding between the antibody and the aptamer the antibody was used as a benchmark for the elemental distribution of the aptamer. Low-resolution elemental imaging showed evidence of aptamer degradation with the thiol functionalised MBP aptamer by way of very high signal clusters. The biotin functionalised aptamer did not have this issue and matched the elemental image of the MBP antibody elemental stain. As a result high-resolution imaging was performed on tissue stained with the MBP aptamer biotin 5'-streptavidin Eu. The final image showed evidence of some cells containing MBP when compared to FM literature images from the Human Protein Atlas [240]. There was, however, features shown in the FM image that were smaller than the 1.25 μm theoretical resolution of the elemental image. Overall the use of aptamers were shown to be viable for iMSI of myelin basic protein.

7 Overall conclusions and future work

Gelatin matrix matched standards were investigated and were demonstrated to be a superior alternative to tissue produced matrix matched standards. The gelatin standards manufactured using both commercial and Teflon tape moulds were flatter and more accurate in thickness and surface roughness than matrix matched tissue standards. The analytical figures of merit were improved for the gelatin standards and limits of analysis were further reduced by an additional extraction step for metals during standard preparation employing different resins.

Super resolution reconstruction was modified for application to LA-ICP-MS imaging which improved resolution over traditional raster scanning regimes up to a theoretical limit of 1 μm , while also maintaining signal intensity. The processing steps were quantitatively invariant, and SRR was the first method that has demonstrated three-dimensional imaging of intact sections of thick tissues by LA-ICP-MS. The SRR processing was automated via MATLAB coding for both two- and three-dimensional imaging.

A protocol for elemental labelling and imaging of dystrophin in murine and human tissues was developed and shows excellent promise for a clinical diagnostic that exceeds the FDA guidelines. This pilot study demonstrated that SRR was essential to attain the required resolution for clear demarcation of muscle fibres that expressed dystrophin, and that three-dimensional SRR showed that muscle fibre dystrophin expression varied throughout the tissue, indicating that adequate sampling of various biopsies is required to fully evaluate the effects of medical interventions for muscular dystrophy.

Aptamers were compared to antibodies for iMSI and were used to image myelin basic protein and were equivalent to antibodies for iMSI based on using biotin functionalised aptamers, following by incubation with streptavidin tagged with europium. Other protocols including direct tagging of aptamers via thiol functionalisation requires further development. The feasibility of quantum dot tagging was also demonstrated and requires protocol improvement.

Future development of gelatin standards to improve routine and facile manufacture requires the development of reusable custom moulds to maximise microscope slide space, possibly by three-dimensional printing techniques. The spiking of gelatin with an internal standard would also allow isotopic dilution approaches for improved analytical figures of merit.

Super resolution reconstruction requires continued investigation of various algorithms of deconvolution for image improvement, investigation of thicker sections for three-dimensional imaging in relation to laser working distances and mitigation of laser power fluctuations with extended acquisition times. The possibility of expansion microscopy to increase resolution by swelling tissues and application of SRR-LA-ICP-MS requires investigation to further improve resolution.

The quantitative imaging of the expression of an ordered protein such as dystrophin shows the broad applicability of iMSI to further diagnostic information for muscular dystrophies. A highly multiplexed analysis of the DGC will allow the determination of the distribution of these proteins. This will result in an increased knowledge on the fundamental processes of strength and stability of muscle fibres, and potentially identify new therapeutic targets and mechanisms as changes in the expression of relevant proteins after medical interventions will may be readily observed. The application of these quantitative imaging technologies has the potential to provide unique insights and new knowledge in muscle biology and the action of novel therapeutics.

iMSI using aptamer probes requires further investigation into thiol functionalised aptamers and tagging by MaxPar protocols to minimise aptamer degradation. The development of quantum dot and other lanthanide containing fluorescent nanocrystal tagging to minimise overstaining and nonspecific binding also requires investigation. The development of aptamers for other targets and investigation to other modified aptamer types with improved features may also be pursued.

The iMSI instrumentation may also be improved by exploitation of ablation cells with faster washouts, and the development of cell devices for performing simultaneous

fluorescent microscopy and LA-ICP-MS imaging to reducing experimental acquisition time and comparisons.

8 References

- [1] C.M. Ackerman, S. Lee, C.J. Chang, Analytical Methods for Imaging Metals in Biology: From Transition Metal Metabolism to Transition Metal Signaling, *Anal. Chem.* 89 (2016) acs.analchem.6b04631. doi:10.1021/acs.analchem.6b04631.
- [2] J.W. Nieves, Bone: Maximizing bone health-magnesium, BMD and fractures., *Nat. Rev. Endocrinol.* 10 (2014) 255–6. doi:10.1038/nrendo.2014.39.
- [3] A. Flynn, The role of dietary calcium in bone health., *Proc. Nutr. Soc.* 62 (2003) 851–858. doi:10.1079/PNS2003301.
- [4] A. Halusic, S. VR, D. Shirley, J. Granjeiro, M. Costa, E. Kuchler, A. Vieira, Calcium and magnesium levels in primary tooth enamel and genetic variation in enamel formation genes, *Pediatr. Dent.* 36 (2014) 384–8.
- [5] B.S. Yu, L.H. Nie, S.Z. Yao, Ion chromatographic study of sodium, potassium and ammonium in human body fluids with bulk acoustic wave detection., *J. Chromatogr. B. Biomed. Sci. Appl.* 693 (1997) 43–49. doi:10.1016/S0378-4347(97)00019-4.
- [6] E. Raux, H.L. Schubert, M.J. Warren, Biosynthesis of cobalamin (vitamin B12): a bacterial conundrum., *Cell. Mol. Life Sci.* 57 (2000) 1880–1893. doi:10.1007/PL00000670.
- [7] A.J. Thomson, H.B. Gray, Bio-inorganic chemistry, *Curr. Opin. In Chem. Biol.* 2 (1998) 155–158. doi:10.1016/S1367-5931(98)80056-2.
- [8] R.H. Holm, P. Kennepohl, E.I. Solomon, E.I. Solomon, Structural and functional aspects of metal sites in biology, *Chem. Rev.* 96 (1996) 2239–2314. doi:10.1021/cr9500390.
- [9] D.J. Hare, P. Lei, S. Ayton, B.R. Roberts, R. Grimm, J.L. George, D.P. Bishop, A.D. Beavis, S.J. Donovan, G. McColl, I. Volitakis, C.L. Masters, P. a. Adlard, R. a. Cherny, A.I. Bush, D.I. Finkelstein, P. a. Doble, An iron–dopamine index predicts risk of parkinsonian neurodegeneration in the substantia nigra pars compacta,

- Chem. Sci. 5 (2014) 2160. doi:10.1039/c3sc53461h.
- [10] F. Molina-Holgado, R.C. Hider, A. Gaeta, R. Williams, P. Francis, Metals ions and neurodegeneration, *BioMetals*. 20 (2007) 639–654. doi:10.1007/s10534-006-9033-z.
- [11] T. Grobner, Gadolinium – a specific trigger for the development of nephrogenic fibrosing dermopathy and nephrogenic systemic fibrosis?, *Nephrol. Dial. Transplant*. 21 (2006) 1104–1108. doi:10.1093/ndt/gfk062.
- [12] R. Mamtani, P. Stern, I. Dawood, S. Cheema, Metals and Disease: A Global Primary Health Care Perspective, *J. Toxicol.* 2011 (2011) 1–11. doi:10.1155/2011/319136.
- [13] J.L. Gómez-Ariza, T. García-Barrera, F. Lorenzo, V. Bernal, M.J. Villegas, V. Oliveira, Use of mass spectrometry techniques for the characterization of metal bound to proteins (metallomics) in biological systems, *Anal. Chim. Acta*. 524 (2004) 15–22. doi:10.1016/j.aca.2004.01.061.
- [14] R. Łobiński, D. Schaumlöffel, J. Szpunar, Mass spectrometry in bioinorganic analytical chemistry, *Mass Spectrom. Rev.* 25 (2006) 255–289. doi:10.1002/mas.20069.
- [15] R.S. Houk, V.A. Fassel, G.D. Flesch, H.J. Svec, A.L. Gray, C.E. Taylor, Inductively coupled argon plasma as an ion source for mass spectrometric determination of trace elements, *Anal. Chem.* 52 (1980) 2283–2289. doi:10.1021/ac50064a012.
- [16] A. Sanz-Medel, M. Montes-Bayón, J. Bettmer, M. Luisa Fernández-Sánchez, J. Ruiz Encinar, ICP-MS for absolute quantification of proteins for heteroatom-tagged, targeted proteomics, *TrAC Trends Anal. Chem.* 40 (2012) 52–63. doi:10.1016/j.trac.2012.07.020.
- [17] D. Pröfrock, A. Prange, Inductively Coupled Plasma–Mass Spectrometry (ICP-MS) for Quantitative Analysis in Environmental and Life Sciences: A Review of Challenges, Solutions, and Trends, *Appl. Spectrosc.* 66 (2012) 843–868. doi:10.1366/12-06681.

- [18] S. Durrant, Laser ablation inductively coupled plasma mass spectrometry: achievements, problems, prospects, *J. Anal. At. Spectrom.* (1999). <http://pubs.rsc.org/en/content/articlehtml/1999/ja/a901765h> (accessed October 14, 2014).
- [19] M. Alexander, M. Smith, J. Hartman, Laser ablation inductively coupled plasma mass spectrometry, *Appl. Surf.* (1998) 255–261. <http://www.sciencedirect.com/science/article/pii/S0169433297006405> (accessed October 14, 2014).
- [20] R. Thomas, *Practical Guide to ICP-MS: A Tutorial for Beginners*, Third Edition, 2013.
- [21] B. Wu, M. Zoriy, Y. Chen, J. Becker, Imaging of nutrient elements in the leaves of *Elsholtzia splendens* by laser ablation inductively coupled plasma mass spectrometry (LA-ICP-MS), *Talanta.* 78 (2009) 132–7. doi:10.1016/j.talanta.2008.10.061.
- [22] C.C. Garcia, H. Lindner, K. Niemax, Laser ablation inductively coupled plasma mass spectrometry—current shortcomings, practical suggestions for improving performance, and experiments to guide future development, *J. Anal. At. Spectrom.* 24 (2009) 14. doi:10.1039/b813124b.
- [23] D.J. Hare, J.L. George, L. Bray, I. Volitakis, A. Vais, T.M. Ryan, R. a. Cherny, A.I. Bush, C.L. Masters, P. a. Adlard, P. a. Doble, D.I. Finkelstein, The effect of paraformaldehyde fixation and sucrose cryoprotection on metal concentration in murine neurological tissue, *J. Anal. At. Spectrom.* 29 (2014) 565. doi:10.1039/c3ja50281c.
- [24] J.S. Becker, J.S. Becker, Mass spectrometry imaging (MSI) of metals by laser ablation ICP-MS and metallomics of biomedical samples, *Biomed. Spectrosc. Imaging.* 1 (2012) 187–204. doi:10.3233/BSI-2012-0016.
- [25] S. Majumdar, J.R. Peralta-Videa, H. Castillo-Michel, J. Hong, C.M. Rico, J.L. Gardea-Torresdey, Applications of synchrotron μ -XRF to study the distribution of

- biologically important elements in different environmental matrices: a review., *Anal. Chim. Acta.* 755 (2012) 1–16. doi:10.1016/j.aca.2012.09.050.
- [26] D.S. Gholap, A. Izmer, B. De Samber, J.T. van Elteren, V.S. Selih, R. Evens, K. De Schamphelaere, C. Janssen, L. Balcaen, I. Lindemann, L. Vincze, F. Vanhaecke, Comparison of laser ablation-inductively coupled plasma-mass spectrometry and micro-X-ray fluorescence spectrometry for elemental imaging in *Daphnia magna*., *Anal. Chim. Acta.* 664 (2010) 19–26. doi:10.1016/j.aca.2010.01.052.
- [27] V.S. Smentkowski, S.L. Mcarthur, G. Mishra, C.D. Easton, *Surface analysis and techniques in biology*, Springer International Publishing, Cham, 2014. doi:10.1007/978-3-319-01360-2.
- [28] M.K. Passarelli, N. Winograd, Lipid imaging with time-of-flight secondary ion mass spectrometry (ToF-SIMS)., *Biochim. Biophys. Acta.* 1811 (2011) 976–90. doi:10.1016/j.bbalip.2011.05.007.
- [29] C.M. Ahamer, K.M. Riepl, N. Huber, J.D. Pedarnig, Femtosecond laser-induced breakdown spectroscopy: Elemental imaging of thin films with high spatial resolution, *Spectrochim. Acta - Part B At. Spectrosc.* 136 (2017) 56–65. doi:10.1016/j.sab.2017.08.005.
- [30] G. Galbács, A critical review of recent progress in analytical laser-induced breakdown spectroscopy, *Anal. Bioanal. Chem.* 407 (2015) 7537–7562. doi:10.1007/s00216-015-8855-3.
- [31] R. McRae, P. Bagchi, S. Sumalekshmy, C.J. Fahrni, In situ imaging of metals in cells and tissues, *Chem. Rev.* 109 (2009) 4780–4827. doi:10.1021/cr900223a.
- [32] A.L. Gray, Solid sample introduction by laser ablation for inductively coupled plasma source mass spectrometry, *Analyst.* 110 (1985) 551. doi:10.1039/an9851000551.
- [33] J. Koch, D. Günther, Review of the state-of-the-art of laser ablation inductively coupled plasma mass spectrometry, *Appl. Spectrosc.* 65 (2011) 155–62. doi:10.1366/11-06255.

- [34] A.B. Wolk, C.M. Leavitt, E. Garand, M.A. Johnson, Cryogenic ion chemistry and spectroscopy, *Acc. Chem. Res.* 47 (2014) 202–210. doi:10.1021/ar400125a.
- [35] L. De Broglie, Recherches sur la théorie des Quanta, *Ann. Phys. (Paris)*. 10 (1925) 22–128. doi:10.1051/anphys/192510030022.
- [36] J.S. Becker, M. Zoriy, A. Matusch, B. Wu, D. Salber, C. Palm, J.S. Becker, Bioimaging of metals by laser ablation inductively coupled plasma mass spectrometry (LA-ICP-MS), *Mass Spectrom. Rev.* (2009) n/a-n/a. doi:10.1002/mas.20239.
- [37] C. Austin, F. Fryer, J. Lear, D. Bishop, D. Hare, T. Rawling, L. Kirkup, A. McDonagh, P. Doble, Factors affecting internal standard selection for quantitative elemental bio-imaging of soft tissues by LA-ICP-MS, *J. Anal. At. Spectrom.* 26 (2011) 1494. doi:10.1039/c0ja00267d.
- [38] J. Lear, D. Hare, P. Adlard, D. Finkelstein, P. Doble, Improving acquisition times of elemental bio-imaging for quadrupole-based LA-ICP-MS, *J. Anal. At. Spectrom.* 27 (2012) 159. doi:10.1039/c1ja10301f.
- [39] M. Shannon, X. Mao, A. Fernandez, Laser ablation mass removal versus incident power density during solid sampling for inductively coupled plasma atomic emission spectroscopy, *Anal.* (1995) 4522–4529. <http://pubs.acs.org/doi/abs/10.1021/ac00120a015> (accessed October 14, 2014).
- [40] A.C. Ciocan, X.L. Mao, O. Borisov, R.E. Russo, Optical emission spectroscopy studies of the influence of laser ablated mass on dry inductively coupled plasma conditions, *Spectrochim. Acta Part B* 53 (1998) 463–470. doi:10.1016/S0584-8547(97)00130-4.
- [41] J.S. Becker, A. Matusch, B. Wu, Bioimaging mass spectrometry of trace elements - recent advance and applications of LA-ICP-MS: A review., *Anal. Chim. Acta.* 835 (2014) 1–18. doi:10.1016/j.aca.2014.04.048.
- [42] D. Günther, C. A. Heinrich, Comparison of the ablation behaviour of 266 nm Nd:YAG and 193 nm ArF excimer lasers for LA-ICP-MS analysis, *J. Anal. At.*

- Spectrom. 14 (1999) 1369–1374. doi:10.1039/A901649J.
- [43] M.E. Shaheen, J.E. Gagnon, B.J. Fryer, Femtosecond (fs) lasers coupled with modern ICP-MS instruments provide new and improved potential for in situ elemental and isotopic analyses in the, *Chem. Geol.* 330–331 (2012) 260–273. doi:10.1016/j.chemgeo.2012.09.016.
- [44] B. Fernández, F. Claverie, Direct analysis of solid samples by fs-LA-ICP-MS, *TrAC Trends* 26 (2007). doi:10.1016/j.trac.2007.08.008.
- [45] S.J.M. Van Malderen, A.J. Managh, B.L. Sharp, F. Vanhaecke, Recent developments in the design of rapid response cells for laser ablation-inductively coupled plasma-mass spectrometry and their impact on bioimaging applications, *J. Anal. At. Spectrom.* 31 (2016) 423–439. doi:10.1039/C5JA00430F.
- [46] D. Hare, C. Austin, P. Doble, Quantification strategies for elemental imaging of biological samples using laser ablation-inductively coupled plasma-mass spectrometry., *Analyst.* 137 (2012) 1527–37. doi:10.1039/c2an15792f.
- [47] M.A.G. Nunes, M. Voss, G. Corazza, E.M.M. Flores, V.L. Dressler, External calibration strategy for trace element quantification in botanical samples by LA-ICP-MS using filter paper, *Anal. Chim. Acta.* 905 (2016) 51–57. doi:10.1016/j.aca.2015.11.049.
- [48] D. Clases, R. Gonzalez de Vega, P.A. Adlard, P. Doble, On-line reverse isotope dilution analysis for spatial quantification of elemental labels used in immunohistochemical assisted imaging mass spectrometry by LA-ICP-MS, *J. Anal. At. Spectrom.* (2018). doi:10.1039/C8JA00324F.
- [49] D.N. Douglas, J. O'Reilly, C. O'Connor, B.L. Sharp, H. Goenaga-Infante, Quantitation of the Fe spatial distribution in biological tissue by online double isotope dilution analysis with LA-ICP-MS: A strategy for estimating measurement uncertainty, *J. Anal. At. Spectrom.* 31 (2016) 270–279. doi:10.1039/c5ja00351b.
- [50] I. Moraleja, M.L. Mena, A. Lázaro, B. Neumann, A. Tejedor, N. Jakubowski, M.M. Gómez-Gómez, D. Esteban-Fernández, An approach for quantification of

- platinum distribution in tissues by LA-ICP-MS imaging using isotope dilution analysis, *Talanta*. 178 (2018) 166–171. doi:10.1016/j.talanta.2017.09.031.
- [51] J. O'Reilly, D. Douglas, J. Braybrook, P.-W. So, E. Vergucht, J. Garrevoet, B. Vekemans, L. Vincze, H. Goenaga-Infante, A novel calibration strategy for the quantitative imaging of iron in biological tissues by LA-ICP-MS using matrix-matched standards and internal standardisation, *J. Anal. At. Spectrom.* 29 (2014) 1378. doi:10.1039/C4JA00002A.
- [52] D.J. Hare, J. Lear, D. Bishop, A. Beavis, P. a. Doble, Protocol for production of matrix-matched brain tissue standards for imaging by laser ablation-inductively coupled plasma-mass spectrometry, *Anal. Methods*. 5 (2013) 1915. doi:10.1039/c3ay26248k.
- [53] M. Bonta, H. Lohninger, Application of gold thin-films for internal standardization in LA-ICP-MS imaging experiments, *Analyst*. 139 (2014) 1521–31. doi:10.1039/c3an01511d.
- [54] S. Hoesl, B. Neumann, S. Techritz, G. Sauter, R. Simon, H. Schlüter, M.W. Linscheid, F. Theuring, N. Jakubowski, L. Mueller, M. W. Linscheid, F. Theuring, N. Jakubowski, L. Mueller, Internal standardization of LA-ICP-MS immuno imaging via printing of universal metal spiked inks onto tissue sections, *J. Anal. At. Spectrom.* 31 (2016) 801–808. doi:10.1039/c5ja00409h.
- [55] A. Kindness, C.N. Sekaran, J. Feldmann, Two-Dimensional Mapping of Copper and Zinc in Liver Sections by Laser Ablation–Inductively Coupled Plasma Mass Spectrometry, *Clin. Chem.* 49 (2003) 1916–1923. doi:10.1373/clinchem.2003.022046.
- [56] Y. Liu, Z. Hu, S. Gao, D. Gunther, J. Xu, C. Gao, H. Chen, In situ analysis of major and trace elements of anhydrous minerals by LA-ICP-MS without applying an internal standard, *Chem. Geol.* 257 (2008) 34–43. doi:10.1016/j.chemgeo.2008.08.004.
- [57] L. Cuadros-Rodríguez, M.G. Bagur-González, M. Sánchez-Viñas, A. González-

- Casado, A.M. Gómez-Sáez, Principles of analytical calibration/quantification for the separation sciences., *J. Chromatogr. A.* 1158 (2007) 33–46. doi:10.1016/j.chroma.2007.03.030.
- [58] C. Austin, D. Hare, T. Rawling, A.M. McDonagh, P. Doble, Quantification method for elemental bio-imaging by LA-ICP-MS using metal spiked PMMA films, *J. Anal. At. Spectrom.* 25 (2010) 722. doi:10.1039/b911316a.
- [59] H.-J. Stärk, R. Wennrich, A new approach for calibration of laser ablation inductively coupled plasma mass spectrometry using thin layers of spiked agarose gels as references., *Anal. Bioanal. Chem.* 399 (2011) 2211–7. doi:10.1007/s00216-010-4413-1.
- [60] I. Konz, B. Fernández, M. Fernández, Gold internal standard correction for elemental imaging of soft tissue sections by LA-ICP-MS: element distribution in eye microstructures, *Anal.* 405 (2013) 3091–6. doi:10.1007/s00216-013-6778-4.
- [61] K. Loehr, H. Traub, A.J. Wanka, U. Panne, N. Jakubowski, Quantification of metals in single cells by LA-ICP-MS: Comparison of single spot ablation and imaging, *J. Anal. At. Spectrom.* (2018). doi:10.1039/C8JA00191J.
- [62] K. Halbach, S. Wagner, S. Scholz, T. Luckenbach, T. Reemtsma, Elemental imaging (LA-ICP-MS) of zebrafish embryos to study the toxicokinetics of the acetylcholinesterase inhibitor naled, *Anal. Bioanal. Chem.* (2018). doi:10.1007/s00216-018-1471-2.
- [63] C.M. Ackerman, P.K. Weber, T. Xiao, B. Thai, T.J. Kuo, E. Zhang, J. Pett-Ridge, C.J. Chang, Multimodal LA-ICP-MS and nanoSIMS imaging enables copper mapping within photoreceptor megamitochondria in a zebrafish model of Menkes disease, *Metallomics.* 10 (2018) 474–485. doi:10.1039/c7mt00349h.
- [64] J.C. Müller, J. Lichtmanegger, H. Zischka, M. Sperling, U. Karst, High spatial resolution LA-ICP-MS demonstrates massive liver copper depletion in Wilson disease rats upon Methanobactin treatment, *J. Trace Elem. Med. Biol.* 49 (2018) 119–127. doi:10.1016/j.jtemb.2018.05.009.

- [65] M.H.M. Klose, S. Theiner, C. Kornauth, S.M. Meier-Menches, P. Heffeter, W. Berger, G. Koellensperger, B.K. Keppler, Bioimaging of isosteric osmium and ruthenium anticancer agents by LA-ICP-MS, *Metallomics*. (2018). doi:10.1039/C8MT00012C.
- [66] D. Clases, S. Fingerhut, A. Jeibmann, M. Sperling, P. Doble, U. Karst, LA-ICP-QQQ-MS improves limits of detection in elemental bioimaging of gadolinium deposition originating from MRI contrast agents in skin and brain tissues, *J. Trace Elem. Med. Biol.* 51 (2018) 1–21. doi:10.1016/j.jtemb.2018.10.021.
- [67] D.P. Bishop, M. Grossgarten, D. Dietrich, A. Vennemann, N. Cole, M. Sperling, M. Wiemann, P.A. Doble, U. Karst, Quantitative imaging of translocated silver following nanoparticle exposure by laser ablation-inductively coupled plasma-mass spectrometry, *Anal. Methods*. 10 (2018) 836–840. doi:10.1039/C7AY02294H.
- [68] M. Cruz-Alonso, B. Fernandez, L. Álvarez, H. González-Iglesias, H. Traub, N. Jakubowski, R. Pereiro, Bioimaging of metallothioneins in ocular tissue sections by laser ablation-ICP-MS using bioconjugated gold nanoclusters as specific tags, *Microchim. Acta*. 185 (2018) 64. doi:10.1007/s00604-017-2597-1.
- [69] S.J.M. Van Malderen, T. Van Acker, B. Laforce, M. De Bruyne, R. de Rycke, T. Asaoka, L. Vincze, F. Vanhaecke, Three-dimensional reconstruction of the distribution of elemental tags in single cells using laser ablation ICP-mass spectrometry via registration approaches, *Anal. Bioanal. Chem.* (2019). doi:10.1007/s00216-019-01677-6.
- [70] R.W. Hutchinson, A.G. Cox, C.W. McLeod, P.S. Marshall, A. Harper, E.L. Dawson, D.R. Howlett, Imaging and spatial distribution of β -amyloid peptide and metal ions in Alzheimer's plaques by laser ablation-inductively coupled plasma-mass spectrometry, *Anal. Biochem.* 346 (2005) 225–233. doi:10.1109/ISTAS.1998.688150.
- [71] D.J. Hare, P. a Adlard, P. a Doble, D.I. Finkelstein, Metallobiology of 1-methyl-4-phenyl-1,2,3,6-tetrahydropyridine neurotoxicity., *Metallomics*. 5 (2013) 91–109.

- doi:10.1039/c2mt20164j.
- [72] D.P. Bishop, N. Cole, T. Zhang, P.A. Doble, D.J. Hare, A guide to integrating immunohistochemistry and chemical imaging, *Chem. Soc. Rev.* (2018). doi:10.1039/C7CS00610A.
- [73] E. a Lerner, M.R. Lerner, C. a Janeway, J. a Steitz, Monoclonal antibodies to nucleic acid-containing cellular constituents: probes for molecular biology and autoimmune disease., *Proc. Natl. Acad. Sci. U. S. A.* 78 (1981) 2737–2741. doi:10.1073/pnas.78.5.2737.
- [74] M. a Helsby, P.M. Leader, J.R. Fenn, T. Gulsen, C. Bryant, G. Doughton, B. Sharpe, P. Whitley, C.J. Caunt, K. James, A.D. Pope, D.H. Kelly, A.D. Chalmers, CiteAb: a searchable antibody database that ranks antibodies by the number of times they have been cited., *BMC Cell Biol.* 15 (2014) 6. doi:10.1186/1471-2121-15-6.
- [75] S.Q. Li, F. Li, Y. Xiao, C.M. Wang, L. Tuo, J. Hu, X. Bin Yang, J.S. Wang, W.H. Shi, X. Li, X.F. Cao, Comparison of long non-coding RNAs, microRNAs and messenger RNAs involved in initiation and progression of esophageal squamous cell carcinoma, *Mol. Med. Rep.* 10 (2014) 652–662. doi:10.3892/mmr.2014.2287.
- [76] B. Schöbitz, E.R. de Kloet, W. Sutanto, F. Holsboer, Cellular localization of interleukin 6 mRNA and interleukin 6 receptor mRNA in rat brain., *Eur. J. Neurosci.* 5 (1993) 1426–1435.
- [77] E. Bertrand, P. Chartrand, M. Schaefer, S.M. Shenoy, R.H. Singer, R.M. Long, Localization of ASH1 mRNA particles in living yeast., *Mol. Cell.* 2 (1998) 437–445. doi:10.1016/S1097-2765(00)80143-4.
- [78] B. Wlotzka, S. Leva, B. Eschgfäller, J. Burmeister, F. Kleinjung, C. Kaduk, P. Muhn, H. Hess-Stumpp, S. Klussmann, In vivo properties of an anti-GnRH Spiegelmer: an example of an oligonucleotide-based therapeutic substance class., *Proc. Natl. Acad. Sci. U. S. A.* 99 (2002) 8898–8902. doi:10.1073/pnas.132067399.
- [79] S. Vaddypally, C. Xu, S. Zhao, Y. Fan, C.E. Schafmeister, M.J. Zdilla, Architectural spiroligomers designed for binuclear metal complex templating, *Inorg. Chem.* 52

- (2013) 6457–6463. doi:10.1021/ic4003498.
- [80] Z.Z. Brown, K. Akula, A. Arzumanyan, J. Alleva, M. Jackson, E. Bichenkov, J.B. Sheffield, M. a. Feitelson, C.E. Schafmeister, A Spiroligomer α -Helix Mimic That Binds HDM2, Penetrates Human Cells and Stabilizes HDM2 in Cell Culture, *PLoS One*. 7 (2012) e45948. doi:10.1371/journal.pone.0045948.
- [81] S. Tombelli, M. Minunni, M. Mascini, Analytical applications of aptamers, *Biosens. Bioelectron.* 20 (2005) 2424–2434. doi:10.1016/j.bios.2004.11.006.
- [82] U. Schlecht, a. Malavé, T. Gronewold, M. Tewes, M. Löhndorf, Comparison of antibody and aptamer receptors for the specific detection of thrombin with a nanometer gap-sized impedance biosensor, *Anal. Chim. Acta.* 573–574 (2006) 65–68. doi:10.1016/j.aca.2006.01.016.
- [83] Y. Pu, Z. Liu, Y. Lu, P. Yuan, J. Liu, B. Yu, G. Wang, C.J. Yang, H. Liu, W. Tan, Using DNA Aptamer Probe for Immunostaining of Cancer Frozen Tissues, *Anal. Chem.* 87 (2015) 1919–1924. doi:10.1021/ac504175h.
- [84] R. Stoltenburg, C. Reinemann, B. Strehlitz, SELEX-A (r)evolutionary method to generate high-affinity nucleic acid ligands, *Biomol. Eng.* 24 (2007) 381–403. doi:10.1016/j.bioeng.2007.06.001.
- [85] D. Peer, J.M. Karp, S. Hong, O.C. Farokhzad, R. Margalit, R. Langer, Nanocarriers as an emerging platform for cancer therapy., *Nat. Nanotechnol.* 2 (2007) 751–760. doi:10.1038/nnano.2007.387.
- [86] I.B. Buchwalow, E. a. Minin, W. Boecker, A multicolor fluorescence immunostaining technique for simultaneous antigen targeting, *Acta Histochem.* 107 (2005) 143–148. doi:10.1016/j.acthis.2005.01.003.
- [87] P. Taupin, BrdU immunohistochemistry for studying adult neurogenesis: Paradigms, pitfalls, limitations, and validation, *Brain Res. Rev.* 53 (2007) 198–214. doi:10.1016/j.brainresrev.2006.08.002.
- [88] Thermo Fisher Scientific Inc., Immunolabeling, (2015).

<https://www.thermofisher.com/au/en/home/life-science/cell-analysis/cell-analysis-learning-center/molecular-probes-school-of-fluorescence/labeling-your-samples/immunolabeling.html>.

- [89] E. Coons, A; Creech, H; Jones, N; Berliner, The demonstration of pneumococcal antigens in tissues, *J. Immunol.* 45 (1942) 159–170.
- [90] N.C. Veitch, Horseradish peroxidase: A modern view of a classic enzyme, *Phytochemistry.* 65 (2004) 249–259. doi:10.1016/j.phytochem.2003.10.022.
- [91] D. Li, Y. Ying, J. Wu, R. Niessner, D. Knopp, Comparison of monomeric and polymeric horseradish peroxidase as labels in competitive ELISA for small molecule detection, *Microchim. Acta.* 180 (2013) 711–717. doi:10.1007/s00604-013-0974-y.
- [92] N.C. Shaner, R.E. Campbell, P. a Steinbach, B.N.G. Giepmans, A.E. Palmer, R.Y. Tsien, Improved monomeric red, orange and yellow fluorescent proteins derived from *Discosoma* sp. red fluorescent protein., *Nat. Biotechnol.* 22 (2004) 1567–1572. doi:10.1038/nbt1037.
- [93] J.S. Paige, K.Y. Wu, S.R. Jaffrey, RNA mimics of green fluorescent protein., *Science.* 333 (2011) 642–646. doi:10.1126/science.1207339.
- [94] B.N.G. Giepmans, S.R. Adams, M.H. Ellisman, R.Y. Tsien, The fluorescent toolbox for assessing protein location and function., *Science.* 312 (2006) 217–224. doi:10.1126/science.1124618.
- [95] M.R. Lewis, R. Kannan, Development and applications of radioactive nanoparticles for imaging of biological systems, *Wiley Interdiscip. Rev. Nanomedicine Nanobiotechnology.* 6 (2014) 628–640. doi:10.1002/wnan.1292.
- [96] B. Xu, C. Zhao, W. Wei, J. Ren, D. Miyoshi, N. Sugimoto, X. Qu, Aptamer carbon nanodot sandwich used for fluorescent detection of protein, *Analyst.* 137 (2012) 5483. doi:10.1039/c2an36174d.
- [97] J. Yuan, S. Wu, N. Duan, X. Ma, Y. Xia, J. Chen, Z. Ding, Z. Wang, A sensitive

- gold nanoparticle-based colorimetric aptasensor for *Staphylococcus aureus*, *Talanta*. 127 (2014) 163–168. doi:10.1016/j.talanta.2014.04.013.
- [98] Y.-P. Ho, K.W. Leong, Quantum dot-based theranostics., *Nanoscale*. 2 (2010) 60–68. doi:10.1039/b9nr00178f.
- [99] P. Zrazhevskiy, M. Sena, X. Gao, Designing multifunctional quantum dots for bioimaging, detection, and drug delivery., *Chem. Soc. Rev.* 39 (2010) 4326–4354. doi:10.1039/b915139g.
- [100] H. Hong, F. Chen, W. Cai, Pharmacokinetic Issues of Imaging with Nanoparticles: Focusing on Carbon Nanotubes and Quantum Dots, *Mol. Imaging Biol.* 15 (2013) 507–520. doi:10.1007/s11307-013-0648-5.
- [101] E.C. Cho, Q. Zhang, Y. Xia, The effect of sedimentation and diffusion on cellular uptake of gold nanoparticles., *Nat. Nanotechnol.* 6 (2011) 385–391. doi:10.1038/nnano.2011.58.
- [102] L. Sun, Y. Wang, C.-H. Yan, Paradigms and Challenges for Bioapplication of Rare Earth Upconversion Luminescent Nanoparticles: Small Size and Tunable Emission/Excitation Spectra, *Acc. Chem. Res.* (2014). doi:10.1021/ar400218t.
- [103] I. Konz, B. Fernández, M.L. Fernández, R. Pereiro, H. González-Iglesias, M. Coca-Prados, A. Sanz-Medel, Quantitative bioimaging of trace elements in the human lens by LA-ICP-MS, *Anal. Bioanal. Chem.* 406 (2014) 2343–2348. doi:10.1007/s00216-014-7617-y.
- [104] Protocol, MAXPAR® Antibody Labeling Kit, (2012) 4–6.
- [105] J. Bettmer, N. Jakubowski, a. Prange, Elemental tagging in inorganic mass spectrometric bioanalysis, *Anal. Bioanal. Chem.* 386 (2006) 7–11. doi:10.1007/s00216-006-0557-4.
- [106] F. Pinaud, X. Michalet, L. a. Bentolila, J.M. Tsay, S. Doose, J.J. Li, G. Iyer, S. Weiss, Advances in fluorescence imaging with quantum dot bio-probes, *Biomaterials*. 27 (2006) 1679–1687. doi:10.1016/j.biomaterials.2005.11.018.

- [107] C. Hu, G. Popescu, Quantitative Phase Imaging (QPI) in Neuroscience, *IEEE J. Sel. Top. Quantum Electron.* 25 (2018) 1–9. doi:10.1109/JSTQE.2018.2869613.
- [108] A.L. Alexander, J.E. Lee, M. Lazar, A.S. Field, Diffusion tensor imaging of the brain., *Neurotherapeutics.* 4 (2007) 316–29. doi:10.1016/j.nurt.2007.05.011.
- [109] N. McGowan, A.M. Fowler, K. Parkinson, D.P. Bishop, K. Ganio, P. a Doble, D.J. Booth, D.J. Hare, Beyond the transect: an alternative microchemical imaging method for fine scale analysis of trace elements in fish otoliths during early life., *Sci. Total Environ.* 494–495 (2014) 177–86. doi:10.1016/j.scitotenv.2014.05.115.
- [110] H. Takeda, S. Farsiu, J. Christou, P. Milanfar, Super-Drizzle : Applications of Adaptive Kernel Regression in Astronomical Imaging, in: *Adv. Maui Opt. Sp. Surveill. Technol. Conf.*, 2006.
- [111] A.S. Fruchter, R.N. Hook, Drizzle: A Method for the Linear Reconstruction of Undersampled Images, *Publ. Astron. Soc. Pacific.* 114 (2002) 144–152. doi:10.1086/338393.
- [112] T. Ha, P. Tinnefeld, Photophysics of Fluorescent Probes for Single-Molecule Biophysics and Super-Resolution Imaging, *Annu. Rev. Phys. Chem.* 63 (2012) 595–617. doi:10.1146/annurev-physchem-032210-103340.
- [113] O. Dzyubachyk, Q. Tao, D.H.J.J. Poot, H.J. Lamb, K. Zeppenfeld, B.P.F.F. Lelieveldt, R.J. van der Geest, Super-resolution reconstruction of late gadolinium-enhanced MRI for improved myocardial scar assessment., *J. Magn. Reson. Imaging.* 42 (2015) 160–7. doi:10.1002/jmri.24759.
- [114] A.G. York, P. Chandris, D.D. Nogare, J. Head, P. Wawrzusin, R.S. Fischer, A. Chitnis, H. Shroff, Instant super-resolution imaging in live cells and embryos via analog image processing., *Nat. Methods.* 10 (2013) 1122–6. doi:10.1038/nmeth.2687.
- [115] V.H. Patil, D.S. Bormane, Interpolation for Super Resolution Imaging, in: *Innov. Adv. Tech. Comput. Inf. Sci. Eng.*, Springer Netherlands, Dordrecht, 2007: pp. 483–489. doi:10.1007/978-1-4020-6268-1_85.

- [116] F. Tang, Y. Bi, J. He, T. Li, Z. Abliz, X. Wang, Application of super-resolution reconstruction of sparse representation in mass spectrometry imaging, *Rapid Commun. Mass Spectrom.* 29 (2015) 1178–1184. doi:10.1002/rcm.7205.
- [117] A.J. Herrmann, S. Techritz, N. Jakubowski, A. Haase, A. Luch, U. Panne, L. Mueller, A simple metal staining procedure for identification and visualization of single cells by LA-ICP-MS, *Analyst.* (2017). doi:10.1039/C6AN02638A.
- [118] D. Drescher, C. Giesen, H. Traub, U. Panne, J. Kneipp, N. Jakubowski, Quantitative imaging of gold and silver nanoparticles in single eukaryotic cells by laser ablation ICP-MS, *Anal. Chem.* 84 (2012) 9684–9688. doi:10.1021/ac302639c.
- [119] L. Mueller, H. Traub, N. Jakubowski, D. Drescher, V.I. Baranov, J. Kneipp, Trends in single-cell analysis by use of ICP-MS, *Anal. Bioanal. Chem.* 406 (2014) 6963–6977. doi:10.1007/s00216-014-8143-7.
- [120] S. Theiner, E. Schreiber-Brynzak, M.A. Jakupec, M. Galanski, G. Koellensperger, B.K. Keppler, LA-ICP-MS imaging in multicellular tumor spheroids – a novel tool in the preclinical development of metal-based anticancer drugs, *Metallomics.* 8 (2016) 398–402. doi:10.1039/C5MT00276A.
- [121] A.-C. Niehoff, J. Grünebaum, A. Moosmann, D. Mulac, J. Söbbing, R. Niehaus, R. Buchholz, S. Kröger, A. Wiehe, S. Wagner, M. Sperling, H. von Briesen, K. Langer, U. Karst, Quantitative bioimaging of platinum group elements in tumor spheroids, *Anal. Chim. Acta.* 938 (2016) 106–113. doi:10.1016/j.aca.2016.07.021.
- [122] B. Scherrer, A. Gholipour, S.K. Warfield, Super-resolution reconstruction to increase the spatial resolution of diffusion weighted images from orthogonal anisotropic acquisitions, *Med. Image Anal.* 16 (2012) 1465–1476. doi:10.1016/j.media.2012.05.003.
- [123] New wave research, NWR193 ultracompact, (n.d.). http://www.atl-laser.de/downloads/NWR193_Brochure.pdf.
- [124] I. Agilent Technologies, Make the Change to ICP-MS with Agilent, 2008.

- [125] Thermo Fisher Scientific, NanoDrop 2000 / 2000c Spectrophotometer User Manual V1.0, (2009) 97. <https://assets.thermofisher.com/TFS-Assets/CAD/manuals/NanoDrop-2000-User-Manual-EN.pdf>.
- [126] F.E. Grubbs, Sample Criteria for Testing Outlying Observations, *Ann. Math. Stat.* 21 (1950) 27–58. doi:10.1214/aoms/1177729885.
- [127] S. Wang, R. Brown, D.J. Gray, Application of Laser Ablation-ICPMS to the Spatially Resolved Micro-Analysis of Biological Tissue, *Appl. Spectrosc.* 48 (1994) 1321–1325. doi:10.1366/0003702944028001.
- [128] J. Seuma, J. Bunch, A. Cox, C. McLeod, J. Bell, C. Murray, Combination of immunohistochemistry and laser ablation ICP mass spectrometry for imaging of cancer biomarkers, *Proteomics.* 8 (2008) 3775–3784. doi:10.1002/pmic.200800167.
- [129] R. González de Vega, D. Clases, M.L. Fernández-Sánchez, N. Eiró, L.O. González, F.J. Vizoso, P.A. Doble, A. Sanz-Medel, MMP-11 as a biomarker for metastatic breast cancer by immunohistochemical-assisted imaging mass spectrometry, *Anal. Bioanal. Chem.* 411 (2019) 639–646. doi:10.1007/s00216-018-1365-3.
- [130] D. Günther, B. Hattendorf, Solid sample analysis using laser ablation inductively coupled plasma mass spectrometry, *TrAC Trends Anal. Chem.* 24 (2005) 255–265. doi:10.1016/j.trac.2004.11.017.
- [131] B. Fernández, P. Rodríguez-González, J.I. García Alonso, J. Malherbe, S. García-Fonseca, R. Pereiro, A. Sanz-Medel, On-line double isotope dilution laser ablation inductively coupled plasma mass spectrometry for the quantitative analysis of solid materials, *Anal. Chim. Acta.* 851 (2014) 64–71. doi:10.1016/j.aca.2014.08.017.
- [132] D. Clases, R. Gonzalez de Vega, P.A. Adlard, P.A. Doble, On-line reverse isotope dilution analysis for spatial quantification of elemental labels used in immunohistochemical assisted imaging mass spectrometry via LA-ICP-MS, *J. Anal. At. Spectrom.* 34 (2019) 407–412. doi:10.1039/C8JA00324F.
- [133] A. Limbeck, P. Galler, M. Bonta, G. Bauer, W. Nischkauer, F. Vanhaecke, Recent advances in quantitative LA-ICP-MS analysis: challenges and solutions in the life

- sciences and environmental chemistry, *Anal. Bioanal. Chem.* (2015) 6593–6617. doi:10.1007/s00216-015-8858-0.
- [134] D. Hare, C. Austin, P. Doble, M. Arora, Elemental bio-imaging of trace elements in teeth using laser ablation-inductively coupled plasma-mass spectrometry., *J. Dent.* 39 (2011) 397–403. doi:10.1016/j.jdent.2011.03.004.
- [135] R. González de Vega, M.L. Fernández-Sánchez, J. Pisonero, N. Eiró, F.J. Vizoso, A. Sanz-Medel, Quantitative bioimaging of Ca, Fe, Cu and Zn in breast cancer tissues by LA-ICP-MS, *J. Anal. At. Spectrom.* 32 (2017) 671–677. doi:10.1039/C6JA00390G.
- [136] R. Niehaus, M. Sperling, U. Karst, Study on aerosol characteristics and fractionation effects of organic standard materials for bioimaging by means of LA-ICP-MS, *J. Anal. At. Spectrom.* 30 (2015) 2056–2065. doi:10.1039/C5JA00221D.
- [137] D.J. Hare, E.P. Raven, B.R. Roberts, M. Bogeski, S.D. Portbury, C.A. McLean, C.L. Masters, J.R. Connor, A.I. Bush, P.J. Crouch, P.A. Doble, Laser ablation-inductively coupled plasma-mass spectrometry imaging of white and gray matter iron distribution in Alzheimer’s disease frontal cortex, *Neuroimage.* 137 (2016) 124–131. doi:10.1016/j.neuroimage.2016.05.057.
- [138] S. Rodríguez-Menéndez, B. Fernández, M. García, L. Álvarez, M. Luisa Fernández, A. Sanz-Medel, M. Coca-Prados, R. Pereiro, H. González-Iglesias, Quantitative Study of Zinc and Metallothioneins in the Human Retina and Rpe Cells By Mass Spectrometry-Based Methodologies, *Talanta.* 178 (2017) 222–230. doi:10.1016/j.talanta.2017.09.024.
- [139] H. González-Iglesias, C. Petrash, S. Rodríguez-Menéndez, M. García, L. Álvarez, L. Fernández-Vega Cueto, B. Fernández, R. Pereiro, A. Sanz-Medel, M. Coca-Prados, Quantitative distribution of Zn, Fe and Cu in the human lens and study of the Zn–metallothionein redox system in cultured lens epithelial cells by elemental MS, *J. Anal. At. Spectrom.* 32 (2017) 1746–1756. doi:10.1039/C6JA00431H.
- [140] O. Reifschneider, C.A. Wehe, K. Diebold, C. Becker, M. Sperling, U. Karst,

- Elemental bioimaging of haematoxylin and eosin-stained tissues by laser ablation ICP-MS, *J. Anal. At. Spectrom.* 28 (2013) 989–993. doi:10.1039/c3ja50046b.
- [141] O. Hachmöller, M. Aichler, K. Schwamborn, L. Lutz, M. Werner, M. Sperling, A. Walch, U. Karst, Element bioimaging of liver needle biopsy specimens from patients with Wilson's disease by laser ablation-inductively coupled plasma-mass spectrometry, *J. Trace Elem. Med. Biol.* 35 (2016) 97–102. doi:10.1016/j.jtemb.2016.02.001.
- [142] P. M-M, U. Merle, R. Weiskirchen, J.S. Becker, Bioimaging of copper deposition in Wilson's diseases mouse liver by laser ablation inductively coupled plasma mass spectrometry imaging (LA-ICP-MSI), *Int. J. Mass Spectrom.* 354–355 (2013) 281–287. doi:10.1016/j.ijms.2013.07.006.
- [143] M. Arora, D. Hare, C. Austin, D.R. Smith, P. Doble, Spatial distribution of manganese in enamel and coronal dentine of human primary teeth., *Sci. Total Environ.* 409 (2011) 1315–9. doi:10.1016/j.scitotenv.2010.12.018.
- [144] K.-A. Dorph-Petersen, J.R. Nyengaard, H.J.G. Gundersen, Tissue shrinkage and unbiased stereological estimation of particle number and size, *J. Microsc.* 204 (2001) 232–246. doi:10.1046/j.1365-2818.2001.00958.x.
- [145] M. Šala, V.S. Šelih, J. van Elteren, Gelatin gels as multi-element calibration standards in LA-ICP-MS bioimaging: fabrication of homogeneous standards and micro-homogeneity testing, *Analyst.* (2017). doi:10.1039/C7AN01361B.
- [146] H. Sela, Z. Karpas, H. Cohen, Y. Zakon, Y. Zeiri, Preparation of stable standards of biological tissues for laser ablation analysis, *Int. J. Mass Spectrom.* 307 (2011) 142–148. doi:10.1016/j.ijms.2011.01.022.
- [147] D. Gholap, J. Verhulst, W. Ceelen, F. Vanhaecke, Use of pneumatic nebulization and laser ablation-inductively coupled plasma-mass spectrometry to study the distribution and bioavailability of an intraperitoneally administered Pt-containing chemotherapeutic drug, *Anal. Bioanal. Chem.* 402 (2012) 2121–2129. doi:10.1007/s00216-011-5654-3.

- [148] M. Birka, K.S. Wentker, E. Lusmöller, B. Arheilger, C.A. Wehe, M. Sperling, R. Stadler, U. Karst, Diagnosis of Nephrogenic Systemic Fibrosis by means of Elemental Bioimaging and Speciation Analysis, *Anal. Chem.* 87 (2015) 3321–3328. doi:10.1021/ac504488k.
- [149] N.M.R.S. Andr, G. Pardo, P.A. Doble, G.L.G. Miklos, Distributions of manganese in diverse human cancers provide insights into tumour radioresistance, *Metallomics.* (2018) 2–3. doi:10.1039/C8MT00110C.
- [150] S.D. Portbury, D.J. Hare, C.J. Sgambelloni, D.P. Bishop, D.I. Finkelstein, P.A. Doble, P.A. Adlard, Age modulates the injury-induced metallomic profile in the brain, *Metallomics.* 9 (2017) 402–410. doi:10.1039/C6MT00260A.
- [151] X. Zheng, Y. Pei, J. Liu, K. Tang, S. Qin, Effect of Molecular Size of Modifying Agents on the Properties of Gelatin films, *Food Sci. Technol. Res.* 23 (2017) 119–127. doi:10.3136/fstr.23.119.
- [152] Grace Bio-Labs, HybriWell™ Sealing System, (2019). <https://gracebio.com/products/hybridization-and-incubation/hybrwell-sealing-system-hybridization-and-incubation/search/>.
- [153] S. Stephen, A. Pillay, Laser ablation of hard and soft materials – prospects and problems, *Int. J. Eng. Tech. Res.* 0869 (2017) 79–82.
- [154] D.B. Hibbert, J.J. Gooding, *Data analysis for chemistry: an introductory guide for students and laboratory scientists*, Oxford University Press, 2006.
- [155] D.J. Hare, E.J. New, G. McColl, Imaging metals in biology: pictures of metals in health and disease, *Metallomics.* 9 (2017) 343–345. doi:10.1039/C7MT90013A.
- [156] D.J. Hare, E.J. New, M.D. de Jonge, G. McColl, Imaging metals in biology: balancing sensitivity, selectivity and spatial resolution, *Chem. Soc. Rev.* 44 (2015) 5941–5958. doi:10.1039/C5CS00055F.
- [157] E.J. New, V.C. Wimmer, D.J. Hare, Promises and Pitfalls of Metal Imaging in Biology, *Cell Chem. Biol.* (2017) 1–12. doi:10.1016/j.chembiol.2017.10.006.

- [158] B. Paul, D.J. Hare, D.P. Bishop, C. Paton, V.T. Nguyen, N. Cole, M.M. Niedzwiecki, E. Andreozzi, A. Vais, J.L. Billings, L. Bray, A.I. Bush, G. McColl, B.R. Roberts, P.A. Adlard, D.I. Finkelstein, J. Hellstrom, J.M. Hergt, J.D. Woodhead, P. a. Doble, M.M. Niedzwiecki, E. Andreozzi, A. Vais, J.L. Billings, L. Bray, A.I. Bush, G. McColl, B.R. Roberts, P.A. Adlard, D.I. Finkelstein, J. Hellstrom, J.M. Hergt, J.D. Woodhead, P. a. Doble, M.M. Niedzwiecki, E. Andreozzi, A. Vais, J.L. Billings, L. Bray, A.I. Bush, G. McColl, B.R. Roberts, P.A. Adlard, D.I. Finkelstein, J. Hellstrom, J.M. Hergt, J.D. Woodhead, P. a. Doble, Visualising mouse neuroanatomy and function by metal distribution using laser ablation-inductively coupled plasma-mass spectrometry imaging, *Chem. Sci.* 6 (2015) 5383–5393. doi:10.1039/C5SC02231B.
- [159] S.J.M. Van Malderen, J.T. van Elteren, F. Vanhaecke, Submicrometer Imaging by Laser Ablation-Inductively Coupled Plasma Mass Spectrometry via Signal and Image Deconvolution Approaches., *Anal. Chem.* 87 (2015) 6125–32. doi:10.1021/acs.analchem.5b00700.
- [160] Y.H. Wang, J. Qiao, J.B. Li, P. Fu, S.C. Chu, J.F. Roddick, Sparse representation-based MRI super-resolution reconstruction, *Meas. J. Int. Meas. Confed.* 47 (2014) 946–953. doi:10.1016/j.measurement.2013.10.026.
- [161] B. Huang, W. Wang, M. Bates, X. Zhuang, Three-Dimensional Super-Resolution Imaging by Stochastic Optical Reconstruction Microscopy, *Science* (80-.). 319 (2008) 810–813. doi:10.1126/science.1153529.
- [162] N. Manivannan, B.D. Clymer, A. Bratasz, K.A. Powell, Comparison of Super Resolution Reconstruction Acquisition Geometries for Use in Mouse Phenotyping, *Int. J. Biomed. Imaging.* 2013 (2013) 1–11. doi:10.1155/2013/820874.
- [163] A.P. Mahmoudzadeh, N.H. Kashou, Interpolation-based super-resolution reconstruction: effects of slice thickness, *J. Med. Imaging.* 1 (2014) 034007. doi:10.1117/1.JMI.1.3.034007.
- [164] J. Woo, Y. Bai, S. Roy, E.Z. Murano, M. Stone, J.L. Prince, Super-resolution reconstruction for tongue MR images, in: D.R. Haynor, S. Ourselin (Eds.), 2012: p.

83140C. doi:10.1117/12.911445.

- [165] A. Gholipour, S.K. Warfield, Super-resolution reconstruction of fetal brain MRI, MICCAI Work. Image Anal. Dev. Brain (IADB'2009). (2009) 45–52.
- [166] A. Gholipour, J.A. Estroff, S.K. Warfield, Robust Super-Resolution Volume Reconstruction From Slice Acquisitions: Application to Fetal Brain MRI, IEEE Trans. Med. Imaging. 29 (2010) 1739–1758. doi:10.1109/TMI.2010.2051680.
- [167] J.R. Chirinos, D.D. Oropeza, J.J. Gonzalez, H. Hou, M. Morey, V. Zorba, R.E. Russo, Simultaneous 3-dimensional elemental imaging with LIBS and LA-ICP-MS, J. Anal. At. Spectrom. 29 (2014) 1292–1298. doi:10.1039/c4ja00066h.
- [168] D.J. Hare, J.L. George, R. Grimm, S. Wilkins, P. a Adlard, R. a Cherny, A.I. Bush, D.I. Finkelstein, P. Doble, Three-dimensional elemental bio-imaging of Fe, Zn, Cu, Mn and P in a 6-hydroxydopamine lesioned mouse brain., Metallomics. 2 (2010) 745–53. doi:10.1039/c0mt00039f.
- [169] S.J.M. Van Malderen, B. Laforce, T. Van Acker, C. Nys, M. De Rijcke, R. de Rycke, M. De Bruyne, M.N. Boone, K. De Schamphelaere, O. Borovinskaya, B. De Samber, L. Vincze, F. Vanhaecke, Three-Dimensional Reconstruction of the Tissue-Specific Multielemental Distribution within *Ceriodaphnia dubia* via Multimodal Registration Using Laser Ablation ICP-Mass Spectrometry and X-ray Spectroscopic Techniques, Anal. Chem. 89 (2017) 4161–4168. doi:10.1021/acs.analchem.7b00111.
- [170] S.J.M. Van Malderen, B. Laforce, T. Van Acker, L. Vincze, F. Vanhaecke, Imaging the 3D trace metal and metalloid distribution in mature wheat and rye grains via laser ablation-ICP-mass spectrometry and micro-X-ray fluorescence spectrometry, J. Anal. At. Spectrom. (2016). doi:10.1039/C6JA00357E.
- [171] D.J. Hare, J.K. Lee, A.D. Beavis, A. van Gramberg, J. George, P. a Adlard, D.I. Finkelstein, P. a Doble, Three-dimensional atlas of iron, copper, and zinc in the mouse cerebrum and brainstem., Anal. Chem. 84 (2012) 3990–7. doi:10.1021/ac300374x.

- [172] E. Lützen, M. Holtkamp, I. Stamme, R. Schmid, M. Sperling, M. Pütz, U. Karst, Multimodal imaging of hallucinogens 25C- and 25I-NBOMe on blotter papers, *Drug Test. Anal.* 12 (2020) 465–471. doi:10.1002/dta.2751.
- [173] J. Schindelin, I. Arganda-Carreras, E. Frise, V. Kaynig, M. Longair, T. Pietzsch, S. Preibisch, C. Rueden, S. Saalfeld, B. Schmid, J.-Y.J.-Y. Tinevez, D.J. White, V. Hartenstein, K. Eliceiri, P. Tomancak, A. Cardona, K. Liceiri, P. Tomancak, C. A., Fiji: an open source platform for biological image analysis., *Nat. Methods.* 9 (2012) 676–682. doi:10.1038/nmeth.2019.Fiji.
- [174] N. Jearawiriyapaisarn, H.M. Moulton, B. Buckley, J. Roberts, P. Sazani, S. Fucharoen, P.L. Iversen, R. Kole, Sustained Dystrophin Expression Induced by Peptide-conjugated Morpholino Oligomers in the Muscles of mdx Mice, *Mol. Ther.* 16 (2008) 1624–1629. doi:10.1038/mt.2008.120.
- [175] C.F.V. Loan, The ubiquitous Kronecker product, *J. Comput. Appl. Math.* 123 (2000) 85–100. doi:10.1016/S0377-0427(00)00393-9.
- [176] D. Garcia, Robust smoothing of gridded data in one and higher dimensions with missing values, *Comput. Stat. Data Anal.* 54 (2010) 1167–1178. doi:10.1016/j.csda.2009.09.020.
- [177] S.J.M. Van Malderen, J.T. van Elteren, F. Vanhaecke, Development of a fast laser ablation-inductively coupled plasma-mass spectrometry cell for sub- μm scanning of layered materials, *J. Anal. At. Spectrom.* 30 (2014) 119–125. doi:10.1039/C4JA00137K.
- [178] D. Sage, L. Donati, F. Soulez, D. Fortun, G. Schmit, A. Seitz, R. Guiet, C. Vonesch, M. Unser, DeconvolutionLab2: An open-source software for deconvolution microscopy, *Methods.* 115 (2017) 28–41. doi:10.1016/j.ymeth.2016.12.015.
- [179] J. Ahrens, B. Geveci, C. Law, ParaView : An End-User Tool for Large Data Visualization, *Energy.* 836 (2005) 717–732. doi:10.1021/ol051115g.
- [180] Charles Zaiontz, Real Statistics Using Excel, (2019). <https://www.real-statistics.com/> (accessed April 1, 2019).

- [181] R. Barresi, Dystroglycan: from biosynthesis to pathogenesis of human disease, *J. Cell Sci.* 119 (2006) 199–207. doi:10.1242/jcs.02814.
- [182] J.M. Ervasti, K.P. Campbell, Membrane organization of the dystrophin-glycoprotein complex, *Cell.* 66 (1991) 1121–1131. doi:10.1016/0092-8674(91)90035-W.
- [183] K. Anthony, V. Arechavala-Gomez, L.E. Taylor, A. Vulin, Y. Kaminoh, S. Torelli, L. Feng, N. Janghra, G. Bonne, M. Beuvin, R. Barresi, M. Henderson, S. Laval, A. Loubakos, G. Campion, V. Straub, T. Voit, C.A. Sewry, J.E. Morgan, K.M. Flanigan, F. Muntoni, Dystrophin quantification: Biological and translational research implications, *Neurology.* 83 (2014) 2062–2069. doi:10.1212/WNL.0000000000001025.
- [184] V. Arechavala-Gomez, M. Kinali, L. Feng, M. Guglieri, G. Edge, M. Main, D. Hunt, J. Lehovsky, V. Straub, K. Bushby, C.A. Sewry, J.E. Morgan, F. Muntoni, Revertant fibres and dystrophin traces in Duchenne muscular dystrophy: Implication for clinical trials, *Neuromuscul. Disord.* 20 (2010) 295–301. doi:10.1016/j.nmd.2010.03.007.
- [185] C.G. Bönnemann, A. Rutkowski, E. Mercuri, F. Muntoni, 173rd ENMC international workshop: Congenital muscular dystrophy outcome measures 5–7 March 2010, Naarden, The Netherlands, *Neuromuscul. Disord.* 21 (2011) 513–522. doi:10.1016/j.nmd.2011.04.004.
- [186] Peripheral and Central Nervous System Drugs, A.C. Meeting, FDA Briefing Document - Translarna (Ataluren), 2017. <https://www.fda.gov/downloads/advisorycommittees/committeesmeetingmaterials/drugs/peripheralandcentralnervoussystemdrugsadvisorycommittee/ucm577349.pdf>.
- [187] I. Sarepta Therapeutics, PERIPHERAL AND CENTRAL NERVOUS SYSTEM DRUGS ADVISORY COMMITTEE, Cambridge, MA, 2016.
- [188] U.S. Department of Health and Human Services, Duchenne Muscular Dystrophy

and Related Dystrophinopathies: Developing Drugs for Treatment Guidance for Industry, Silver Spring, MD, 2018.

- [189] L.E. Taylor, Y.J. Kaminoh, C.K. Rodesch, K.M. Flanigan, Quantification of dystrophin immunofluorescence in dystrophinopathy muscle specimens, *Neuropathol. Appl. Neurobiol.* 38 (2012) 591–601. doi:10.1111/j.1365-2990.2012.01250.x.
- [190] C. Beekman, J.A. Sipkens, J. Testerink, S. Giannakopoulos, D. Kreuger, J.C. Van Deutekom, G. V. Campion, S.J. De Kimpe, A. Loubakos, A sensitive, reproducible and objective immunofluorescence analysis method of dystrophin in individual fibers in samples from patients with duchenne muscular dystrophy, *PLoS One.* 9 (2014). doi:10.1371/journal.pone.0107494.
- [191] F. Aeffner, C. Faelan, S.A. Moore, A. Moody, J.C. Black, J.S. Charleston, D.E. Frank, J. Dworzak, J. Kris Piper, M. Ranjitkar, K. Wilson, S. Kanaly, D.G. Rudmann, H. Lange, G. David Young, A.J. Milici, Validation of a muscle-specific tissue image analysis tool for quantitative assessment of dystrophin staining in frozen muscle biopsies, *Arch. Pathol. Lab. Med.* 143 (2019) 197–205. doi:10.5858/arpa.2017-0536-OA.
- [192] V. Straub, P. Balabanov, K. Bushby, M. Ensini, N. Goemans, A. De Luca, A. Pereda, R. Hemmings, G. Campion, E. Kaye, V. Arechavala-Gomez, A. Goyenvalle, E. Niks, O. Veldhuizen, P. Furlong, V. Stoyanova-Beninska, M.J. Wood, A. Johnson, E. Mercuri, F. Muntoni, B. Sepodes, M. Haas, E. Vroom, A. Aartsma-Rus, Stakeholder cooperation to overcome challenges in orphan medicine development: the example of Duchenne muscular dystrophy, *Lancet Neurol.* 15 (2016) 882–890. doi:10.1016/S1474-4422(16)30035-7.
- [193] F. Muntoni, Is a muscle biopsy in Duchenne dystrophy really necessary?, *Neurology.* 57 (2001) 574–575. doi:10.1212/WNL.57.4.574.
- [194] L.V.B. Nicholson, M.A. Johnson, D. Gardner-Medwin, S. Bhattacharya, J.B. Harris, Heterogeneity of dystrophin expression in patients with Duchenne and Becker muscular dystrophy, *Acta Neuropathol.* 80 (1990) 239–250.

doi:10.1007/BF00294640.

- [195] C. Giesen, H.A.O. Wang, D. Schapiro, N. Zivanovic, A. Jacobs, B. Hattendorf, P.J. Schüffler, D. Grolimund, J.M. Buhmann, S. Brandt, Z. Varga, P.J. Wild, D. Günther, B. Bodenmiller, Highly multiplexed imaging of tumor tissues with subcellular resolution by mass cytometry, *Nat. Methods*. 11 (2014) 417–422. doi:10.1038/nmeth.2869.
- [196] D. Schapiro, H.W. Jackson, S. Raghuraman, J.R. Fischer, V.R.T. Zanotelli, D. Schulz, C. Giesen, R. Catena, Z. Varga, B. Bodenmiller, histoCAT: analysis of cell phenotypes and interactions in multiplex image cytometry data, *Nat. Methods*. (2017). doi:10.1038/nmeth.4391.
- [197] P.J. Schüffler, D. Schapiro, C. Giesen, H.A.O. Wang, B. Bodenmiller, J.M. Buhmann, Automatic single cell segmentation on highly multiplexed tissue images, *Cytom. Part A*. 87 (2015) 936–942. doi:10.1002/cyto.a.22702.
- [198] D. Schulz, V.R.T. Zanotelli, J.R. Fischer, D. Schapiro, S. Engler, X.-K. Lun, H.W. Jackson, B. Bodenmiller, Simultaneous Multiplexed Imaging of mRNA and Proteins with Subcellular Resolution in Breast Cancer Tissue Samples by Mass Cytometry, *Cell Syst*. (2017) 1–12. doi:10.1016/j.cels.2017.12.001.
- [199] A. Aljakna, E. Lauer, S. Lenglet, S. Grabherr, T. Fracasso, M. Augsburger, S. Sabatasso, A. Thomas, Multiplex quantitative imaging of human myocardial infarction by mass spectrometry-immunohistochemistry, *Int. J. Legal Med*. (2018). doi:10.1007/s00414-018-1813-9.
- [200] N. Otsu, A threshold selection method from gray-level histograms, *IEEE Trans. Syst. Man. Cybern*. 9 (1979) 62–66. doi:10.1109/TSMC.1979.4310076.
- [201] E.M. Gibbs, J.L. Marshall, E. Ma, T.M. Nguyen, G. Hong, J. Lam, M.J. Spencer, R.H. Crosbie-Watson, High levels of sarcospan are well tolerated and act as a sarcolemmal stabilizer to address skeletal muscle and pulmonary dysfunction in DMD., *Hum. Mol. Genet*. 25 (2016) 5395–5406. doi:10.1093/hmg/ddw356.
- [202] J.W. Lee, R.S. Weiner, J.M. Sailstad, R.R. Bowsher, D.W. Knuth, P.J. O’Brien, J.L.

- Fourcroy, R. Dixit, L. Pandite, R.G. Pietrusko, H.D. Soares, V. Quarmby, O.L. Vesterqvist, D.M. Potter, J.L. Witliff, H.A. Fritche, T. O’Leary, L. Perlee, S. Kadam, J.A. Wagner, Method Validation and Measurement of Biomarkers in Nonclinical and Clinical Samples in Drug Development: A Conference Report, *Pharm. Res.* 22 (2005) 499–511. doi:10.1007/s11095-005-2495-9.
- [203] T. Tyner, J. Francis, ACS Reagent Chemicals, American Chemical Society, Washington, DC, 2017. doi:10.1021/acsreagents.
- [204] C. Matenaers, B. Popper, A. Rieger, R. Wanke, A. Blutke, Practicable methods for histological section thickness measurement in quantitative stereological analyses, *PLoS One.* 13 (2018) 1–21. doi:10.1371/journal.pone.0192879.
- [205] A.D. Pearse, R. Marks, Measurement of section thickness in quantitative microscopy with special reference to enzyme histochemistry, *J. Clin. Pathol.* 27 (1974) 615–618. doi:10.1136/jcp.27.8.615.
- [206] A.D. Pearse, R. Marks, Further studies on section thickness measurement, *Histochem. J.* 8 (1976) 383–386. doi:10.1007/BF01003827.
- [207] C.N. Carlo, C.F. Stevens, Analysis of differential shrinkage in frozen brain sections and its implications for the use of guard zones in stereology, *J. Comp. Neurol.* 519 (2011) 2803–2810. doi:10.1002/cne.22652.
- [208] D. Gardella, W.J. Hatton, H.B. Rind, G.D. Rosen, C.S. Von Bartheld, Differential tissue shrinkage and compression in the z-axis: Implications for optical disector counting in vibratome-, plastic- and cryosections, *J. Neurosci. Methods.* 124 (2003) 45–59. doi:10.1016/S0165-0270(02)00363-1.
- [209] C.F. Almeida, S.A. Fernandes, A.F. Ribeiro Junior, O. Keith Okamoto, M. Vainzof, Muscle satellite cells: Exploring the basic biology to rule them, *Stem Cells Int.* 2016 (2016). doi:10.1155/2016/1078686.
- [210] N.A. Dumont, C.F. Bentzinger, M.C. Sincennes, M.A. Rudnicki, Satellite cells and skeletal muscle regeneration, *Compr. Physiol.* 5 (2015) 1027–1059. doi:10.1002/cphy.c140068.

- [211] N.A. Dumont, Y.X. Wang, J. Von Maltzahn, A. Pasut, C.F. Bentzinger, C.E. Brun, M.A. Rudnicki, Dystrophin expression in muscle stem cells regulates their polarity and asymmetric division, *Nat. Med.* 21 (2015) 1455–1463. doi:10.1038/nm.3990.
- [212] F. Le Grand, M. Rudnicki, Satellite and stem cells in muscle growth and repair, *Development.* 134 (2007) 3953–3957. doi:10.1242/dev.005934.
- [213] H. Yin, F. Price, M.A. Rudnicki, Satellite Cells and the Muscle Stem Cell Niche, *Physiol. Rev.* 93 (2013) 23–67. doi:10.1152/physrev.00043.2011.
- [214] Y. Gimenez, B. Busser, F. Trichard, A. Kulesza, J.M. Laurent, V. Zaun, F. Lux, J.M. Benoit, G. Panczer, P. Dugourd, O. Tillement, F. Pelascini, L. Sancey, V. Motto-Ros, 3D Imaging of Nanoparticle Distribution in Biological Tissue by Laser-Induced Breakdown Spectroscopy., *Sci. Rep.* 6 (2016) 29936. doi:10.1038/srep29936.
- [215] A. Li, A. Kumar, Y. Ha, H. Corporaal, Correlation ratio based volume image registration on GPUs, *Microprocess. Microsyst.* 39 (2015) 998–1011. doi:10.1016/j.micpro.2015.04.002.
- [216] M.A. Viergever, J.B.A. Maintz, S. Klein, K. Murphy, M. Staring, J.P.W. Pluim, A survey of medical image registration – under review, *Med. Image Anal.* 33 (2016) 140–144. doi:10.1016/j.media.2016.06.030.
- [217] T. Mano, A. Albanese, H.-U. Dodt, A. Erturk, V. Gradinaru, J.B. Treweek, A. Miyawaki, K. Chung, H.R. Ueda, Whole-Brain Analysis of Cells and Circuits by Tissue Clearing and Light-Sheet Microscopy, *J. Neurosci.* 38 (2018) 9330–9337. doi:10.1523/JNEUROSCI.1677-18.2018.
- [218] J. Schöneberg, D. Dambournet, T.-L. Liu, R. Forster, D. Hockemeyer, E. Betzig, D.G. Drubin, 4D cell biology: big data image analytics and lattice light-sheet imaging reveal dynamics of clathrin-mediated endocytosis in stem cell-derived intestinal organoids, *Mol. Biol. Cell.* 29 (2018) 2959–2968. doi:10.1091/mbc.E18-06-0375.
- [219] S.A. Sloan, S. Darmanis, N. Huber, T.A. Khan, F. Birey, C. Caneda, R. Reimer, S.R.

- Quake, B.A. Barres, S.P. Paşca, Human Astrocyte Maturation Captured in 3D Cerebral Cortical Spheroids Derived from Pluripotent Stem Cells, *Neuron*. 95 (2017) 779–790.e6. doi:10.1016/j.neuron.2017.07.035.
- [220] Y. Zhao, O. Bucur, H. Irshad, F. Chen, A. Weins, A.L. Stancu, E.-Y. Oh, M. DiStasio, V. Torous, B. Glass, I.E. Stillman, S.J. Schnitt, A.H. Beck, E.S. Boyden, Nanoscale imaging of clinical specimens using pathology-optimized expansion microscopy, *Nat. Biotechnol.* 35 (2017) 757–764. doi:10.1038/nbt.3892.
- [221] R.M. Levenson, A.D. Borowsky, M. Angelo, PATHOBIOLOGY IN FOCUS Immunohistochemistry and mass spectrometry for highly multiplexed cellular molecular imaging, *Lab. Investig.* 00 (2015) 1–9. doi:10.1038/labinvest.2015.2.
- [222] W.C. Hanly, J.E. Artwohl, B.T. Bennett, Review of Polyclonal Antibody Production Procedures in Mammals and Poultry, *ILAR J.* 37 (1995) 93–118. doi:10.1093/ilar.37.3.93.
- [223] K. Groff, J. Brown, A.J. Clippinger, Modern affinity reagents: Recombinant antibodies and aptamers, *Biotechnol. Adv.* 33 (2015) 1787–1798. doi:10.1016/j.biotechadv.2015.10.004.
- [224] L.S. Rodkey, Evaluation of Antibody Clonality, in: *Antib. Eng. Protoc.*, Humana Press, New Jersey, 2003: pp. 151–164. doi:10.1385/0-89603-275-2:151.
- [225] C. De Michele, P. De Los Rios, G. Foffi, F. Piazza, Simulation and Theory of Antibody Binding to Crowded Antigen-Covered Surfaces, *PLoS Comput. Biol.* 12 (2016) 1–17. doi:10.1371/journal.pcbi.1004752.
- [226] B.A. Bukari, M. Citartan, E.S. Ch'ng, M.P. Bilibana, T. Rozhdestvensky, T.-H. Tang, Aptahistochemistry in diagnostic pathology: technical scrutiny and feasibility, *Histochem. Cell Biol.* 0 (2017) 1–9. doi:10.1007/s00418-017-1561-9.
- [227] A.D. Ellington, J.W. Szostak, In vitro selection of RNA molecules that bind specific ligands., *Nature*. 346 (1990) 818–822. doi:10.1038/346818a0.
- [228] L. Gold, D. Ayers, J. Bertino, C. Bock, A. Bock, E.N. Brody, J. Carter, A.B. Dalby,

- B.E. Eaton, T. Fitzwater, D. Flather, A. Forbes, T. Foreman, C. Fowler, B. Gawande, M. Goss, M. Gunn, S. Gupta, D. Halladay, J. Heil, J. Heilig, B. Hicke, G. Husar, N. Janjic, T. Jarvis, S. Jennings, E. Katilius, T.R. Keeney, N. Kim, T.H. Koch, S. Kraemer, L. Kroiss, N. Le, D. Levine, W. Lindsey, B. Lollo, W. Mayfield, M. Mehan, R. Mehler, S.K. Nelson, M. Nelson, D. Nieuwlandt, M. Nikrad, U. Ochsner, R.M. Ostroff, M. Otis, T. Parker, S. Pietrasiewicz, D.I. Resnicow, J. Rohloff, G. Sanders, S. Sattin, D. Schneider, B. Singer, M. Stanton, A. Sterkel, A. Stewart, S. Stratford, J.D. Vaught, M. Vrkljan, J.J. Walker, M. Watrobka, S. Waugh, A. Weiss, S.K. Wilcox, A. Wolfson, S.K. Wolk, C. Zhang, D. Zichi, Aptamer-based multiplexed proteomic technology for biomarker discovery, *PLoS One*. 5 (2010). doi:10.1371/journal.pone.0015004.
- [229] K. Mullis, F. Faloona, S. Scharf, R. Saiki, G. Horn, H. Erlich, Specific enzymatic amplification of DNA in vitro: the polymerase chain reaction. 1986., *Biotechnology*. 24 (1992) 17–27. <http://www.ncbi.nlm.nih.gov/pubmed/1422010>.
- [230] W. Tan, H. Wang, Y. Chen, X. Zhang, H. Zhu, C. Yang, R. Yang, C. Liu, Molecular aptamers for drug delivery, *Trends Biotechnol.* 29 (2011) 634–640. doi:10.1016/j.tibtech.2011.06.009.
- [231] B. Röder, K. Frühwirth, C. Vogl, M. Wagner, P. Rossmann, Impact of long-term storage on stability of standard DNA for nucleic acid-based methods, *J. Clin. Microbiol.* 48 (2010) 4260–4262. doi:10.1128/JCM.01230-10.
- [232] Y. Yoshida, N. Sakai, H. Masuda, M. Furuichi, F. Nishikawa, S. Nishikawa, H. Mizuno, I. Waga, Rabbit antibody detection with RNA aptamers, *Anal. Biochem.* 375 (2008) 217–222. doi:10.1016/j.ab.2008.01.005.
- [233] M. Tvrdonova, M. Vlcnovska, L.P. Vanickova, V. Kanicky, V. Adam, L. Ascher, N. Jakubowski, M. Vaculovicova, T. Vaculovic, Gold nanoparticles as labels for immunochemical analysis using laser ablation inductively coupled plasma mass spectrometry, *Anal. Bioanal. Chem.* (2018). doi:10.1007/s00216-018-1300-7.
- [234] N.S. Barteneva, I.A. Vorob'ev, Quantum dots in microscopy and cytometry: immunostaining applications., *Microsc. Sci. Technol. Appl. Educ.* 1 (2010) 710–

721.

- [235] J.M. Boggs, Myelin basic protein: A multifunctional protein, *Cell. Mol. Life Sci.* 63 (2006) 1945–1961. doi:10.1007/s00018-006-6094-7.
- [236] K.K. Koeller, F. Barkhof, Demyelinating Diseases, in: *Dis. Brain, Head Neck, Spine* 2012–2015, Springer Milan, Milano, 2012: pp. 50–57. doi:10.1007/978-88-470-2628-5_9.
- [237] J.A. Perge, J.E. Niven, E. Mugnaini, V. Balasubramanian, P. Sterling, Why Do Axons Differ in Caliber?, *J. Neurosci.* 32 (2012) 626–638. doi:10.1523/jneurosci.4254-11.2012.
- [238] J.-P. Michalski, R. Kothary, Oligodendrocytes in a Nutshell, *Front. Cell. Neurosci.* 9 (2015) 1–11. doi:10.3389/fncel.2015.00340.
- [239] S.M. Sunkin, L. Ng, C. Lau, T. Dolbeare, T.L. Gilbert, C.L. Thompson, M. Hawrylycz, C. Dang, Allen Brain Atlas: An integrated spatio-temporal portal for exploring the central nervous system, *Nucleic Acids Res.* 41 (2013). doi:10.1093/nar/gks1042.
- [240] M. Uhlén, L. Fagerberg, B.M. Hallström, C. Lindskog, P. Oksvold, A. Mardinoglu, Å. Sivertsson, C. Kampf, E. Sjöstedt, A. Asplund, I. Olsson, K. Edlund, E. Lundberg, S. Navani, C.A. Szigartyo, J. Odeberg, D. Djureinovic, J.O. Takanen, S. Hober, T. Alm, P. Edqvist, H. Berling, H. Tegel, J. Mulder, J. Rockberg, P. Nilsson, J.M. Schwenk, M. Hamsten, K. Von Feilitzen, M. Forsberg, L. Persson, F. Johansson, M. Zwahlen, G. Von Heijne, J. Nielsen, F. Pontén, Tissue-based map of the human proteome, *Science* (80-.). 347 (2015) 1260419–1260419. doi:10.1126/science.1260419.
- [241] G.T. Rozenblum, T. Kaufman, A.D. Vitullo, Myelin Basic Protein and a Multiple Sclerosis-related MBP-peptide Bind to Oligonucleotides, *Mol. Ther. Acids.* 3 (2014) e192. doi:10.1038/mtna.2014.43.
- [242] P. Stothard, The Sequence Manipulation Suite: JavaScript Programs for Analyzing and Formatting Protein and DNA Sequences, *Biotechniques.* 28 (2000) 1102–1104.

doi:10.2144/00286ir01.

- [243] B.E. McKay, M.L. Molineux, R.W. Turner, Endogenous Biotin in Rat Brain, in: *Avidin-Biotin Interact.*, Humana Press, Totowa, NJ, 2008: pp. 111–128. doi:10.1007/978-1-59745-579-4_10.
- [244] S. Prost, R.E.B. Kishen, D.C. Kluth, C.O.C. Bellamy, Working with commercially available quantum dots for immunofluorescence on tissue sections, *PLoS One*. 11 (2016) 1–23. doi:10.1371/journal.pone.0163856.
- [245] A. Badon, A.C. Boccara, G. Lerosey, M. Fink, A. Aubry, Multiple scattering limit in optical microscopy, *Opt. Express*. 25 (2017) 28914. doi:10.1364/OE.25.028914.

9 Appendix

Appendix 9-1 Super Resolution Reconstruction MATLAB code

```
%% Import raw data
delimiterIn = ',';
headerlinesIn = 1;
Directory='D:\';
mkdir ([Directory], 'OutDirectory');
OutDirectory=( [Directory 'OutDirectory\']);
mkdir ([Directory], 'SliceDirectory');
SliceDirectory=( [Directory 'SliceDirectory\']);
mkdir ([Directory], 'ProcessedSliceDirectory');
ProcessedSliceDirectory=( [Directory 'ProcessedSliceDirectory\']);

%% Files and initial conditions for loop
HFiles=dir([Directory '*horz*.csv']);
VFiles=dir([Directory '*vert*.csv']);
lengthV=length(VFiles);
lengthH=length(HFiles);
layer=0;

%% Constants from LA-ICP-MS parameters
Speed=20;
Scantime=0.1 ;
SpotSize=10;
gradient=1;
intercept=0;
Frequency=20;
M=SpotSize/(Speed*Scantime);
N=floor(M/2);
if mod(N,2)==0
    N=N+1;
end
Layers=2;
TheoryRes=Speed/Frequency;
ExpRes=Speed/(M*2);

%% Data is measured then trimmed of warmup and washout time data
dataH = importdata([Directory HFiles(1).name],delimiterIn,headerlinesIn);
dataV = importdata([Directory VFiles(1).name],delimiterIn,headerlinesIn);

la1=size(dataH.data,1);
wa=size(dataH.data,2);
lb1=size(dataV.data,1);
wb=size(dataV.data,2);
j=round(((1.2/Scantime)*10);
k=round((la1-(wa*M))-j);
l=round((lb1-(wb*M))-j);%
A1=dataH.data;
A1(la1-l+1:la1, :) = [];
A1(1:j, :) = [];
updowncut1=A1;
sizex=size(updowncut1,1)*Layers+N;
sizey=size(updowncut1,2)*M*Layers+N;
lengthz=length(dir([Directory '*.csv']));
FirstLayer=kron(dataH.data,ones(1,M));
```

```
%% Empty 3D array is constructed from measured values
RM=zeros(sizey,sizex,lengthz);%to include padding and kron
```

```
%% Reconstruction of data to fill the above 3D array
```

```
for ifp=1:lengthV
fileH = importdata([Directory HFiles(ifp).name],delimiterIn,headerlinesIn);
fileV = importdata([Directory VFiles(ifp).name],delimiterIn,headerlinesIn);
dataH=fileH.data;
dataV=fileV.data;

dataH(la1-l+1:la1, :) = [];
dataH(1:j, :) = [];
dataH=(dataH-intercept)/gradient;
dataH=kron(dataH,ones(1,M));
dataH=upsample(dataH,Layers);
dataH=transpose(dataH);
dataH=upsample(dataH,Layers);

dataH=padarray(dataH,[N N],0,'post');

dataV(lb1-k+1:lb1, :) = [];
dataV(1:j, :) = [];
dataV=(dataV-intercept)/gradient;
dataV=kron(dataV,ones(1,M));
dataV=upsample(dataV,Layers);
dataV=transpose(dataV);
dataV=upsample(dataV,Layers);
dataV=transpose(dataV);

dataV=padarray(dataV,[N N],0,'pre');

layer=layer+1;

RM(:,layer) = dataH;

layer=layer+1;

RM(:,layer) = dataV;

end

if lengthV<lengthH

dataH1 = importdata([Directory HFiles(lengthH).name],delimiterIn,headerlinesIn);

dataH1(la1-l+1:la1, :) = [];
dataH1(1:j, :) = [];

dataH1=(dataH1-intercept)/gradient;
dataH1=kron(dataH1,ones(1,M));
dataH1=upsample(dataH1,Layers);
dataH1=transpose(dataH1);
dataH1=upsample(dataH1,Layers);
```

```

dataH1=padarray(dataH1,[N N],0,'post');

layer=layer+1;

RM(:, :, layer) = dataH1;

end

RM(RM == 0) = NaN;

%% Trilinear interpolation of empty elements of array
FM = ones(size(RM));
MM = ones(size(RM));
MM = MM.*RM;
[NcomX, NcomY, NcomZ] = size(RM);

for iz=1:NcomZ
for ic=1:NcomY
for ir=1:NcomX
if isnan(MM(ir,ic,iz))
cf=0;
avenum=0;
if (iz>1)&&(~isnan(MM(ir,ic,iz-1)))
cf=cf+MM(ir,ic,iz-1);
avenum=avenum+1;
end
if (ir-1>0)&&(iz>1)&&(~isnan(MM(ir-1,ic,iz-1)))
cf=cf+MM(ir-1,ic,iz-1);
avenum=avenum+1;
end
if (ir+1<=NcomX)&&(iz>1)&&(~isnan(MM(ir+1,ic,iz-1)))
cf=cf+MM(ir+1,ic,iz-1);
avenum=avenum+1;
end
if (ic-1>0)&&(iz>1)&&(~isnan(MM(ir,ic-1,iz-1)))
cf=cf+MM(ir,ic-1,iz-1);
avenum=avenum+1;
end
if (ic+1<=NcomY)&&(iz>1)&&(~isnan(MM(ir,ic+1,iz-1)))
cf=cf+MM(ir,ic+1,iz-1);
avenum=avenum+1;
end
if (ir-1>0)&&(ic-1>0)&&(iz>1)&&(~isnan(MM(ir-1,ic-1,iz-1)))
cf=cf+MM(ir-1,ic-1,iz-1);
avenum=avenum+1;
end
if (ir+1<=NcomX)&&(ic+1<=NcomY)&&(iz>1)&&(~isnan(MM(ir+1,ic+1,iz-1)))
cf=cf+MM(ir+1,ic+1,iz-1);
avenum=avenum+1;
end
if (ir+1<=NcomX)&&(ic-1>0)&&(iz>1)&&(~isnan(MM(ir+1,ic-1,iz-1)))
cf=cf+MM(ir+1,ic-1,iz-1);
avenum=avenum+1;
end
if (ir-1>0)&&(ic+1<=NcomY)&&(iz>1)&&(~isnan(MM(ir-1,ic+1,iz-1)))
cf=cf+MM(ir-1,ic+1,iz-1);
avenum=avenum+1;
end
if (ir-1>0)&&(~isnan(MM(ir-1,ic,iz)))

```

```

    cf=cf+MM(ir-1,ic,iz);
    aenum=aenum+1;
end
if (ir+1<=NcomX)&&(~isnan(MM(ir+1,ic,iz)))
    cf=cf+MM(ir+1,ic,iz);
    aenum=aenum+1;
end
if (ic-1>0)&&(~isnan(MM(ir,ic-1,iz)))
    cf=cf+MM(ir,ic-1,iz);
    aenum=aenum+1;
end
if (ic+1<=NcomY)&&(~isnan(MM(ir,ic+1,iz)))
    cf=cf+MM(ir,ic+1,iz);
    aenum=aenum+1;
end
if (ir-1>0)&&(ic-1>0)&&(~isnan(MM(ir-1,ic-1,iz)))
    cf=cf+MM(ir-1,ic-1,iz);
    aenum=aenum+1;
end
if (ir+1<=NcomX)&&(ic+1<=NcomY)&&(~isnan(MM(ir+1,ic+1,iz)))
    cf=cf+MM(ir+1,ic+1,iz);
    aenum=aenum+1;
end
if (ir+1<=NcomX)&&(ic-1>0)&&(~isnan(MM(ir+1,ic-1,iz)))
    cf=cf+MM(ir+1,ic-1,iz);
    aenum=aenum+1;
end
if (ir-1>0)&&(ic+1<=NcomY)&&(~isnan(MM(ir-1,ic+1,iz)))
    cf=cf+MM(ir-1,ic+1,iz);
    aenum=aenum+1;
end
end
%from layer to layer+1
if (iz<NcomZ)&&(~isnan(MM(ir,ic,iz+1)))
    cf=cf+MM(ir,ic,iz+1);
    aenum=aenum+1;
end
if (ir-1>0)&&(iz<NcomZ)&&(~isnan(MM(ir-1,ic,iz+1)))
    cf=cf+MM(ir-1,ic,iz+1);
    aenum=aenum+1;
end
if (ir+1<=NcomX)&&(iz<NcomZ)&&(~isnan(MM(ir+1,ic,iz+1)))
    cf=cf+MM(ir+1,ic,iz+1);
    aenum=aenum+1;
end
if (ic-1>0)&&(iz<NcomZ)&&(~isnan(MM(ir,ic-1,iz+1)))
    cf=cf+MM(ir,ic-1,iz+1);
    aenum=aenum+1;
end
if (ic+1<=NcomY)&&(iz<NcomZ)&&(~isnan(MM(ir,ic+1,iz+1)))
    cf=cf+MM(ir,ic+1,iz+1);
    aenum=aenum+1;
end
if (ir-1>0)&&(ic-1>0)&&(iz<NcomZ)&&(~isnan(MM(ir-1,ic-1,iz+1)))
    cf=cf+MM(ir-1,ic-1,iz+1);
    aenum=aenum+1;
end
if (ir+1<=NcomX)&&(ic+1<=NcomY)&&(iz<NcomZ)&&(~isnan(MM(ir+1,ic+1,iz+1)))
    cf=cf+MM(ir+1,ic+1,iz+1);
    aenum=aenum+1;
end
if (ir+1<=NcomX)&&(ic-1>0)&&(iz<NcomZ)&&(~isnan(MM(ir+1,ic-1,iz+1)))

```

```

        cf=cf+MM(ir+1,ic-1,iz+1);
        avenum=avenum+1;
    end
    if (ir-1>0)&&(ic+1<=NcomY)&&(iz<NcomZ)&&(~isnan(MM(ir-1,ic+1,iz+1)))
        cf=cf+MM(ir-1,ic+1,iz+1);
        avenum=avenum+1;
    end

    FM(ir,ic,iz)=cf/avenum;
else
    FM(ir,ic,iz)=MM(ir,ic,iz);
end
end
end
end

%% Remove any errors from interpolation and create flat 2D array from summing 3D array
FM(isnan(FM))=0;
InterpBig3D=FM;
Interp2D=sum(InterpBig3D,3);

%% Split 3D array into layers and export
for ilayers=1:lengthz
    name = sprintf('%sSlice0%d_Gd158SRR.csv',SliceDirectory,ilayers);
    dlmwrite(name,FM(:, :, ilayers));
end

%% Export 2d Array as csv and vtk for paraview
dlmwrite([OutDirectory 'SRRCombined2D.csv'],Interp2D);

InterpBin=InterpBig3D;

[x y z]=size(InterpBin);
filename='3DSRR.vtk';
total=numel(InterpBig3D);
z=size(InterpBig3D,3);
fp=fopen(sprintf('%s',filename),'w');
fp=fopen([OutDirectory '3DSRR.vtk'],'w');
fprintf(fp,sprintf('# vtk DataFile Version 2.0\n%s\nASCII\nDATASET STRUCTURED_POINTS\nDIMENSIONS
%d %d %d\nORIGIN 0.0 0.0 0.0\nSPACING 1.0 1.0 5.0\n \nPOINT_DATA %d\nSCALARS values
double\nLOOKUP_TABLE default\n',filename,x,y,z,total));
for z1=1:z;
for y1=1:y;
for x1=1:x;
    if x1>=x;
        fprintf(fp,'%d\n',InterpBin(x1,y1,z1));
    else
        fprintf(fp,'%d\t',InterpBin(x1,y1,z1));
    end
end
end
end
end
fclose(fp);

```